MASTERARBEIT

Titel der Masterarbeit

„High temperature electrolysis on model-type $La_{0.6}Sr_{0.4}FeO_{3-\delta}$ thin film electrodes"

verfasst von

Gregor Walch, B.Sc.

angestrebter akademischer Grad

Master of Science (MSc)

Wien, 2013

"'And what will they burn instead of coal?'
'Water,' replied Harding.
'Water!' cried Pencroft, 'water as fuel for steamers and engines! Water to heat water!'
'Yes, but water decomposed into its primitive elements,' replied Cyrus Harding, 'and decomposed doubtless, by electricity, which will then have become a powerful and manageable force, for all great discoveries, by some inexplicable laws, appear to agree and become complete at the same time.'" Verne, J., *The Mysterious Island*; 1874/75. [1], [2]

Abstract

With the aim of ensuring sustainable energy supply in mind, the use of alternative energy sources such as wind or solar power and the conversion of their output into storable forms is a crucial issue. Solid state electrolyzers could accomplish this task by converting electric current and abundant compounds such as water or CO_2 into storable chemical compounds (e.g. H_2, CO). Because of the higher operating temperature, solid oxide electrolysis cells (SOECs) can be more efficient than electrolysis at lower temperatures.

The most common electrode material under reducing conditions for both SOECs and solide oxide fuel cells to date is the porous Ni/YSZ cermet, which has shown higher degradation in electrolysis mode and lower activity for electrolysis than for H_2 oxidation. A systematic search for new electrode materials benefits from a well-defined electrode geometry which allows easier comparison of materials. Acceptor-doped perovskites that exhibit electron as well as ionic conduction are promising candidates because the reduction reaction is not limited to the triple phase boundary (as in a cermet) but can take place on the whole electrode surface.

It was the aim of this work to electrochemically characterize model-type $La_{0.6}Sr_{0.4}FeO_{3-\delta}$ (LSF64) thin-film cathodes in an H_2O containing gas and to detect the electrolytically produced H_2 by a chemical analysis system. SOECs with LSF64 cathodes, yttria-stabilized zirconia (YSZ) electrolyte and $La_{0.6}Sr_{0.4}Co_{0.2}Fe_{0.8}O_{3-\delta}$ anode were fabricated. The LSF64 thin film was deposited by pulsed laser deposition (PLD), while the porous anode material was applied as a slurry and sintered subsequently.

Current-voltage and impedance measurements were carried out to characterize the cathode. The contribution of the porous anode to the overall DC resistance was shown to be negligible, the resistance of the electrolyte was measured by impedance spectroscopy and the corresponding potential drop could thus subtracted.

The impact of different experimental conditions on the measurements was interpreted electrochemically. For detection of the hydrogen produced during electrolysis a mass spectrometer was employed which required an extensive calibration study of a novel setup. The measured electrical current could be related to the change in gas concentrations by Faraday's law. Currents calculated from measured gas concentrations and the applied electrical current were in good agreement.

Zusammenfassung

Im Hinblick auf eine nachhaltige Energieversorgung ist die Verwendung von alternativen Energiequellen wie Wind- oder Solarenergie und die Umwandlung des so erzeugten Stromes in speicherbare Formen (z.B. H_2) entscheidend. Zur Bewältigung dieser Aufgabe könnten Festoxidelektrolysezellen (solid oxide electrolysis cells, SOECs) beitragen, die ausreichend vorhandene Stoffe wie Wasser oder CO_2 in speicherbare chemische Verbindungen (z.B. H_2, CO) umwandeln. Auf Grund der höheren Arbeitstemperaturen kann die Elektrolyse mit SOECs effizienter durchgeführt werden als bei niedrigerer Temperatur.

Das heute sowohl in Festoxidbrennstoffzellen als auch -elektrolysezellen unter reduzierenden Bedingungen am meisten verwendete Elektrodenmaterial ist ein Ni/YSZ cermet. An diesem porösen Material wurde im Elektrolysemodus höhere Degradation und niedrigere katalytische Aktivität als für die H_2-Oxidation beobachtet. Eine systematische Suche nach neuen Elektrodenmaterialien wird durch eine wohldefinierte Elektrodengeometrie erleichtert, die ein einfacheres Vergleichen der Materialien erlaubt. Akzeptordotierte Perowskite, die sowohl Elektronen- als auch Ionenleitung zeigen, sind vielversprechende Kandidaten, da die Reduktionsreaktion nicht nur - wie in einem cermet - entlang der Dreiphasengrenze stattfinden kann, sondern auf der gesamten Elektrodenoberfläche.

Das Ziel dieser Arbeit war die elektrochemische Charakterisierung von Dünnschicht-Modell-Kathoden aus $La_{0.6}Sr_{0.4}FeO_{3-\delta}$ (LSF64) in einer wasserhältigen Gasatmosphäre mit gleichzeitiger Detektion von elektrolytisch erzeugtem H_2. Hierzu wurden SOECs mit LSF64-Kathoden, yttrium-stabilisiertem Zirconiumdioxid (YSZ) als Elektrolyt und $La_{0.6}Sr_{0.4}Co_{0.2}Fe_{0.8}O_{3-\delta}$-Anoden hergestellt. Die LSF64-Dünnschicht wurde mit pulsed laser deposition (PLD) abgeschieden, während das poröse Anodenmaterial als Suspension aufgebracht und anschließend gesintert wurde.

Um die Kathode zu charakterisieren, wurden Strom-Spannungskurven und Impedanzmesssungen durchgeführt. Es konnte gezeigt werden, dass der Beitrag der porösen Anode zum gesamten Gleichstromwiderstand vernachlässigbar klein ist. Der Elektrolytwiderstand wurde mittels Impedanzspektroskopie gemessen und der entsprechende Spannungsabfall bei der Analyse berücksichtigt.

Die Auswirkungen unterschiedlicher experimenteller Bedingungen auf die Messergebnisse wurden elektrochemisch interpretiert. Der während der Elektrolyse produzierte Wasserstoff wurde mit Hilfe eines Massenspektrometers (MS) detektiert - in diesem neuen Setup erforderte die Quantifizierung mittels MS ausführliche Untersuchungen zur Kalibration bezüglich der Gasmenge. Der gemessene elektrische Strom wurde mit der Änderung der Gaskonzentration über das Faraday'sche Gesetz in Zusammenhang gebracht, wobei die aus den gemessenen Gaskonzentrationen berechneten Ströme gut mit dem elektrisch gemessenen Strom übereinstimmten.

Contents

1 Introduction

1.1 Motivation for electrolysis

"Sustainable development is development that meets the needs of the present without compromising the ability of future generations to meet their own needs." [3, p 54] Sustainability is an issue that many countries made a commitment to, for example in the Kyoto protocol [4, article 2, paragraph 1], and which is closely connected to the way people meet their energy demands in industry, transportation, heating/cooling houses, etc.

Today, the primary energy supply worldwide is based on fossil fuels, such as coal, oil or natural gas [5]. This situation is not sustainable for the following reasons:

- Fossil fuels will eventually be depleted.

- The use of fossil fuels is a source of greenhouse gases and most of the observered warming of the climate system since the mid-20th century [6, p 5] has been found very likely to be due to the emission of anthropogenic greenhouse gases [6, pp 2, 10].

In order to ensure long-term energy supply and to mitigate the effects of climate warming [6, p.8] by cutting down on green house gas emissions renewable energy carriers (e.g. wind, solar or geothermal energy or hydropower) must be used.
The energy output of some of these alternative energy sources (e.g. wind, solar power) varies strongly with time but excess energy can be converted into a storeable form, e.g. chemical energy. Hydrogen or hydrocarbons are conceivable as storage compounds because they can be easily used in combustion engines or fuel cells. The various types of fuel cells[1] are particularly interesting thanks to their high efficiency compared to combustion engines.

Electrolysis is a means to accomplish this conversion. The electrochemical splitting of water yields hydrogen:

$$H_2O \longrightarrow H_2 + \tfrac{1}{2}O_2 \tag{1.1}$$

Electrolysing CO_2 gives CO:

$$CO_2 \longrightarrow CO + \tfrac{1}{2}O_2 \tag{1.2}$$

which can subsequently be fed into a Fischer-Tropsch process that yields synthetic hydrocarbon fuels:

$$\underbrace{CO + H_2}_{\text{syngas}} \longrightarrow \text{hydrocarbons} \tag{1.3}$$

---

[1]Polymer Electrolyte Membrane Fuel Cells (PEM-FCs) could be used in vehicles, for example. Direct Methanol Fuel Cells (DMFCs) can be designed to be small and mobile (e.g. for camping or use on leisure boats). Solid Oxide Fuel Cells (SOFCs) are suitable as stationary power and heat sources.

1.2 High temperature water electrolysis with solid oxide electrolysis cells (SOECs)

1.2.1 Why SOECs?

High temperature electrolysis with SOECs offers some fundamental advantages over electrolysis at lower temperatures.

Thermodynamics Electrolysing water at higher temperatures can be advantageous from a thermodynamical point of view. The reaction taking place at the temperature T can, according to [7], be expressed as

$$H_2O + \text{electrical energy } \Delta G + \text{heat } T\Delta S \longrightarrow H_2 + \tfrac{1}{2}O_2 \tag{1.4}$$

For the decomposition of water, the change of entropy ΔS is positive. This is reasonable if we consider the configurational entropy $S = k \ln W$ (k is Boltzmann's constant, W the configurational weight) - the products (1,5 molecules) have more degrees of freedom than the substrate (1 molecule). Therefore, at higher temperatures the free enthalpy

$$\Delta G = \Delta H - T\Delta S \tag{1.5}$$

required to split water becomes lower due to the increasing entropy term $T\Delta S$ (ΔH is the reaction enthalpy for the decomposition of H_2O). This is depicted in fig. 1.1.
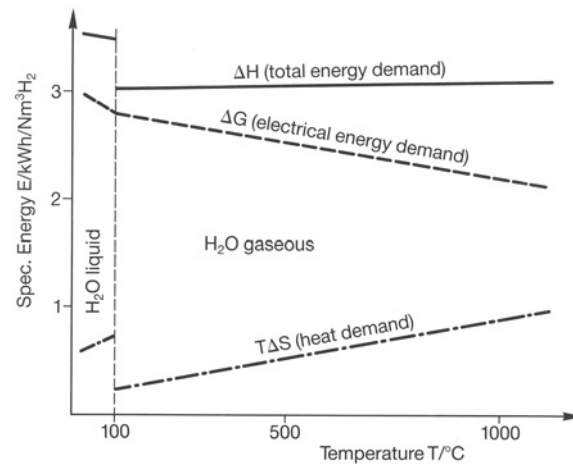
Figure 1.1: The thermodynamics of water splitting [8].

Since ΔG is proportional to the cell voltage ΔE_{cell} according to

$$\Delta G = -zF\Delta E_{\text{cell}} \tag{1.6}$$

(with z being the number of exchanged electrons and F being the Faraday constant), the cell voltage will decrease at higher temperature because a larger part of the energy needed to split H_2O is contributed by heat than at lower temperatures.

This effect can also be expressed by considering the thermodynamic (=theoretical) efficiency, ξ_{SOEC}, which is the reciprocal of a fuel cell's efficiency [9, p 25], ξ_{SOFC}:

$$\xi_{SOEC} = \frac{\Delta H}{\Delta G} \tag{1.7}$$

As ΔH remains almost constant with T, the efficiency will increase if ΔG is lowered by the increasing entropy term $T\Delta S$ at higher temperature.

Owing to this, a CO_2-neutral electrolysis process is possible if electricity and heat can be provided from sustainable sources. Waste heat from industrial processes could also be utilized to heat the cell (e.g. [10, 11]).
Moreover, the inevitable Joule heat can be the electrolyzer's exclusive heat source. The potential at which the generated Joule heat in the cell and the heat consumption for electrolysis, $\Delta_f H$ are equal, is referred to as the thermoneutral potential V_f [12]:

$$V_f = \frac{\Delta_f H}{zF} \tag{1.8}$$

Kinetics The kinetics of electrode reactions is faster at higher temperatures, resulting in smaller overpotentials. Two typical processes can be considered as examples.
First, the conductivity σ of an ion conductor increases exponentially with temperature according to

$$\sigma = \sigma_0 \cdot e^{-\frac{E_a}{kT}} \tag{1.9}$$

assuming that the activation energy E_a remains constant (σ_0 is the limiting conductivity).
Second, an activation-controlled electron transfer process at an electrode can be described by the Butler-Volmer model [13, p 130]. The reduction rate constant k'_{rd} is expressed as

$$k'_{rd} = k^{0\prime} \cdot e^{-\frac{\alpha zF}{RT}\left(E - E^{0\prime}\right)} \tag{1.10}$$

with the pre-exponential factor $k^{0\prime}$, the electron transfer coefficient α, the potential E and the potential at standard concentrations $E^{0\prime}$ [13, p 133]. From equation 1.10 it can be seen that the rate constant for this process increases exponentially with temperature as well.

For the above thermodynamic and kinetic reasons raising the temperature is favourable and is only limited by the high temperature stability of the materials used for building the SOEC.

1.2.2 State-of-the-art of SOECs for water electrolysis

The discovery of the decomposition of liquid water by an electric current dates back to the late 18th century - although it seems to be not entirely certain to whom it has to be attributed [14]. Possible discoverers include William Nicholson and Anthony Carlisle in 1800 [15] and Johann Wilhelm Ritter [16], also around 1800. Unfortunately, no original literature, that could clarify the situation, could be found. The term "to electrolyze", however, was suggested by Michael Faraday in 1837 and can be found in Faraday's original paper [17].
Even though the underlying phenomenon was discovered over 200 years ago, only two types of electrolyzers are commercially available: alkaline electrolyzers [18] and polymer electrolyte membrane (PEM) electrolyzers (see for example [19]). The research interest in SOECs has increased in the past decade [12] but they are not commericalized to date [18].

Research on Solid Oxide Electrolysis Cells is supported by government programmes such as the RelHy programme [20] and the Fuel Cells and Hydrogen Joint Undertaking (FCH JU) [21], funded by the European Commission or the U.S. Department of Energy within the Nuclear Hydrogen R+D plan [11].

Table 1.2 (page 6) gives a rough overview over the research activies on the field of SOECs (abbreviations are explained in table 1.1).

Table 1.1: Abbreviations used in table 1.2

Abbreviation	Meaning
YSZ	yttria-stabilized zirconia
TZ3Y	tetragonal zirconia with 3% Y_2O_3
ScSZ	scandia-stabilized zirconia
CGO	= GDC, gadolinia-doped CeO_2
SDC	samaria-doped CeO_2
LSM	La-doped Sr manganite
LSCM	$La_xSr_{1-x}Co_yMn_{1-y}O_{3-\delta}$
LSF	La-doped Sr ferrite
LSCF	$La_xSr_{1-x}Co_yFe_{1-y}O_{3-\delta}$
Ref.	Reference

Table 1.2: Overview of SOEC systems tested in literature.

Cathode	Electrolyte	Anode	$T/°C$	Comment	Year	Author's affiliation	Ref.
Ni/YSZ or Co/YSZ	YSZ	$PrCoO_3$	800-1200	single cells, stacks	1969	General Electric Research and Development Center, USA	[22]
Ni/YSZ	YSZ	ZrO_2/In_2O_3/Co-Pr-oxide, Pr-oxide	1000	7-cell stack	1981	Westinghouse, Inc., USA	[23]
?	YSZ	?	1000	1000h long-term test of a cell; test of tube with 10 cells, plant concept developed	1985	Dornier System GmbH, GER	[24]
porous Pt	$SrCe_{0.95}Yb_{0.05}O_{3-\delta}$ (H^+ conductor)	porous Pd	750		1986	Tottori University, JP	[25]
Ni cermet	YSZ	Sr-modified La manganite	800-1050	single tubular cells	1986	Westinghouse, Inc., USA	[26]
Pt or Ni/YSZ	YSZ or SDC	LSM or LSC	800, 1000		1996	Kyushu University, JP	[27]
Ni/YSZ	YSZ	$La_{0.9}Sr_{0.1}MnO_3$ or Sr-doped La cobaltite or Non-doped cobaltite	1000		1997	Electrotechnical Laboratory, Tsukuba-shi, JP	[28]
Pt/ $SrZr_{0.9}Yb_{0.1}O_{3-\delta}$	$SrZr_{0.9}Yb_{0.1}O_{3-\delta}$ (H^+ conductor)	Pt/ $SrZr_{0.9}Yb_{0.1}O_{3-\delta}$ cermet	460-600		2001	Toyota; Nagoya University, JP	[29]
$(CeO_2)_{0.8}(SmO_{1.5})_{0.2}$ with nm-sized Ni catalyst	YSZ	Porous Pt or $La_{0.6}Sr_{0.4}CoO_3$	900		2004	University of Yamanashi, JP	[30]
Ni/YSZ	YSZ or ScYSZ	LSM	800-900	commercial SOFC by Ceramatec, Inc. used as SOEC	2005	Idaho National Engineering and Environmental Laboratory; Ceramatec Inc; USA	[31]
Ni/YSZ	YSZ	LSM/YSZ	750, 850		2006	DTU Risø and Lyngby, DK	[32]
Ni/YSZ	ScSZ	Sr-doped manganite/zirconia//Sr-doped manganite/cobaltite	800-900	10-cell planar SOEC stack by Ceramatec Inc.	2007	Idaho National Laboratory; Ceramatec; FLUENT, Inc, USA	[33]

Table 1.2: Overview of SOEC systems tested in literature.

Cathode	Electrolyte	Anode		$T/°C$	Comment	Year	Author's affiliation	Ref.
$La_{0.35}Sr_{0.65}TiO_3/Ce_{0.5}La_{0.5}O_{2-\delta}$ (50:50) or Ni/YSZ	YSZ	$La_{0.8}Sr_{0.2}FeO_{3-\delta}$ $La_{0.7}Sr_{0.3}Cu_{0.1}Fe_{0.9}O_{3-\delta}$ $La_{0.6}Sr_{0.4}Co_{0.2}Fe_{0.8}O_{3-\delta}$ $La_{0.8}Sr_{0.2}MnO_{3-\delta}$	or or or	650-850	Stack	2007	Pacific Northwest National Laboratory; National Energy Technology Laboratory, USA	[34]
Ni/YSZ	YSZ	LSM		800-900	commercial SOFC by HTCeramics used as SOEC	2008	European Institute for Energy Research (EIfER), GER	[35]
$(La_{0.75}Sr_{0.25})_{0.95}Mn_{0.5}Cr_{0.55}O_3$ (LSCM) or Ni/YSZ or LSCM/CGO or LSCM/YSZ or LSCM	YSZ	LSM/YSZ or LSF		750-1000		2008	University of St. Andrews, UK	[36]
Ni/CGO	TZ3Y	$Nd_2Ni_{4+\delta}$		750-850	commercial cathode and electrolyte by H.C. Starck Ceramics	2009	Université de Bordeaux, Commissariat à l'Energie Atomique (CEA), FR	[37]
Ni/YSZ	YSZ	LSM/LSCF		800-850		2009	Deutsches Zentrum für Luft- und Raumfahrt (DLR), GER	[38]
Ni/Ni cermet	ScSZ	Sr-doped manganite		800-850	commercial SOFCs by Ceramatec, Inc. used in an SOEC stack	2009	Idaho National Laboratory; Ceramatec Inc., USA	[39]
$Gd_{0.4}Ce_{0.6}O_{2-\delta}/65\%NiO$ $35\%Gd_{0.1}Ce_{0.9}O/NiO$	$Sc_{0.2}Ce_{0.01}Zr_{0.79}O_{2-\delta}$	$La_{0.6}Sr_{0.4}Co_{0.2}Fe_{0.8}O_{3-\delta}$		800		2010	Energy Research Center of the Netherlands (ECN), NL	[40]
Ni/YSZ	YSZ	LSM		650-800		2011	Korea Institute of Energy Research, KR	[41]
Ni/YSZ	YSZ	$(La_{0.8}Sr_{0.2})_{0.95}MnO_3$ or $La_{0.65}Sr_{0.3}MnO_3$ or $(La_{0.8}Sr_{0.2})_{0.95}FeO_{3-\delta}$ or $La_{0.65}Sr_{0.3}FeO_{3-\delta}$ or $(La_{0.6}Sr_{0.4})_{0.98}Fe_{0.8}Co_{0.2}O_{3-\delta}$		800	1" diameter button single cell modules, 3-cell-stacks, 10-cell-stacks	2011	University of California, San Diego, USA	[42]
$La_{0.2}Sr_{0.8}TiO_{3+\delta}/Ce_{0.8}Gd_{0.2}O_{2-\delta}$ composite	YSZ	$(La_{0.8}Sr_{0.2})_{0.95}MnO_{3-\delta}$		700		2012	Hefei University of Technology; University of Science and Technology of China, Hefei, CN	[43]

In order to assess a material's potential as an SOEC cathode, the connection between overvoltage and current density associated with the evolution of hydrogen has to be known. Unfortunately, attempts to compare the different studies from this standpoint are in vain for the following reasons:

- In some of the studies cited in table 1.2 cathodic overvoltages were not measured.

- In all of the studies porous cathode materials were used. As their inner surface is unknown and depends strongly on the production process, it is challenging to compare current densities obtained in different studies.

- In different studies the measurements were performed at different temperatures.

The most common hydrogen electrode for both SOFCs and SOECs is the Ni/YSZ cermet [12]. However, it has shown some disadvantages as an SOEC cathode.

- An asymmetric current-voltage curve showing a diffusion limited current was reported in reference [28].

- Degradation in steam atmosphere, which could be due to surface oxidation of the Ni particles [27], was observed in different studies [27, 34, 44, 45]. It was found to be higher in electrolysis mode than in fuel cell mode [45]. Also, Ni/YSZ has a higher activity for H_2 oxidation than for steam electrolysis [34]. Furthermore, degradation due to Si compounds emitted by glass sealings was reported by [45].

Therefore, investigating new candidates for SOEC cathode materials is a highly interesting issue. Geometrically well-defined thin film electrodes offer a powerful tool for such studies since they allow to accurately determine current densities. The use of a well-defined model-type working electrode measured versus a porous counter electrode with a negligible polarization resistance offers the opportunity to evaluate the voltage drops at the working electrode. Thus the driving force of water-splitting becomes determinable which is a tremendous advantage for an electrochemical interpretation of results.

1.3 Perovskite-type thin film electrodes and the aim of this work

Acceptor-doped perovskite-type compounds are promising materials for SOEC cathodes. Their ability to conduct oxygen ions as well as electrons gives them a fundamental advantage over the Ni/YSZ cermet: Oxygen ions can be incorporated on the whole surface of the material, whereas on a Ni/YSZ electrode the reaction can only occur along the triple phase boundary (TPB). A material that has shown sufficient stability under reducing conditions is the 40% Sr-doped La ferrite, $La_{0.6}Sr_{0.4}FeO_{3-\delta}$ (LSF64). Its decomposition oxygen partial pressure was found to be below 10^{-20} bar in a temperature range between 773 and 1173 K [46].

Studies on the mechanism and the kinetics of oxygen reduction on LSF64 dense thin-film microelectrodes under oxidising as well as under reducing conditions are a highly interesting topic [47]. From these investigations insights into the fundamentals of the electrochemical processes in and on this material are expected. With the background of a basic understanding of electrode kinetics on model-type thin film electrodes the

investigations of the behaviour of LSF64 cathodes under real SOEC conditions, i.e. producing detectable amounts of H_2, is a promising approach from both a fundamental and an application point of view.

In the light of these considerations - from sustainability to testing LSF64 on an actual model type SOEC - the aims of this work are:

- Conducting first investigations (electrochemical impedance spectroscopy (EIS) and current-voltage measurements) on 5×5 mm, symmetric cells (LSF64-YSZ-LSF64) and comparing them with the results from the measurements on micro-electrodes [47].

- Preparing a macroscopic SOEC (around 1 cm in diameter) and finding an experimental setup suitable for EIS and current-voltage measurements during electrolysis of water or CO_2 and detection of the produced gases. The focus is on trying to relate the voltage drop at the LSF64 electrode to the current density and the amount of gas produced.

2 Theoretical aspects

2.1 Materials

The materials used in this work and the crystal structures they exhibit (perovskite and fluorite structure) will be briefly introduced here.

Table 2.1 summarizes some of these two structures' features, figures 2.1 and 2.2 illustrate the arrangement of the atoms in the unit cells with different atoms in the origin of the unit cell.

Table 2.1: Some properties of the perovskite ([48, pp 81-83], [49, pp 53-56]) and fluorite ([48, pp 78-81], [50], [51, p 712]) structures. The symbol $CN(A/X)$ denotes the coordination of e.g. A-atoms by X-atoms.

	perovskite structure	fluorite structure
eponymous compound	$CaTiO_3$	CaF_2
general formula	ABX_3 A ... a large cation, e.g. an alkali metal, an alkaline earth metal or a rare earth metal B ... a small cation, e.g. a transition metal X ... e.g. oxygen or a halogen The charges of the cations can range from +1 to +5. Perovskites can have mixed cation lattices (e.g. LSF64) as well as mixed anion lattices (e.g. $BaScO_2F$).	AB_2 A ... cation B ... anion
examples	$\overset{+2}{\text{Sr}}\overset{+4}{\text{Ti}}O_3$, $\overset{+1}{\text{Na}}\overset{+5}{\text{W}}O_3$, $\overset{+3}{\text{La}}\overset{+3}{\text{Al}}O_3$, $\overset{+1}{\text{Cs}}\overset{+2}{\text{Hg}}Cl_3$, $\overset{+2}{\text{Ba}}\overset{+3}{\text{Sc}}O_2F$	SrF_2, $BaCl_2$, UO_2, CeO_2, Y_2O_3-doped ZrO_2
one way of describing the structure	B ... primitive cubic lattice A ... in the center of the cube X ... in the middle of each edge see fig. 2.1, left	A ... face-centered cubic lattice B ... in all tetrahedral sites see fig. 2.2 (b)
another way of describing the structure	A ... primitive cubic lattice B ... in the center of the cube X ... in the middle of the faces see fig. 2.1, right	B ... primitive cubic lattice A ... half of the cubic sites see fig. 2.2 (a)
Coordination numbers and polyhedra	$CN(A/X) = 12$, cuboctahedron $CN(B/X) = 6$, octahedron	$CN(A/B) = 8$, cube $CN(B/A) = 4$, tetrahedron

Many compounds crystallizing in perovskite structure do not have an ideal cubic unit cell but show distortion. The lower symmetry influences their electric and magnetic properties (e.g. ferroelectricity in $BaTiO_3$). In order to estimate the amount of distortion,

9

the Goldschmidt tolerance factor t, which is calculated from the ionic radii of A, B and X ($r(A)$, $r(B)$ and $r(X)$, respectively) was introduced:

$$t = \frac{r(A) + r(X)}{\sqrt{2}\left[r(B) + r(X)\right]} \tag{2.1}$$

Compounds having a t-value between 0,89 and 1 are considered to exhibit ideal cubic symmetry, t-values of 0,8-0,89 indicate a distorted perovskite structure. The ilmenite structure is present if t-values lower than 0,8 are reached.
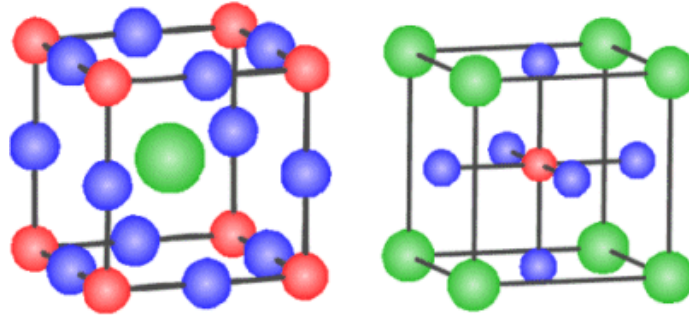[52, p 296]

Figure 2.1: The perovskite unit cell with red B-atoms (left) or green A-atoms in the origin (right). The blue spheres represent the X-atoms (from [53]). In the left figure the twelve-fold coordination of A by X is visible, whereas the right figure simplifies the visualization of the six-fold coordination of B by X.

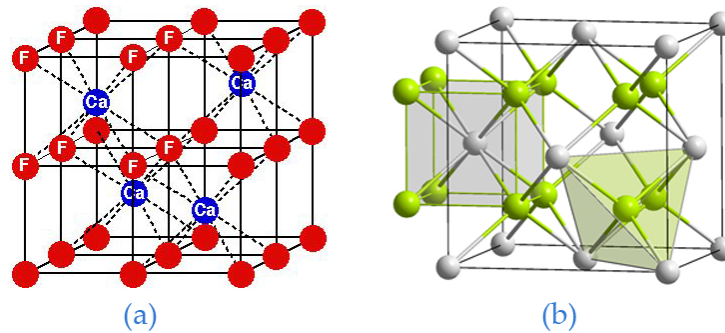(a)   (b)

Figure 2.2: (a): The fluorite unit cell with an anion in the origin (from [54]). (b): The fluorite unit cell with a cation (grey) in the origin. The cube and the tetrahedron show the 8-fold coordination of cations by anions and the 4-fold coordination of anions by cations, respectively (from [55]).
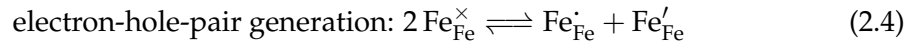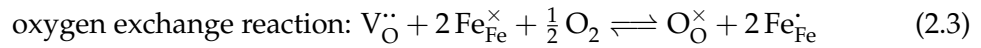
2.1.1 LSF64

Defect model Sr-doped La ferrites are good electronic and ionic conductors and show high catalytic activity. Their electronic and oxygen ion conduction properties are due to the mixed valence state of Fe on the B-site and the high oxygen non-stoichiometry [56].

The defect model suggested by [56] considers the defects (expressed in Kröger-Vink notation) $V_O^{\cdot\cdot}$ (oxygen vacancy), Sr'_{La} (Sr^{2+} on a La^{3+} site), $Fe_{Fe}^{\cdot}$ (Fe^{4+} on an Fe^{3+} site) and Fe'_{Fe} (Fe^{2+} on an Fe^{3+} site). The doping of $LaFeO_3$ with $SrFeO_3$ can (according to [46] or [57]) be expressed by

$$SrFeO_3 \xrightarrow{LaFeO_3} Sr'_{La} + Fe_{Fe}^{\cdot} + 3\,O_O^{\times}. \tag{2.2}$$
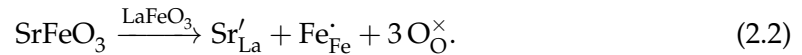
The defect equilibrium is then described by the following two reactions :

$$\text{oxygen exchange reaction: } V_O^{\cdot\cdot} + 2\,Fe_{Fe}^{\times} + \tfrac{1}{2}\,O_2 \rightleftharpoons O_O^{\times} + 2\,Fe_{Fe}^{\cdot} \tag{2.3}$$

$$\text{electron-hole-pair generation: } 2\,Fe_{Fe}^{\times} \rightleftharpoons Fe_{Fe}^{\cdot} + Fe'_{Fe} \tag{2.4}$$

The introduction of a cation on a lattice site that has a lower charge than the cation occupying this site in the pure compound is called acceptor doping, so LSF64 is an acceptor-doped lanthanum ferrite. The relative negative charge introduced by Sr ions occupying La sites is compensated by the formation of $Fe_{Fe}^{\cdot}$ or oxygen vacancies, which are connected by the oxygen exchange reaction (reaction 2.3).
This defect model was in good agreement with the experimental thermogravimetric (TG) and coulometric titration measurements performed in [56] and [46] (see figure 2.3).

In the oxygen content vs. oxygen partial pressure curve (figure 2.3) a plateau can be observed. In this range the oxygen stoichiometry[1] is almost independent from $p(O_2)$ which means that it is fixed by the dopant concentration via reactions 2.2 and 2.3. The plateau is located at $3 - \delta = 2,8$ corresponding to $\delta = 0,2 = [Sr]/2$ [56]. This means that the relative negative charge introduced by Sr'_{La} is compensated by oxygen vacancies only (and not by other positively charged defects) [58].

Crystal structure The strontium doped lanthanum ferrites $La_{1-x}Sr_xO_{3-\delta}$ show perovskite structure [46]. The distortion of the unit cell (which is cubic in the ideal perovskite) depends on the oxygen stoichiometry $3 - \delta$. A phase diagram for the $La_{1-x}Sr_xFeO_{3-\delta}$ system (x in $La_{1-x}Sr_xFeO_{3-\delta}$ vs. temperature T) was investigated in air by [59], showing a second-order phase transition of LSF64 from rhombohedral to cubic symmetry at 850±50°C (see figure 2.4).
For reducing conditions no x vs. T diagram is available in the literature. However, an x vs. $3 - \delta$ diagram was suggested by [60] (figure 2.5 (b)), involving a phase transition of LSF64 from rhombohedral to cubic near $\delta = 0,2$ and $x = 0,4$, which was reported as well by [46].
Figure 2.6 illustrates the transition from a cubic to a rhombohedrally distorted perovskite unit cell. In a second-order phase transition the first derivative of the chemical

---

[1]The oxygen non-stoichiometry is denoted by δ and corresponds to the concentration of oxygen vacancies: $[V_O^{\cdot\cdot}] = \delta$. The oxygen stoichiometry is a synonym for the oxygen content and is denoted by $3 - \delta = [O_O^{\times}]$.
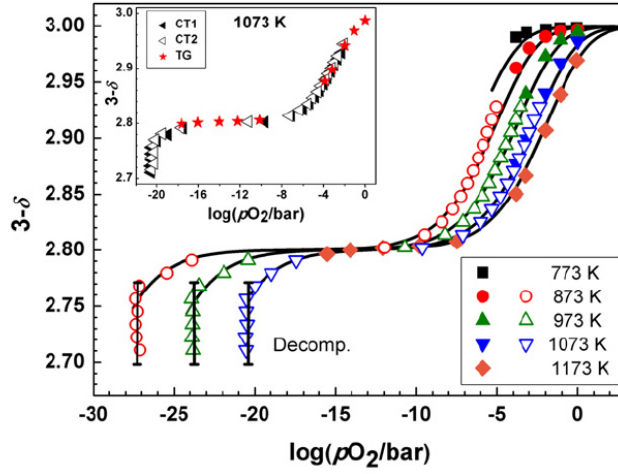
Figure 2.3: The oxygen stoichiometry $3 - \delta$ as a function of oxygen partial pressure. A plateau can be observed at $3 - \delta = 2,8$. The black lines represent calculated values based on the defect model and are in good agreement with the experimental data (from [46]).
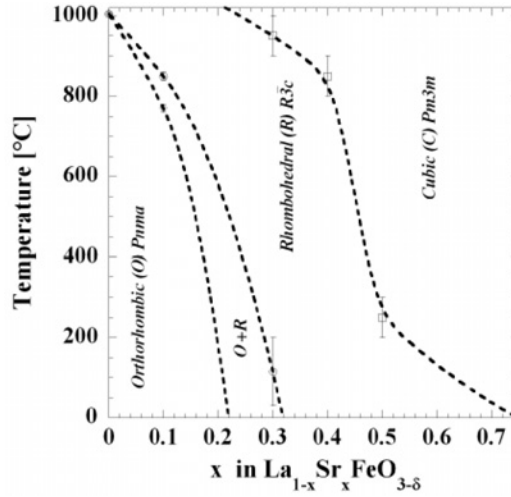

Figure 2.4: Pseudobinary phase diagram for the $La_{1-x}Sr_xFeO_{3-\delta}$ system ($x \leq 0,75$) in air (from [59]).

potential μ is continuous but the second derivative is discontinuous. For a crystalline solid this means that the crystal structure changes but without involving a discontinuity in the interaction between the atoms or the volume they occupy [61, p 130]. Here, the continuous change can be tracked by observing the rhombohedral angle α that was observed to approach 60° near $\delta = [Sr]/2$ [46].

Apart from the crystal structure as a function of oxygen content it would be interesting to estimate the temperature at which the phase transition occurs, for two reasons: First, the crystal structures of LSF64 that were found in other studies (at various temperatures) could be compared with the phase diagram in figure 2.5. Second, it could be favourable to keep the phase transition temperature in mind when interpreting the results of the measurements done in this work. The oxygen stoichiometry for a fixed
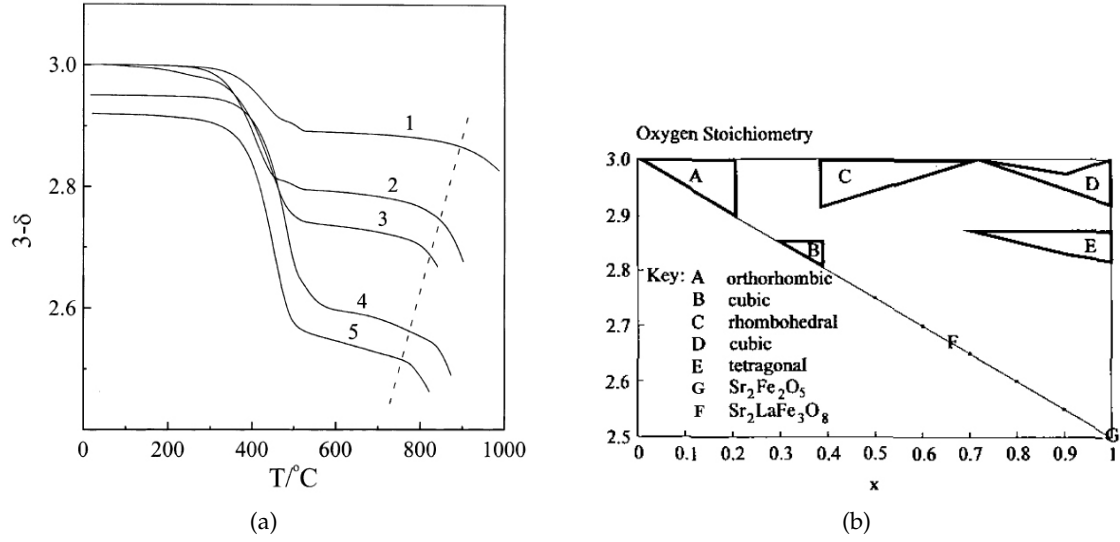
Figure 2.5: (a): The oxygen content of $La_{1-x}Sr_xFeO_{3-\delta}$ in an atmosphere containing 5% H_2 and 95% He. $x = 0,2$ (1), 0,4 (2), 0,5 (3), 0,7 (4) and 0,9 (5). The dashed line shows the approximate decomposition temperature [58]. (b): A phase diagram of the system $La_{1-x}Sr_xFeO_{3-\delta}$. The unlabeled regions are multiphase (modified from [60]). Point F in the diagram corresponds to $Sr_{2/3}La_{1/3}FeO_{8/3} = Sr_2LaFe_3O_8$.
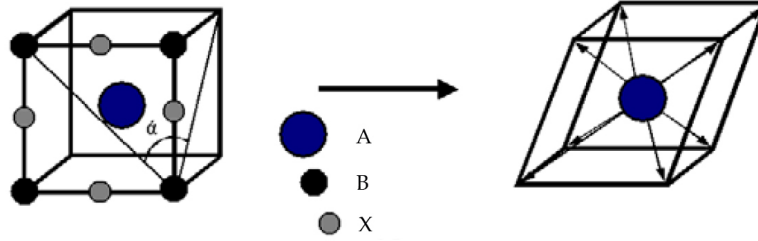

Figure 2.6: Illustration of the phase transition cubic $\rightarrow$ rhombohedral in the perovskite structure. The rhombohedral angle α is 60° in the cubic unit cell (figure modified from [62]).

value of x is a function of temperature and oxygen partial pressure in the surrounding atmosphere and is plotted versus temperature in figure 2.5 (a) for reducing conditions [58]. This diagram can be used to estimate the oxygen stoichiometry value at a certain temperature, which can then be used to find the corresponding phase in figure 2.5 (b): At 700°C, for instance, it can be read from fig. 2.5 (a) that the oxygen stoichiometry of LSF64 (line no. 2) is somewhere close to 2,8 which, according to figure 2.5 (b), corresponds to the cubic phase B. In contrast to this, an LSF64 sample equilibrated and quenched from 700°C in 5% H_2 and 95% He was found to exhibit rhombohedral structure in reference [58]. Two possible reasons for this discrepancy are the way of connecting the stoichiometry value to a temperature as described above, which is only qualitative, and the nature of the LSF system, which is very sensitive to oxygen stoichiometry and sample preparation [60].

Conductivity The conductivity as a function of oxygen partial pressure $p(O_2)$ was investigated by [58] (see figure 2.7), where three different regions of conductivity be-
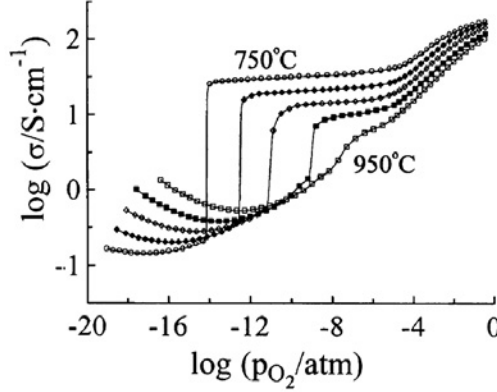
Figure 2.7: A plot of log total conductivity vs. the logarithm of oxygen partial pressure for LSF64 (from [58]).

havior could be distinguished. In the low $p(O_2)$ range the conductivity increases with decreasing $p(O_2)$ showing a slope of $-1/4$. This was interpreted as an indication for electronic conductivity. Furthermore, the material shows semiconducting behavior because the conductivity increases with temperature.

In the high $p(O_2)$ range the conductivity increases with $p(O_2)$ and a slope of $+1/4$, which shows that the majority charge carriers are electron holes ($h^{\cdot}$).

For the intermediate $p(O_2)$ range ($\approx 10^{-4}$ to 10^{-14}) the authors of reference [58] reported very slow kinetics, resulting in an equilibration that "would have taken an unreasonably long time of many hundred hours" per data point. Therefore, the conductivity data in this range of figure 2.7 do not represent equilibrium values. The reasons for this equilibration behaviour are unknown. The authors of reference [58] proposed that it could be related to the semiconductor to metal transition or other processes.

The same sluggish equilibration in this pressure range was also observed for other $La_{1-x}Sr_xO_{3-\delta}$, e.g. LSF37 ([58], [63]). In reference [63] LSF37 was found to exhibit brownmillerite-like structure at oxygen partial pressures lower than 1×10^{-4} atm while it showed perovskite structure at oxygen partial pressures above 1×10^{-4} atm. This structural transition was claimed to be reflected in the electrical properties of LSF37 [63]. It was however not noted explicitly that this phase transition is the reason for the equilibration behaviour in the intermediate pressure range.

For LSF64, this means that a phase transition from perovskite to brownmillerite at lower $p(O_2)$ values is conceivable and can be expected to have effects on its electronic properties.

The electronic and hole conductivity and its dependence on $p(O_2)$ can be explained if one supposes that the doping does not lead to the creation of holes and the concentration of oxygen vacancies is fixed by the dopant concentration, which is in agreement with the defect model [58]. If we consider hole conduction, i.e. at higher $p(O_2)$ values, the increase in $p(O_2)$ and therefore in the concentration of holes by the equilibrium

$$\tfrac{1}{2}\,O_2 + V_O^{\cdot\cdot} \rightleftharpoons O_O^{\times} + 2\,h^{\cdot} \tag{2.5}$$

[58] will be the only contribution to the increase in overall conductivity. Therefore, the conductivity dependence on $p(O_2)$ can be calculated from the mass action law [58] of

14

reaction 2.5:

$$K_p = \frac{[\text{h}^{\cdot}]^2[\text{O}_\text{O}^\times]}{p(\text{O}_2)^{1/2}[\text{V}_\text{O}^{\cdot\cdot}]} \tag{2.6}$$

$$[\text{h}^{\cdot}]^2 = K_p \cdot p(\text{O}_2)^{1/2}[\text{V}_\text{O}^{\cdot\cdot}][\text{O}_\text{O}^\times]^{-1} \tag{2.7}$$

$$[\text{h}^{\cdot}] \propto p(\text{O}_2)^{1/4} \tag{2.8}$$

If the overall conductivity σ is dominated by the hole conductivity σ_h it follows that $\log \sigma \propto +1/4 \log p(\text{O}_2)$, which can be observed in figure 2.7.
A similar argument applies for the electronic conduction at low $p(\text{O}_2)$, using the reaction

$$\text{O}_\text{O}^\times \rightleftharpoons \text{V}_\text{O}^{\cdot\cdot} + 2\,\text{e}' + \tfrac{1}{2}\,\text{O}_2 \tag{2.9}$$

which consequently leads to $[\text{e}'] \propto p(\text{O}_2)^{-1/4}$ and $\log \sigma \propto -1/4 \log p(\text{O}_2)$.

2.2 Experimental techniques

In this section some of the experimental techniques employed in this work will be introduced.

2.2.1 Mass spectrometry

Principle

Mass spectrometry (MS) is a widely applicable analytical method that allows (among other features) the qualitative and quantitative determination of a mixtures' composition, conclusions about a molecule's structure and the examination of solid surfaces [64, p 550].
A mass spectrometer consists roughly of the following parts [65, p 5.53]:

- sample inlet

- ion source

- analyzer

- detector

The sample is introduced into the machine via the sample inlet. In the ion source the molecules are ionized and broken into smaller pieces. The fragment ions are then accelerated into the analyzer, where they are separated according to their mass to charge (m/z) ratio. Finally the detector records the ion current for the desired m/z ratio. The results are presented graphically in a mass spectrum, a plot of the m/z ratio versus the ion current. Sample inlet, ion source, analyzer and detector are evacuated in order to avoid collisions between the fragement ions and the air particles. [65, pp 5.52-5.59]

Sample inlet and ionization In the sample inlet system, which is often coupled to the ion source, the sample is introduced, evaporated and subsequently ionized. There are inlet and ionization systems for gaseous, liquid and solid samples [66]. MS can also be used as an on-line detector for various separation methods such as gas chromatography (GC/MS), liquid chromatography (LC/MS) or capillary electrophoresis (CE/MS) [65, p 5.53]. Some examples for ionization methods are given in figure 2.8.

Atomic Ionization	Molecular Ionization		
	Sample Phase	Mode	Pressure[a]
Thermal ionization	Gas phase	Electron ionization	HV
Spark source		Chemical ionization (CI)	IV
Glow discharge		Photoionization (PI)	HV
Inductively coupled plasma		Field ionization	HV
Resonance ionization		Metastable atom bombardment	HV
	Solution phase	Thermospray	LV
		Atmospheric-pressure CI	AP
		Atmospheric-pressure PI	AP
		Electrospray	AP
	Solid phase	Plasma desorption	HV
		Field desorption	HV
		Secondary-ion MS	HV
		Fast atom bombardment	HV
		Matrix-assisted laser desorption	HV

[a] HV, high vacuum; IV, intermediate vacuum; LV, low vacuum; AP, atmospheric pressure.

Figure 2.8: Modes of ionization [67, p 16]

Analyzer   The analyzers used in mass spectrometry according to [68] are listed in figure 2.9.

Type of analyser	Symbol	Principle of separation
Electric sector	E or ESA	Kinetic energy
Magnetic sector	B	Momentum
Quadrupole	Q	m/z (trajectory stability)
Ion trap	IT	m/z (resonance frequency)
Time-of-flight	TOF	Velocity (flight time)
Fourier transform ion cyclotron resonance	FTICR	m/z (resonance frequency)
Fourier transform orbitrap	FT-OT	m/z (resonance frequency)

Figure 2.9: Types of analyzers use in mass spectrometry [68, p 86]

The resolution R of an analyzer is defined as

$$R = \frac{m}{\Delta m} \tag{2.10}$$

Δm is the difference in mass between the two peaks under consideration. The definition of m does not seem to be entirely unambiguous. In [67, p 68] and [65, p 5.60] m is the average of the two peak's masses whereas from [68, p 87] it can be concluded that m is the lower one of the two masses. The example given in [69, p 36], however, implies that m is the higher one of them.
"Two peaks are considered to be resolved if the valley between them is equal to 10% of the weaker peak intensity when using magnetic or ion cyclotron resonance (ICR) instruments and 50% when using quadrupoles, ion trap, TOF, and so on."[68, p 87] When determining the resolution using a single peak Δm is defined as the width of the peak at half of its height (full width at half maximum, FWHM) [68, p 87]. The abbreviations for these three definitions are $R^{10\%}$, $R^{50\%}$ and R^{FWHM} [66, p 10].
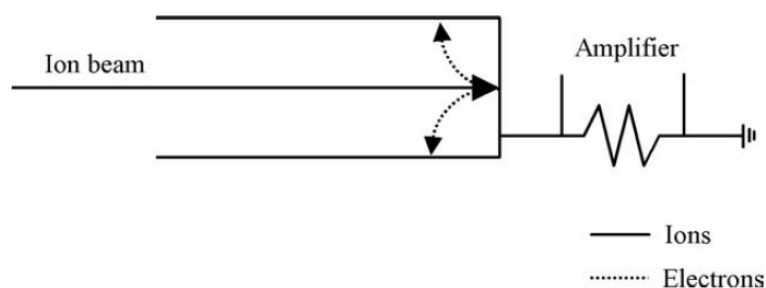For the same resolution the R^{FWHM} value is twice as much as the $R^{10\%}$ value [67, p 69].

16

Figure 2.10: Schematic drawing of a Faraday cup detector (from [68, p 176])
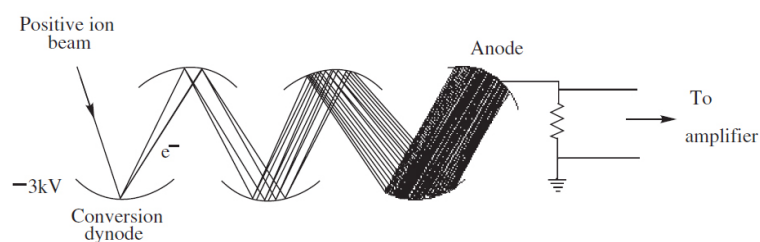

Figure 2.11: Schematic drawing of a secondary electron multiplier (SEM) (from [67, p 104])

Detector   Two commonly used detectors are the Faraday cup and the secondary electron multiplier (SEM).

The Faraday cup is a simple and robust tool for the detection of rather high concentrations of analyte. As depicted in figure 2.10 it consists of a steel cup with dimensions of about $2 \times 4 \times 4$ mm that is connected to ground potential via a large resistance. The analyte ions enter the cup and are neutralized on its inner walls, giving away to or extracting electrons from the metal (depending on their charge). This leads to a current passing through the resistor which can be measured as a potential drop over the resistor. [65, p 5.68] [68, p 176]

The secondary electron multiplier (SEM) is more sensitive than the Faraday cup, its working principle is sketched in figure 2.11. The SEM consists of an array of dynodes (usually copper beryllium electrodes), the first one (conversion dynode) being at a large negative potential (up to 3kV) versus the last one (anode). The potential of the dynodes in between increases from the conversion dynode to the anode. If an ion hits the conversion dynode it knocks electrons out of the metal, which are accelerated to the next dynode, emitting even more electrons upon impact. The resulting amplified electron current can then be measured. [65, p 5.68], [67, p 104]
SEMs have a limited lifetime due to neutralized particles that stay on the surface of the conversion dynode, influencing its work function [65, p 5.68].

17

Mass spectrometry with electron ionization and a quadrupole mass analyzer (EI-Q-MS)

This subsubsection describes EI-Q-MS, the method used in this work.

Electron Ionization Electron ionization (EI) is the most important ionization method for volatile compounds [69, p 17]. Figure 2.12 shows its working principle. The sample
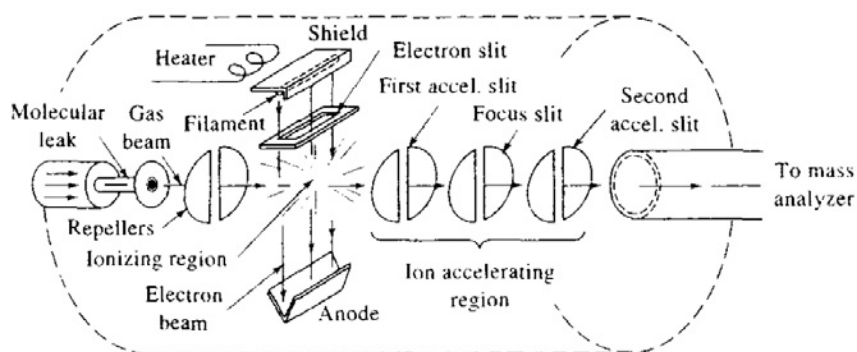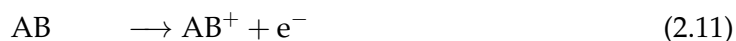

Figure 2.12: The principle of Electron Ionization (EI) (from [64, p 552])

molecule stream is struck in a 90° angle by the electrons that are emitted from the heated cathode made from e.g. W or Re and accelerated to the anode by a potential difference of around 50-100 V. Several reactions can occur:

$$AB \longrightarrow AB^+ + e^- \tag{2.11}$$
$$AB \longrightarrow AB^{2+} + 2\,e^- \tag{2.12}$$
$$AB + e^- \longrightarrow AB^- \tag{2.13}$$
$$AB \longrightarrow A^+ + B^- \tag{2.14}$$
$$AB \longrightarrow A^+ + B + e^- \tag{2.15}$$
$$AB + e^- \longrightarrow A^- + B \tag{2.16}$$

The most important one is reaction 2.11, the formation of a positive molecule ion. Apart from these processes, fragmentation occurs, so EI is called a "hard" ionisation method. However, the fragmentation is often useful, since it can provide structural information. [70, p 21] [69, p 17] [65, p 5.57] [68, p 17]

Quadrupole analyzer The quadrupole mass filter is the most widely used analyzer in MS [65, p 5.62]. Figures 2.13 and 2.14 show a schematic drawing and a photograph of a quadrupole, respectively.
It consists of four metal rods (A, B, C, D) forming a square. Rods A and C are connected to one pole of a voltage source, rods B and D to the other one. An alternating voltage is applied between rods A, C and B, D, meaning that rods A and C are always on the same potential, and rods B and D are on another potential. Additionally, a DC potential is superimposed on the AC potential. By adjusting the AC and DC voltages the rods A and C act as a highpass filter and the rods B and D are a lowpass filter, giving a bandpass filter that can be tuned to let only a certain m/z ratio pass. [69, pp 32,33] [67, pp 76,77]
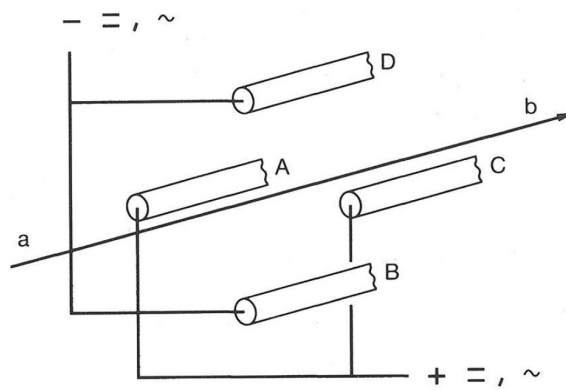
Figure 2.13: Scheme of a quadrupole mass analyzer (from [69, p 33])

Figure 2.14: Photograph of a quadrupole mass analyzer (from [71])

In practice the m/z ratios of interest are scanned for about 10-200 ms. A longer scan time increases the intensity of the signal [65, p 5.63].

Important parameters of a quadrupole analyzer are its mass range and its resolution. The mass range is determined by the maximum AC voltage and the diameter of the rod array [65, p 5.63]. A practical upper limit of m/z is 4000 [67, p 79].

The resolution R of a quadrupole mass analyzer is given by

$$R = \frac{m f^2 L^2}{zV} \tag{2.17}$$

where L is the length of the rods, f is the frequency of the AC voltage and V is the accelerating potential (zV is the kinetic energy of the ions). It follows from equation 2.17 that the resolution can be improved by using longer rods, a higher AC frequency or a lower acceleration potential [67, p 79]. Also, the resolution increases with increasing mass [65, p 5.63].

Some of the advantages of the quadrupole mass filter over other analyzers are its low price, its compactness and robustness [65, p 5.63] [67, p 80]. However, other detectors may have a wider mass range and resolution [68, p 89].

2.2.2 Interpretation of stationary current voltage-measurements

Since recording stationary current voltage (E-I)-curves and relating the amount of hydrogen produced to the E-I data is one of the goals of this work this subsection is about how these measurements can be interpreted and highlights the differences between Liquid and Solid State Electrochemistry with respect to this.

Electrode kinetics

The Butler-Volmer equation [13, p 134]

$$i = i_n \left[-\frac{c_O^s}{c_O^b} e^{-\frac{\alpha F}{RT}(E-E_n)} + \frac{c_R^s}{c_R^b} e^{\frac{(1-\alpha)F}{RT}(E-E_n)} \right] \tag{2.18}$$

is widely used to describe the current voltage-dependence of charge-transfer-controlled processes (for the meaning of the symbols see table 2.2). This model is applicable if the rate-determining elementary step (which is always a single-electron transfer [72, pp 108-109]) is the heterogeneous electron-transfer process [13, p 130].

If the overpotential

$$\eta = E - E_n \tag{2.19}$$

is applied the activation energy of the cathodic reaction changes by $\alpha F \eta$ [72, p 95]. The reaction Gibbs Energy[2] , $\Delta_r G$, of the rate determining step, changes by $F \eta$ (see the graph

---

[2]The reaction Gibbs energy is the sum of the chemical potentials μ_i of the products minus the sum of the chemical potentials of the reactants, where each of the μ_i is weighted with the respective stoichiometric coefficient ν_i [61, p 205]:

$$\Delta_r G = \sum_i \nu_i \mu_i. \tag{2.20}$$

For an electrochemical reaction μ_i has to be replaced by the electrochemical potential μ_i^*, and $\Delta_r G$ is replaced by $\Delta_r G^* = \Delta_r G + zFE$.

symbol	meaning
i	current density
i_n	exchange current density
c_O^s	concentration of the oxidized species at the electrode surface
c_O^b	concentration of oxidized species in the bulk of the electrolyte
α	symmetry factor = charge-transfer coefficient
E	potential
E_n	open-circuit potential
c_R^s	concentration of reduced species at the electrode surface
c_R^b	concentration of reduced species in the bulk of the electrolyte
F	Faraday's constant
R	gas constant
T	temperature

in [72, p 95]).

While in Liquid Electrochemistry this model often works fine, it cannot be applied in the case of oxygen incorporation into an LSF64 electrode on a YSZ electrolyte. Two reasons for this could be identified, they are presented in the following two paragraphs.

η **and current density i might be measured for different reactions**   As mentioned above, the BV-model states that $\Delta_r G^*$ of the rate limiting elementary step can be influenced by the electrode potential E. The reaction rate determines the current which is then related to E via the BV equation. However, in order to check if $\Delta_r G^*$ changes with E we do not need to know the mechanism, it is sufficient to consider the influence of E on the overall oxygen reduction reaction. If $\Delta_r G$ of the overall reaction is a function of E, the rate limiting step may be directly driven by E (BV case), but the rate may also be limited by another step (e.g. diffusion, another previous chemical reaction, etc.; non-BV case). If the overall reaction can't be driven directly by E, the rate limiting step cannot be, either, and the BV model is not applicable[3].

This difference will now be illustrated with an example for each case. An example for a half cell-reaction for which a **BV** description can be **possible** is the reduction of **oxygen on a Pt electrode in an acidic aqueous electrolyte**. The overall oxygen reduction reaction on Pt reads

$$\tfrac{1}{2}\,O_2 + 2\,e^- + 2\,H^+ \rightleftharpoons H_2O \tag{2.21}$$

If a potential E (giving an overpotential $\eta = E - E_n$) is applied to the electrode this will affect the charged species in the electrode. For low concentrations c_i, the electrochemical potential μ^* per mol of charged species i,

$$\mu_i^* = \underbrace{\mu_i^0 + RT \ln c_i}_{\mu_i} + z_i F E, \tag{2.22}$$

---

[3]An alternative formulation is: In a reaction mechanism there are "chemical" and "electrochemical" steps (not influenced by E and influenced by E, respectively), no matter if the reaction Gibbs energy of the overall reaction changes with E. The rate limiting step, however, can only be an "electrochemical" one, if $\Delta_r G^*$ of the overall reaction is a function of E.

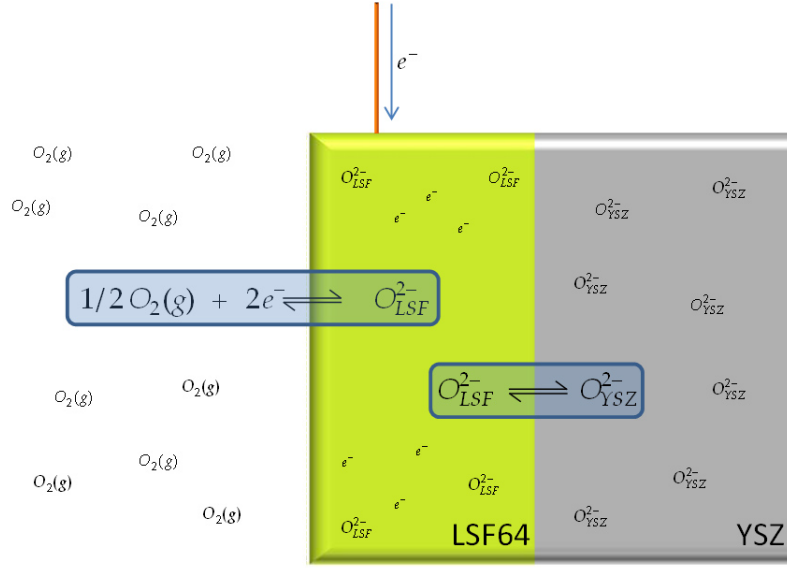Or: If no current flows if a potential is applied, it won't if we look at it in more detail, either.

Figure 2.15: Illustration of the oxygen reduction on LSF64. The second electrode and the rest of the circuit are not shown.

is the sum of the electrical potential energy $z_i F E$ (with z_i being the number of elementary charges of the species in question) and the chemical potential μ_i, which is in turn the sum of the chemical potential under standard conditions μ_i^0 and the term $RT \ln c_i$. A change of E will alter μ_i^* of the charged particles in the electrode by $z_i F \eta$. In reaction 2.21, the only charged species in the electrode, whose electrochemical potential will rise upon cathodic polarization of the electrode, are the electrons, changing $\Delta_r G^*$, shiftig the equilibrium 2.21 to the right-hand side.

This consideration shows that the overall reaction can be driven by E directly. If now a charge-transfer step is rate limiting, the current-overpotential behaviour can be modelled by the BV equation (and this can actually be done [73, p 90]).

When **oxygen is reduced on a solid state MIEC** such as LSF64, it can not only be incorporated via the triple phase boundary (gas/electrode/electrolyte), as it is the case for the Pt/O$_2$-half cell described above, but also via the bulk of the electrode material, thanks to the MIEC's ability to conduct electronic as well as ionic charge carriers. Due to this reaction path, the oxygen incorporation **can not be described by the BV model**. This will be illustrated in the following paragraph.

While in a Pt/O$_2$-half cell the reaction occurs at one single triple phase interface, an O$_2$/LSF64/YSZ-half cell contains two interfaces which have to be passed by oxygen on its way from the gas phase to the electrolyte: The gas/LSF64-interface and the LSF64/YSZ-interface (see figure 2.15). The two corresponding reaction equations are the oxygen incorporation reaction

$$\tfrac{1}{2} O_2 + 2 e^- \rightleftharpoons O_{LSF}^{2-} \tag{2.23}$$

and the oxygen transport reaction from LSF64 to YSZ,

$$O_{LSF}^{2-} \rightleftharpoons O_{YSZ}^{2-} \tag{2.24}$$

where O_{LSF}^{2-} and O_{YSZ}^{2-} denote the oxygen anion in LSF64 and YSZ, respectively. Depending on which of these two reactions contains the rate limiting step, two limiting cases can be distinguished:

- An elementary step of the oxygen incorporation reaction (reaction 2.23) can be rate limiting, while the transport of O^{2-} over the LSF64-YSZ interface is very fast.

  For the sake of simplicity, let's perform a gedankenexperiment and consider the influence of the electrostatic potential E on reactions 2.23 and 2.24 seperately. First, let's consider the change in $\Delta_r G^*$ with E for reaction 2.23. When an overpotential η is applied, G^* of the reactants changes by $2 \cdot 1 \cdot F\eta$ per mole due to the electrostatic contribution of the electrons. In contrast to the $O_2/Pt/H_2O$-half cell mentioned above, G^* of the products also changes because the product species O_{LSF}^{2-} are charged and they are located in the electrode. The change in G^* of the products is $2 \cdot F\eta$ per mol. Consequently, if only the electrostatic contributions to $\Delta_r G^*$, are considered, $\Delta_r G^*$ does not change at all. This leads to the conclusion that although the reaction equation contains charged species, the charge-transfer reaction 2.23 cannot be driven into one direction by electrostatic potential! It follows that there cannot be a rate limiting elementary step that is driven by E, either (although it might contain charged species and can therefore be termed an "electrochemical" step). In case of a rate limitation by reaction 2.23, the current-overpotential curve cannot be modelled by the BV equation, since the BV only considers the electrostatic influence on the change of $\Delta_r G^*$.

  Second, let's observe the influence of E on reaction 2.24. For this reaction $\Delta_r G^*$ can change with E because the electrochemical potential of O_{LSF}^{2-} will change by $2 \cdot F\eta$, whereas μ^* of the O^{2-} in YSZ will not. Hence, the applied potential drives the transport of O^{2-} from LSF64 into YSZ.

  Now we can end the gedankenexperiment and consider the effect of E on both reactions at the same time. As the overpotential is applied, O^{2-} ions are electrostatically pushed out of the electrode into the electrolyte (reaction 2.24). Since this reaction is very fast compared to the oxygen incorporation, the electrochemical potential of oxygen species is always equal in LSF64 and YSZ.

  So far, we have only discussed the purely electrostatic effect on $\Delta_r G^*$ when a potential is applied to an electrode because this is sufficient to check the applicability of the BV model. Now, in order to understand how the application of E *indirectly* drives the oxygen incorporation reaction, let's consider the following two effects. (a): As O^{2-} are transported from LSF64 to YSZ by the electrostatic force, the concentration of O_{LSF}^{2-} decreases and shifts the equilibrium 2.23 to the right-hand side. In other words, the change in E is translated into a change in $\mu_{O_{LSF}^{2-}}$, which drives the oxygen incorporation. (b): In the experiments performed in this work, E is changed by "pumping in" or "sucking out" charge carriers into/out of a material. Therefore, when applying a potential to the LSF64 electrode by means of a potentiostat, not only the electrostatic potential is changed, but also the concentration of electrons in LSF64. According to equation 2.22, $\mu_{e^-}^*$ changes by $RT \ln \Delta c_{e^-} - FE$, and so does G^* for the reactants in reaction 2.23 (if electrons are "pumped in", oxygen will be incorporated).

  To sum up, even though the electrostatic potential E does not influence the oxygen incorporation reaction 2.23 directly, it is driven indirectly via two effects: (a) the

decrease in concentration of O_{LSF}^{2-}, which is in turn caused by the effect of E on the oxygen transport reaction 2.24 and (b) the increase in electron concentration in LSF64.

The overpotential that is associated with the $\Delta\mu_{O_{LSF}^{2-}}$ is called stoichiometry polarization.

In order to predict the current-voltage behaviour of a system in this limiting case and to extract kinetic parameters (such as the activation energy) for the rate limiting step of the oxygen incorporation reaction from an experimental current-voltage curve a theory that connects η via $\mu_{O_{LSF}^{2-}}$ to those parameters is needed.

- The oxygen ion transport reaction via the LSF64-YSZ interface 2.24 can be rate limiting, while the oxygen incorporation reaction is very fast. In this case, the rate limiting reaction can be driven by E and the overpotential measured can be expected to lead to the current that is predicted by the BV model (BV case for interface).

In reality there can be mixtures of both limiting cases, where none of the two reactions 2.23 and 2.24 are clearly rate limiting. From studies on LSCF [74] showing that the LSCF-YSZ interfacial resistance is about two orders of magnitude smaller than the resistance associated with the oxygen incorporation reaction it can be expected that an LSF64/YSZ-half cell will be closer to the first limiting case (rate limiting step in oxygen incorporation) than to the second.

Similar considerations also apply to other mixed conduction materials and incorporation of oxygen from other compounds than O_2, e.g. water or CO_2.

Material changes with potential   The oxygen non-stoichiometry in LSF64 as an electrode on an electrochemical cell does not only change in response to different oxygen partial pressures in the surrounding gas (see the defect model, equation 2.3) but also as a function of applied potential. When a potential is applied the oxygen ions in LSF64 will start to move into the YSZ (see equation 2.24) and as a consequence oxygen will be incorporated into the material. If the oxygen incorporation is very fast the concentration of O^{2-} in LSF64 will not change. However, if the incorporation reaction is rate limiting, the concentration of O^{2-} in LSF64 will be lower than without the potential applied.

During a current voltage measurement the oxygen stoichiometry will therefore change with every pair of current/voltage values.

The parameters α and i_0 that can be obtained from the BV equation can thus be different for every oxygen non-stoichiometry. Consequently, even if a current-voltage curve has a shape that can be described by the BV equation the parameters α and i_0 are not materials properties because they cannot be attributed to a single "material", i.e. a certain value of δ.

Potential threshold

When electrolysing liquid water there is a minimum in the absolute value of potential in order to produce a significant current and gas stream [75, pp 4-5]. This is illustrated in the current-voltage diagram (2.16). This behaviour can be explained by the fact that
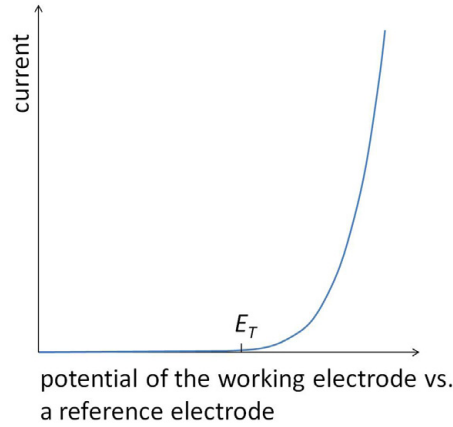
Figure 2.16: The electrolysis current as a function of the potential of the working electrode. E_T marks the threshold potential.

in liquid electrolysis evolving gas bubbles have to push against the external pressure p_{ex} in order to leave the electrode surface. For $p(H_2) < p_{ex}$ hydrogen can't form bubbles and its surface concentration increases, causing the Nernst potential to rise as well (the desorption current can practically be neglected). When $p(H_2) = p_{ex}$ (at the potential E_T) gas bubbles start to evolve and the current rises significantly.

In Solid State Electrochemistry, however, no potential threshold is expected since H_2 with low partial pressure is not forced to stay at the electrode surface but can desorb into the gas phase easily.

The potential measured across an electrochemical cell in DC measurements in different experimental setups

The potential drop measured across an electrochemical cell, ΔE_{cell}, can be split up into potential drops at the components of the cell (working electrode (WE), counter electrode (CE) and electrolyte) and the potential resulting from the $\Delta_r G$ for the overall reaction, ΔE_{Nernst}:

$$\Delta E_{cell} = \underbrace{IR_{CE}}_{\eta_{CE}} + \underbrace{IR_{electrolyte}}_{\eta_{electrolyte}} + \underbrace{IR_{WE}}_{\eta_{WE}} + \Delta E_{Nernst} \qquad (2.25)$$

In this work, η_{WE} and ΔE_{Nernst} are the quantities of interest - their sum is denoted $E_{LSF} = \eta_{WE} + \Delta E_{Nernst}$ in this work. All other contributions should be negligibly small or known and thus subtractable, which can be realized experimentally. Therefore, η_{CE} and $\eta_{electrolyte}$ will not be treated in this subsubsection.

The Nernst potential The equilibrium potential of the hydrogen-producing half-cell depends on the hydrogen partial pressure according to the Nernst equation. As in Liquid Electrolysis the produced gas is usually allowed to bubble freely the hydrogen partial pressure remains constant and only the gas flow changes. Therefore, the Nernstian contribution to the electrode potential does not change any more with potential once hydrogen production has started.

25

In the Solid State case, however, gaseous H_2O in a carrier gas stream is transformed into H_2 and its concentration changes according to the electric current flowing through the cell in a certain point on the current-voltage curve. For different electrode potentials the Nernstian contribution will therefore be different. For an electrolysis experiment this means that ΔE_{Nernst} can change as a function of time, which is symbolized in the following by $\Delta E_{\text{Nernst, initial}} \neq \Delta E_{\text{Nernst, final}}$.

Moreover, the Nernst potential will also be affected by the gas flow.

Overpotential at the WE η_{WE} can be composed of contributions from different processes requiring activation energy such as chemical reactions, transport processes or charge-transfer processes [72, p 23]. Here, only two of them are considered:

- the concentration overpotential $\eta_{\text{WE,c}}$

  If the concentration of electroactive species in the bulk, c_{bulk} is different from the concentration at the electrode surface, c_{surf}, a resistance due to sluggish mass transfer, $R_{\text{mass transfer}}$ arises which can be expressed as a concentration overpotential $\eta_{\text{WE,c}} = IR_{\text{mass transfer}}$ [72, pp 23,24].

- the overpotential associated with the charge transfer from electrode to the electroactive species, $\eta_{\text{WE,ct}}$ [72, pp 23,24].

In the following description η_{WE} and ΔE_{Nernst} will be listed for several measurement setups/situations encountered in this work, and compared with other setups.

electrode in "infinite" volume This setup is encountered if a tiny electrode is immersed in a very large volume so that concentrations in the bulk of the solution do not change during a measurement: $\Delta E_{\text{Nernst, initial}} = \Delta E_{\text{Nernst, final}}$. If $c_{\text{surf}} = c_{\text{bulk}}$, then $\eta_{\text{WE}} = \eta_{\text{WE,ct}}$, if $c_{\text{surf}} \neq c_{\text{bulk}}$ then $\eta_{\text{WE}} = \eta_{\text{WE,ct}} + \eta_{\text{WE,c}}$. The BV equation without or with concentration terms ("current-overpotential equation", [72, p 100]) can be used to interpret the current-voltage curve.

This case exists in Liquid Electrochemistry as well as in Solid State Electrochemistry (micro contact measurement instrument "I-Pot" [76], [47]).

"volume of fluid surrounding electrode small" In this case, the concentrations in the bulk of the electrolyte solution can change during a measurement. Hence, $\Delta E_{\text{Nernst, initial}} \neq \Delta E_{\text{Nernst, final}}$. The Nernst potential depends not only on the time that has passed since the start of the DC measurement but also on the flow of fluid in which the electrode is immersed. If the concentrations of the substances contributing to the overall cell reaction are known and only one redox couple is present, ΔE_{Nernst} can be calculated. If $c_{\text{surf}} = c_{\text{bulk}}$, then $\eta_{\text{WE}} = \eta_{\text{WE,ct}}$, if $c_{\text{surf}} \neq c_{\text{bulk}}$ then $\eta_{\text{WE}} = \eta_{\text{WE,ct}} + \eta_{\text{WE,c}}$.

This case is also found in both Liquid Electrochemistry and Solid State Electrochemistry. The Solid State case is realized in the SOEC sample holder (see subsection 3.3.2), if no leak between inner and outer gas chambers is present.

SOEC sample holder with leak The sample holder used for measurements on the model SOECs if there is a leak between inner and outer gas chambers. $\Delta E_{\text{mix, initial}} \neq \Delta E_{\text{mix, final}}$, where ΔE_{mix} indicates that the Nernst potential is replaced by a mixed

potential, due to more than one redox couples being present. Since the concentrations change during the measurement, the mixed potential changes as well.

If $c_{surf} = c_{bulk}$, then $\eta_{WE} = \eta_{WE,ct,mix}$, if $c_{surf} \neq c_{bulk}$ then $\eta_{WE} = \eta_{WE,ct,mix} + \eta_{WE,c,mix}$. All overpotentials are determined by the kinetics of the reactions between different redox couples (hence the subscript "mix").

macroscopic sample holder, one gas chamber The macroscopic sample holder used for measurements on LSF64-YSZ-LSF64 cells, see subsection 3.1.2. If currents are small, c_{bulk} does not change during the measurement because the gas consumed or produced is resupplied or diluted by convection immediately: $\Delta E_{Nernst,\, initial} = \Delta E_{Nernst,\, final}$. For high currents, c_{bulk} changes and since there is only one gas chamber, the substances at anode and cathode can mix, and the gas flow cannot compensate the concentration changes any more. Therefore, $\Delta E_{mix,\, initial} \neq \Delta E_{mix,\, final}$.

If $c_{surf} = c_{bulk}$, then $\eta_{WE} = \eta_{WE,ct,mix}$, if $c_{surf} \neq c_{bulk}$ then $\eta_{WE} = \eta_{WE,ct,mix} + \eta_{WE,c,mix}$.

2.2.3 Electrochemical impedance spectroscopy

Electrochemical Impedance Spectroscopy (EIS) is one of the major methods for the characterization of a solid's (di)electrical properties because under certain circumstances it allows the determination of materials constants such as the conductivity σ or the dielectric constant ϵ in different zones of a crystal as well as statements about the kinetics of transport processes.

In an EIS measurement an AC voltage with amplitude U_0 is applied to the sample and the resulting current (with amplitude I_0) is monitored as a function of time t. Then the impedance

$$Z = \frac{U_0}{I_0} \cdot e^{i\varphi}, \tag{2.26}$$

which, in contrast to $R = U(t)/I(t)$ is independent from time, is calculated from the phase shift φ between voltage and current.

Among other ways to graphically represent the results of these measurements the Nyquist and Bode plots are very common. In the Nyquist plot the real part of the impedance, $\mathrm{Re}(Z)$, on the abscissa is plotted against the negative imaginary part, $-\mathrm{Im}(Z)$, on the ordinate. The phase shift φ can be calculated from the angle between the abscissa and the line connecting the origin and the point $(\mathrm{Re}(Z), \mathrm{Im}(Z))$ using

$$\frac{\mathrm{Im}(Z)}{\mathrm{Re}(Z)} = \tan \varphi. \tag{2.27}$$

While in the Nyquist plot the frequency f of the AC voltage is shown only implicitly (different point-different frequency), the Bode representation consists of two plots with f given on the abscissa: f versus the absolute value of Z, $|Z|$, and a plot of φ as a function of f. Table 2.3 shows the impedance of different circuit elements as a function of frequency and the respective graphical representations in the Nyquist and Bode plot. [77, pp 15-17]

For the interpretation of an impedance spectrum an equivalent circuit has to be found. After normalization to geometric properties the parameters of this equivalent circuit

27

are materials properties and can be determined by fitting a calculated spectrum to the real data.

$R \parallel C$ elements can be employed as approximate descriptions of several electrochemical processes in solids, such as transfer of charge carriers in grains, grain boundaries or through interfaces, each process having a characteristic angular frequency $\omega_c = 1/RC$. Provided the respective ω_c values differ enough from each other the processes can be separated in the impedance spectrum.

Table 2.3: The impedance of different circuit elements and their representation in the Nyquist and Bode plots. Z' and Z'' denote the real and the imaginary part of the impedance (in arbitrary units), respectively.
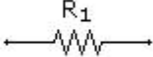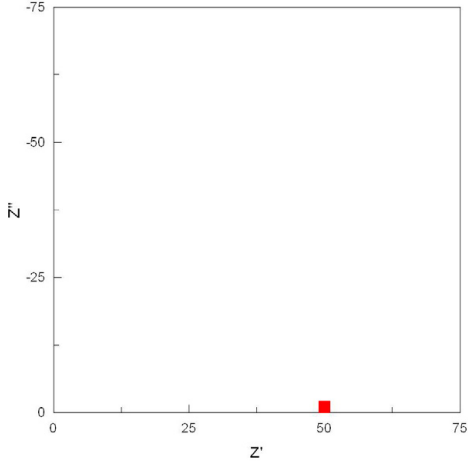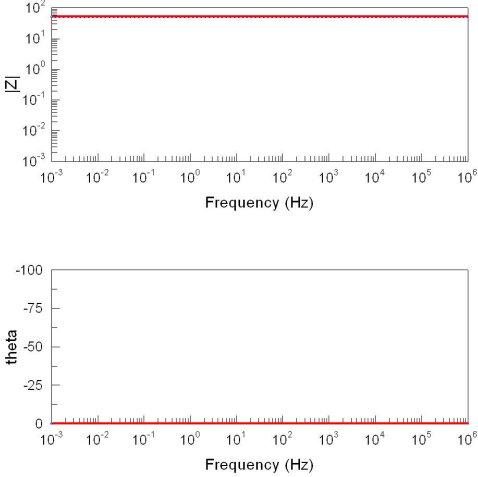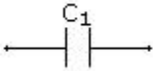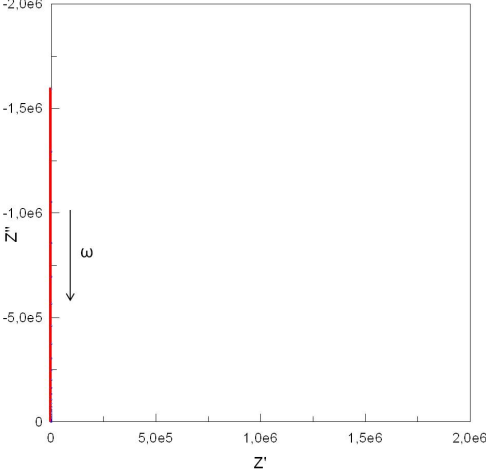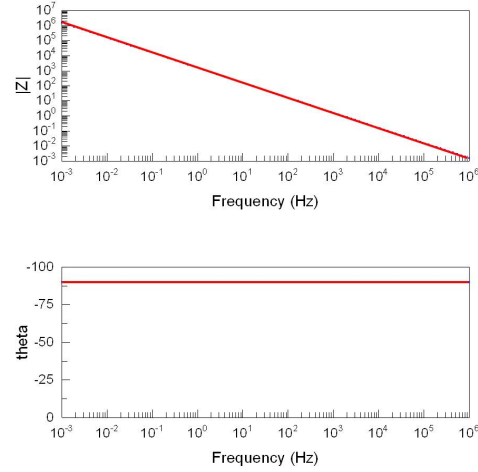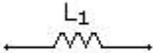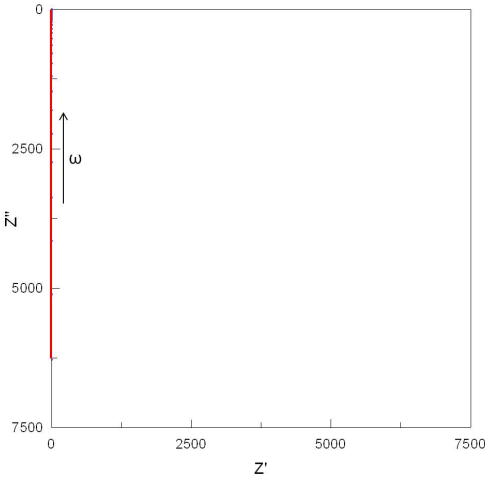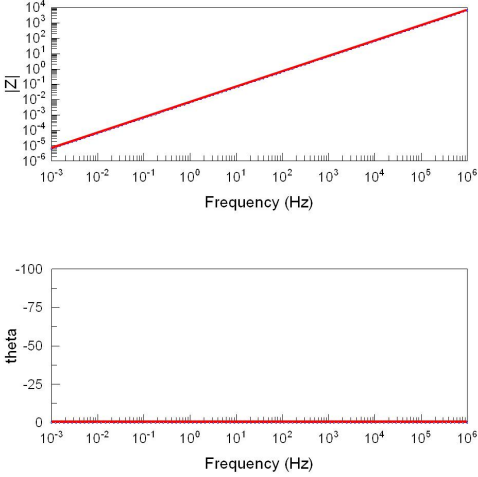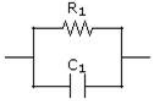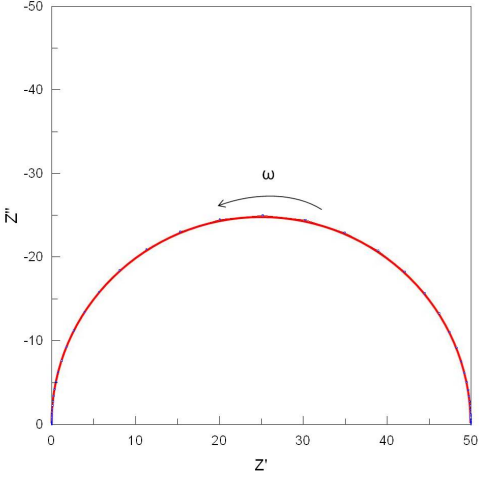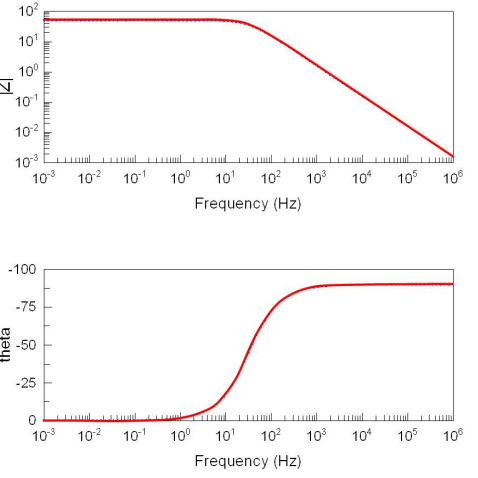
circuit element	impedance	Nyquist plot	Bode plot
R_1	$Z = R$		
C_1	$Z = \dfrac{1}{i\omega C} = -\dfrac{i}{\omega C}$		

Table 2.3: The impedance of different circuit elements and their representation in the Nyquist and Bode plots. Z' and Z'' denote the real and the imaginary part of the impedance (in arbitrary units), respectively.

circuit element	impedance	Nyquist plot	Bode plot

L_1

$$Z = i\omega L$$

R_1 C_1

$$Z = \frac{R}{1+\omega^2 R^2 C^2} - i\frac{\omega R^2 C}{1+\omega^2 R^2 C^2}$$

3 Experimental aspects

In this chapter the sample preparation and the measurement setups are described. Three different kinds of samples were prepared:

- Symmetric LSF64-YSZ-LSF64 cells for the pre-investigations of LSF64

- Symmetric cells with $La_{0,6}Sr_{0,4}Co_{0,2}Fe_{0,8}$ (LSCF6428), the anode material for the model-type SOECs on a polycrystalline YSZ electrolyte, were prepared with the main purpose of comparing the ohmic resistance of an LSCF6428 electrode with that of the LSF64 thin film electrode: During the preparation of each LSCF6428 electrode for an SOEC a symmetric LSCF6428-YSZ-LSCF6428 cell was also prepared in order to determine the impedance contribution of the LSCF6428 electrode via measurements on the symmetric cell. This ensures that neglecting the anode impedance (see end of chapter 1.2.2) versus the cathode impedance is justified for every SOEC sample ("anode quality test sample", samples YSZ_poly_12_LSCF - YSZ_poly_16_LSCF).

- Model-type LSF64-YSZ-LSCF solid oxide electrolysis cells

The gases used in this work are Ar (Alphagaz 1, Air Liquide), O_2 (Alphagaz 1, Air Liquide), N_2 (Alphagaz 1, Air Liquide), 1% O_2 in N_2 (obtained from Air Liquide) and 2,5% H_2 in Ar (technical gas "ARCAL 10", Air Liquide).

3.1 Symmetric LSF64-YSZ-LSF64 cells

3.1.1 Sample preparation

Eight of these samples were produced and named LSF64_001_1, LSF64_001_2, LSF64_001_3, LSF64_001_4, LSF64_002_1, LSF64_002_2, LSF64_002_3 and LSF64_002_4. The preparation procedure of these cells is sketched in figure 3.1. Single crystalline YSZ
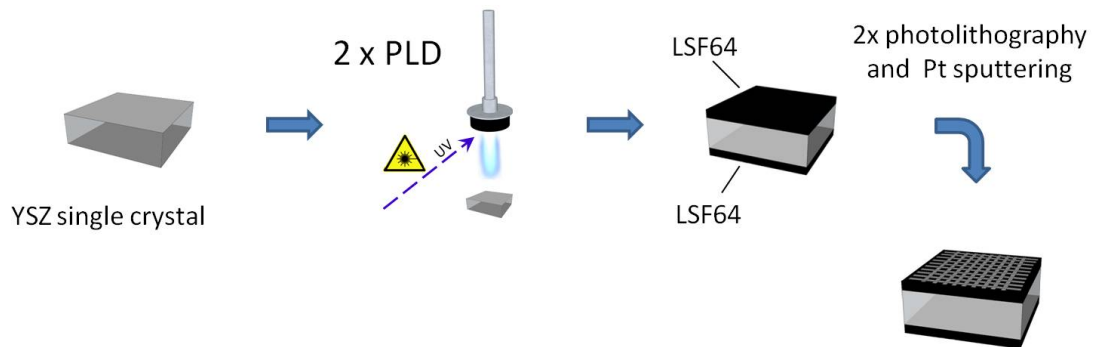

Figure 3.1: Sketch of the preparation procedure for symmetric LSF64-YSZ-LSF64 cells.

$(5 \times 5 \times 0,5$ mm, (100)-oriented), polished on both sides, was obtained from Crystec, Germany. LSF64 powder was prepared via a Pechini synthesis [78], the target for pulsed laser deposition (PLD) was obtained by subsequent pressing and sintering. LSF64 was then deposited on both sides (in two subsequent steps) by PLD (Kr/F excimer laser, Lambda COMPex Pro 205F, wavelength $\lambda = 248$ nm); samples and the respective PLD parameters are given in table 3.1. LSF64 could be deposited on one side of four samples in one step. The temperature of the sample was measured using a pyrometer (Strahlungspyrometer KT 19.99, Heitronics, Germany).

Table 3.1: Parameters for PLD, LSF64-YSZ-LSF64 cells.

sample name	parameter	value
all samples	desired film thickness/nm	200
	set temperature/°C	1200
	oxygen partial pressure/mbar	$4 \cdot 10^{-2}$
	pulse rate/Hz	10
	energy per pulse/mJ	400
	deposition time/min	40
	distance target-furnace/cm	5,5
	cooling rate/°C min^{-1}	12
first deposition on LSF64_001_1, LSF64_001_2, LSF64_001_3, LSF64_001_4		584
second deposition on LSF64_001_1, LSF64_001_2, LSF64_001_3, LSF64_001_4		670
first deposition on LSF64_002_1, LSF64_002_2, LSF64_002_3, LSF64_002_4	sample temperature/°C	580
second deposition on LSF64_002_1, LSF64_002_2, LSF64_002_3, LSF64_002_4		699

A Pt thin film was then deposited by magnetron sputtering (BAL-TEC MED 020 Coating System; Pt with 99,95% purity was obtained from Ögussa, Austria) and microstructured by means of lift-off photolithography to give a $10\,\mu m \times 10\,\mu m$ grid. The photolithography and sputtering process is shown schematically in figure 3.2, the parameters for photolithograpy are given in table 3.2, those for the sputtering process are listed in table 3.3. The sample (LSF64 layer on YSZ substrate) was first spincoated with photoresist (micro resist technologie ma-N 1420) and afterwards put on a hot plate to evaporate the solvent. Subsequently, a mask shading the areas where Pt deposition is desired was fixed on the sample. After exposing the sample (with mask) to the radiation of a high pressure Hg lamp that hardens the photoresist, the non-hardened photoresist was removed from the shaded areas with a developer solution (micro resist technologie ma-D 553S). A Ti layer (to promote adhesion), followed by a Pt layer was then deposited on the sample by magnetron sputtering. Finally the metal layers and the remaining photoresist were removed together by ethanol (EtOH) in an ultrasonic bath (lift-off). The success of the photolithography step was checked by optical microscopy (Zeiss Imager.M1m).
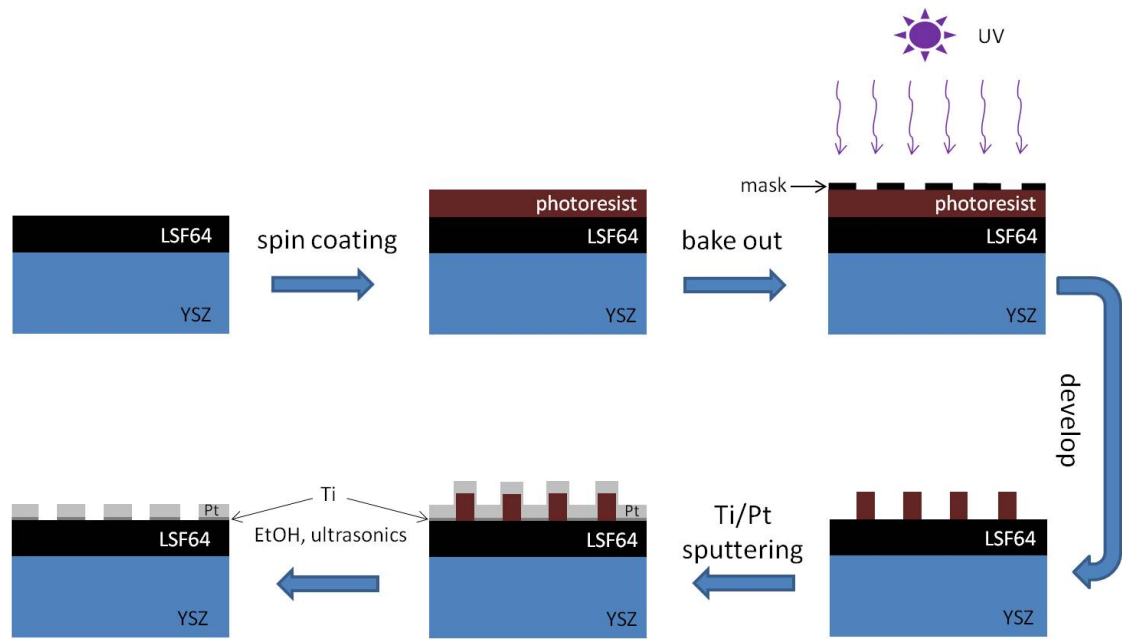
Figure 3.2: Sketch of the lift-off photolithography process for preparing LSF64-YSZ-LSF64 cells.

Table 3.2: Parameters for photolithography.

	parameter	value
spincoating	angular speed/rounds per minute	3000
	time/s	30
	volume of photoresist/µl	50-100
bake out time/min		2
bake out temperature/°C		100
UV exposure time/s		40
developing time/s		60-90

Table 3.3: Parameters for magnetron sputtering of Ti/Pt. The targets were cleaned by sputtering with the sample covered.

parameter	value	
	Ti	Pt
desired thickness of layer/nm	20	100
Ar pressure/mbar	7×10^{-3}	2×10^{-2}
current/mA	100	
target cleaning time/s	20	
sputtering time/s	150	

Due to problems during the sputtering process the Ti layer of one side of every sample can be expected to contain some TiO_2. This has to be taken into account when interpreting the measurement data of these samples.

3.1.2 Measurement setup

The measurements were carried out using the sample holder shown in figure 3.3. The parts in the heated area of the apparatus were made of inert materials (quartz glass for the tubes, rods, spacers, etc. and Pt for the metallic parts) to avoid any contamination of the sample. A Keithley SM2611A source meter unit and a Solartron SI 1260 Impedance/Gain-Phase Analyzer or a Novocontrol Alpha-A High-Performance Frequenzy Analyzer with 4-wire Impedance Test Interface were used for DC and AC measurements, respectively. In order to fix the sample between the washers the movable rod was slid towards the tip of the sample holder, pushing together the washers and the sample. Two Pt wires were fixed on each of the Pt sheets. In this way a four-point measurement, eliminating the impedance contribution of the Pt wires and the cables could be performed. In order to shield the sample from electric fields a wire gauze connected to ground potential was placed around the outer tube of the sample holder before inserting it into the furnace.

The furnace was set to 700°C leading to temperatures near the sample of around 650°C, measured with the thermocouple located beneath the sample. All measurements were done in a gas stream of 2,5 vol% H_2 and 97,5 vol% Ar that was bubbled through a gas washing bottle containing deionized water before reaching the sample holder. With a water partial pressure of 2,6453 kPa at 22 °C [79] and assuming that all gases are perfect gases this gives a gas mixture with approximately 2,4% H_2, 2,6% H_2O and 95% Ar.

The parameters for the DC measurements are given in table 3.4. The measurements started at the start potential E_{start} and ended at the potential E_{stop}. The acquisition time resolution is the time interval in which data points are recorded.

Table 3.4: Parameters for DC measurements on LSF64-YSZ-LSF64 samples.

parameter	value
measurement mode	potentiostatic, 2-wire
ΔE_{start}	-0,5 V
ΔE_{stop}	0,5 V
no. measurement points	20
acquisition time	60-5850 s
acquisition time resolution	0,5 s
temperature	$\approx 650°C$
gas flow of reducing gas mixture/bubbles per second	a few

The parameters for the EIS experiments are shown in table 3.5. Measurements were carried out in 2- or 4-wire mode.
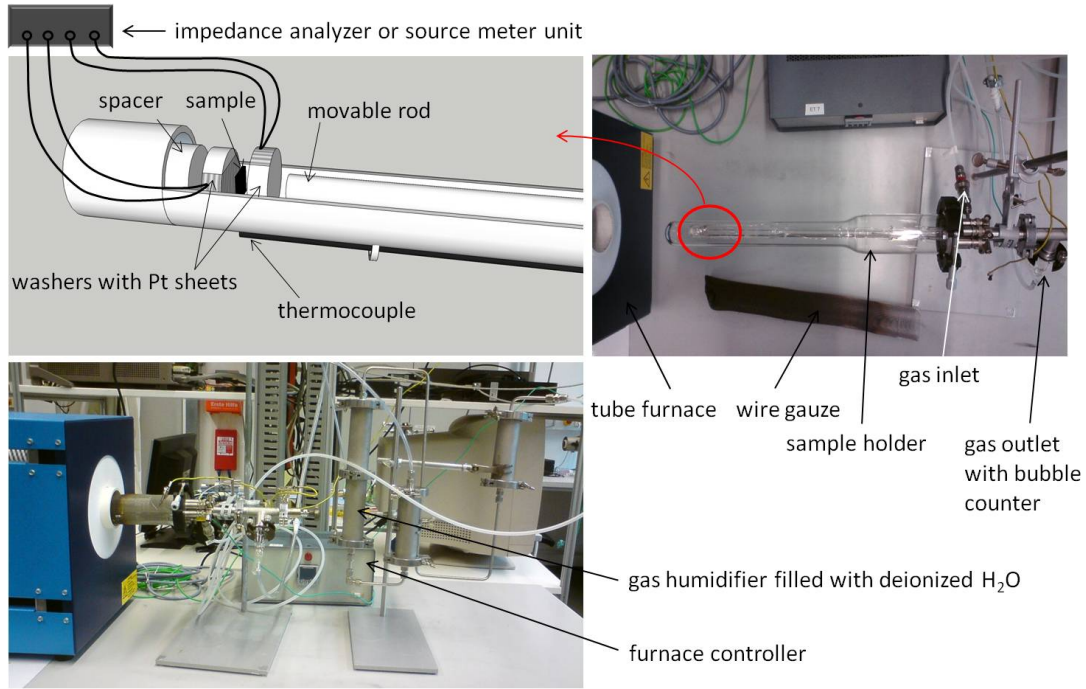
Figure 3.3: Macroscopic sample holder. Top left: Sketch of the place where the sample is inserted. Top right: Photograph (top view) of the entire sample holder. Bottom left: Photograph of the sample holder in the tube furnace. Cables are not shown in this figure.

Table 3.5: Parameters for AC measurements on LSF64-YSZ-LSF64 samples.

parameter	value
f_{start}/Hz	1×10^6
f_{stop}/Hz	1 to 1×10^{-2}
voltage rms/V	0,01
number of data points per decade	5 or 10
gas flow of reducing gas mixture/bubbles per second	a few
temperature	$\approx 650°C$

3.2 Symmetric cells with porous paste LSCF6428 electrodes

3.2.1 Sample preparation

Polycrystalline YSZ disks of ≈ 2 mm thickness and ≈ 1 cm diameter were obtained by isostatic pressing of 8 mol% yttria doped zirconia powder (Tosoh, Japan), and subsequent sintering for 5 hours at 1550 °C (see [80, p 10] and [81, p 11]). Table 3.6 gives an overview of the prepared samples, their purpose (for more detailed description see below) and the annealing conditions.
The LSCF6428-YSZ-LSCF6428 cells were prepared according to the method from [81, pp 11-13] using LSCF6428 powder synthesized via a Pechini synthesis and subsequent annealing for three hours at 900°C.

Table 3.6: The LSCF6428-YSZ-LSCF6428 samples.

sample name	purpose	annealing conditions
YSZ_poly_15_LSCF	"anode quality test sample" for sample SOEC-001	heating with 10°C/min to 850°C (5 h), cooling with 10°C/min
YSZ_poly_16_LSCF	"anode quality test sample" for SOEC-003 - SOEC-005	see above
YSZ_poly_12_LSCF	air vs. N_2	see above
YSZ_poly_9_LSCF, YSZ_poly_10_LSCF, YSZ_poly_11_LSCF	multiple layers	heating with 2°C/min to 850°C (2 h), cooling with 12°C/min

YSZ_poly_15_LSCF and YSZ_poly_16_LSCF These samples were prepared with the same electrode slurry as the SOEC samples indicated in table 3.6 ("anode quality test samples"). The YSZ disks were first roughened on both sides with SiC abrasive paper (Struers FEPA P 500) and cleaned in ethanol p.a. A mixture of 97 wt% percent LSCF6428 powder and 3 wt% ethyl cellulose was ground in a mortar until the powder was homogeneous and a slight greyish shimmering was visible (grinding for 10-15 min was normal). Terpineol obtained from Aldrich was then added (57 % of the powder's total mass) and the electrode slurry was applied to one side of the YSZ disks using a paint brush (flat, size 6). The samples were dried in the drying oven at 85°C until the solvent had evaporated (electrode surface looked matt). Afterwards, the second electrode was applied by the same procedure. The cell was then annealed in air at 850°C (annealing conditions see table 3.6).

YSZ_poly_12_LSCF This sample was prepared as described in the paragraph above and was used to compare the resistance of LSCF in air and pure nitrogen.

YSZ_poly_9_LSCF, YSZ_poly_10_LSCF, YSZ_poly_11_LSCF These samples were prepared to evaluate the effect of multiple layers of LSCF6428 on the electrode impedance. The preparation procedure was identical to the one described above except that the LSCF and ethyl cellulose powders were first mixed with terpineol and then grinding was started. After having dried the electrode in the drying oven the electrode slurry application and drying step was repeated once (YSZ_poly_10_LSCF) or twice (YSZ_poly_11_LSCF) for each side. During the application of the second or third layers the electrodes applied and dried previously on the opposite side of the electrolyte disk showed poor mechanical stability (broke off very easily) and so YSZ_poly_10_LSCF could not be coated successfully with 2 layers of electrode slurry on both sides and therefore measurements on this sample were not performed. YSZ_poly_11_LSCF was coated with 2 layers of electrode slurry on both sides (instead of 3, as planned). This is attributed to the grinding of LSCF and ethyl cellulose together with terpineol because the electrodes of the samples described in the paragraph above were much more robust. However, the comparison between a sample with one and two layers of LSCF on each side can still be done.

3.2.2 Measurement setup

The AC measurements on the symmetric LSCF6428-YSZ-LSCF6428 cells were performed in 4-wire mode and with the setup also used for the LSF64-YSZ-LSF64 samples. Experiments in a gas mixture of 1% O_2 in N_2 and in air were done using a Solartron SI 1260 Impedance/Gain-Phase Analyzer or a Novocontrol Alpha-A High-Performance Frequenzy Analyzer, respectively. The measurement parameters are given in table 3.7, 3.8, 3.9 and 3.10.

Table 3.7: Parameters for AC measurements on sample YSZ_poly_16_LSCF measured in 1% O_2.

parameter	value
f_{start}/Hz	1×10^6
f_{stop}/Hz	5×10^{-2}
voltage rms/V	0,01
number of data points per decade	10
gas flow of 1% O_2 in N_2 gas mixture/bubbles per second	a few
temperature	$\approx 649°C$

Table 3.8: Parameters for AC measurements on sample YSZ_poly_16_LSCF measured in air.

parameter	value
f_{start}/Hz	1×10^6
f_{stop}/Hz	1×10^{-2}
voltage rms/V	0,03
number of data points per decade	5
gas flow of air	sample holder open
temperature	$\approx 648°C$

Table 3.9: Parameters for AC measurements on samples YSZ_poly_9_LSCF and YSZ_poly_11_LSCF (Solartron 1260; for temperature see subsection 5.4.2).

parameter	value
f_{start}/Hz	1×10^6
f_{stop}/Hz	1×10^{-2}
voltage rms/V	0,01
number of data points per decade	10
gas flow of air	sample holder open

Table 3.10: Parameters for AC measurements on sample YSZ_poly_12_LSCF measured in N_2 or air.

parameter	value
f_{start}/Hz	1×10^6
f_{stop}/Hz	5×10^{-2} (air) 1×10^{-3} (N_2)
voltage rms/V	0,01
number of data points per decade	5
gas flow of N_2 or air	a few bubbles per second (N_2); sample holder open (air)
temperature	$\approx 649°C$

3.3 Model-type LSF64-YSZ-LSCF6428 SOECs

3.3.1 Sample preparation

The preparation procedure for these samples is depicted in figure 3.4. Polycrystalline YSZ disks (preparation see section 3.2.1) were ground and polished (Struers TegraPol-31). An LSF64 layer was then deposited by PLD (parameters see table 3.11), microstructured by standard photolithography and ion etching (see figure 3.5) to give a circle with a diameter of 5 mm (see figure 3.4 bottom right).

On top of the LSF64 electrode a Pt layer (using Ti to promote adhesion) was deposited and microstructured by lift-off photolithography into a circular grid, which is shown in detail in figure 3.6. The photolithographic process (except for the mask) is the same as for the LSF64-YSZ-LSF64 samples (figure 3.2).
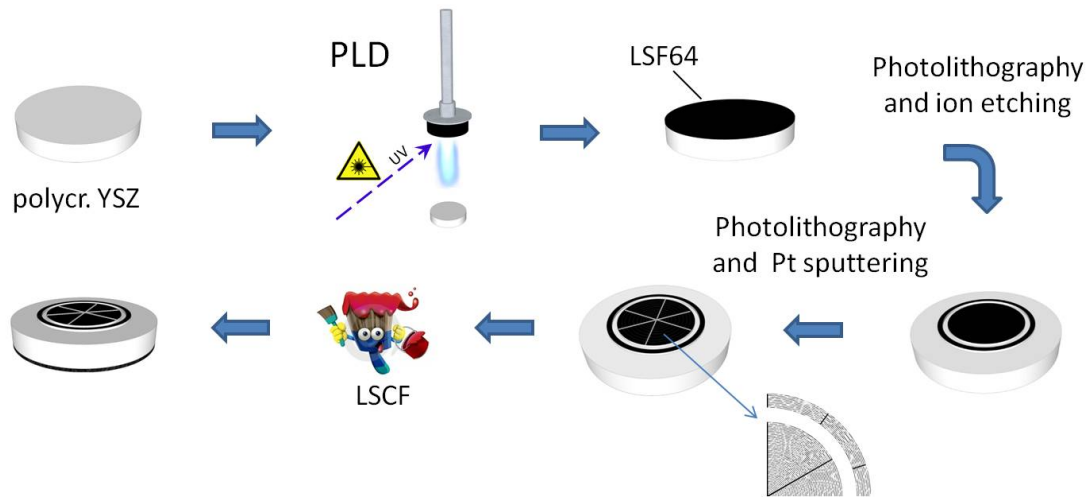

Figure 3.4: Preparation process for model-type SOECs (picture of brush from [82]).

Table 3.11: Parameters for PLD, SOECs.

parameter	sample				
	SOEC-001	SOEC-002	SOEC-003	SOEC-004	SOEC-005
desired film thickness/nm	200	200	250	250	250
set temperature/°C	780	770	1230	1230	1230
sample temperature/°C	604	608	640	610	625
oxygen partial pressure/mbar	4×10^{-2}	4×10^{-2}	4×10^{-2}	4×10^{-2}	4×10^{-2}
pulse rate/Hz	5	5	5	5	5
energy per pulse/mJ	400	400	400	400	400
deposition time/min	40	40	30	30	30
distance target-furnace/cm	5,5	5,5	6	6	6
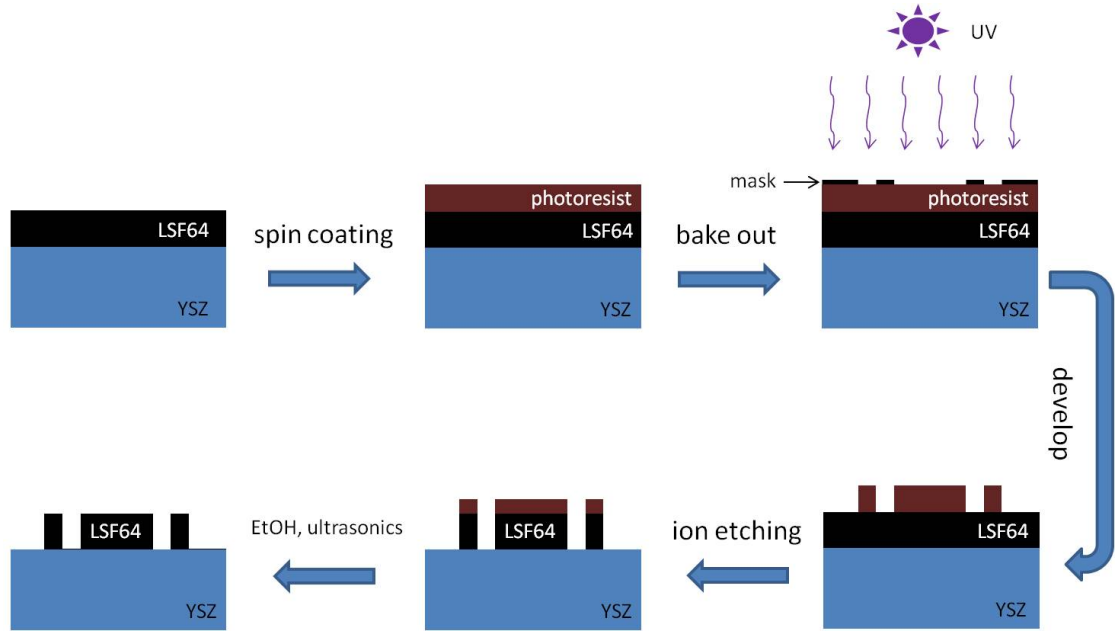
Figure 3.5: A scheme for the microstructuring process of the LSF64 layer on the model-type SOEC samples including photolithography and ion etching.

Exception: SOEC-001 The sample preparation for SOEC-001, the first sample produced, was slightly different than for the other SOEC samples because of new insights that were gained during the first measurements. The microstructuring of the LSF64 electrode, that was not included in the preparation process at first, turned out to be necessary and was therefore carried out after the Pt deposition. The impact of the microstructuring of the LSF64 electrode on the measurements will be discussed in detail in chapter 5.

The SOEC sample holder, that will be described in the following subsection, features two separate gas chambers for the two electrodes. In order to improve the gas-tightness of the connection between sample and the alumina tube confining the inner chamber,
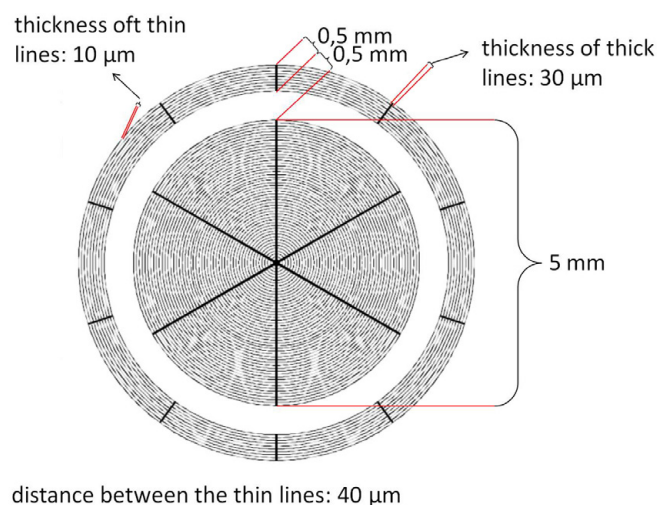
Figure 3.6: The photolithographic mask for the microstructuring of the Pt layer on the LSF64 electrodes for the SOEC samples. The metal pattern on the sample corresponds to the areas shaded by the mask (black and grey lines and circles).

the YSZ disks for SOEC-003 - SOEC-005 were ground and polished as described above. This issue will also be treated in more detail in chapter 5.

3.3.2 Measurement setup

The measurement setup is sketched in figure 3.7. The sample holder "ProboStat" (NorECS, Norway) features two separate gas chambers for anode and cathode. Gas flow 1 (usually $\approx$ 15 ml/min) was controlled with an Aera FC7700C mass flow controller, bubbled through a humidifier (containing deionized water at room temperature) and fed into the cathode gas chamber (inner chamber). The outcoming gas stream was analyzed with a Pfeiffer OmniStar Gas Analysis System GSD320 containing a QMG220 PrismaPlus Compact Mass Spectrometer (EI-Q-MS; quartz sample inlet capillary). The operator can choose between two detectors: a Faraday cup and a SEM.

The anode gas chamber (outer chamber) was supplied with gas 2 (normally $\approx$ 20 ml/min), regulated with an Aera FC770AC mass flow controller. For electrochemical measurements the sample was heated to around 650°C. Figure 3.8 shows how the sample is mounted in the sample holder.

DC measurements were done with a Keithley 2611A source meter unit (4-point measurement), AC measurements were performed with a Novocontrol Alpha-A High Performance Frequency Analyzer with Electrochemical Test Station POT/GAL (4-point measurement).

The measurement parameters (samples SOEC-004 and SOEC-005) are summarized in table 3.12.
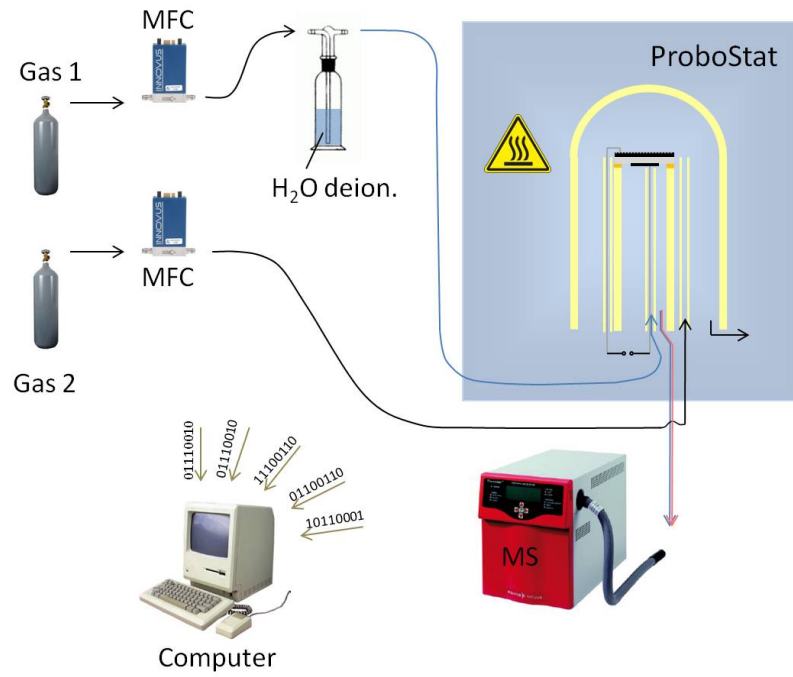
Figure 3.7: Measurement setup for SOEC samples (picture of computer from [83], picture of MS from [84]).

Table 3.12: Parameters for DC measurements on samples SOEC-004 and SOEC-005.

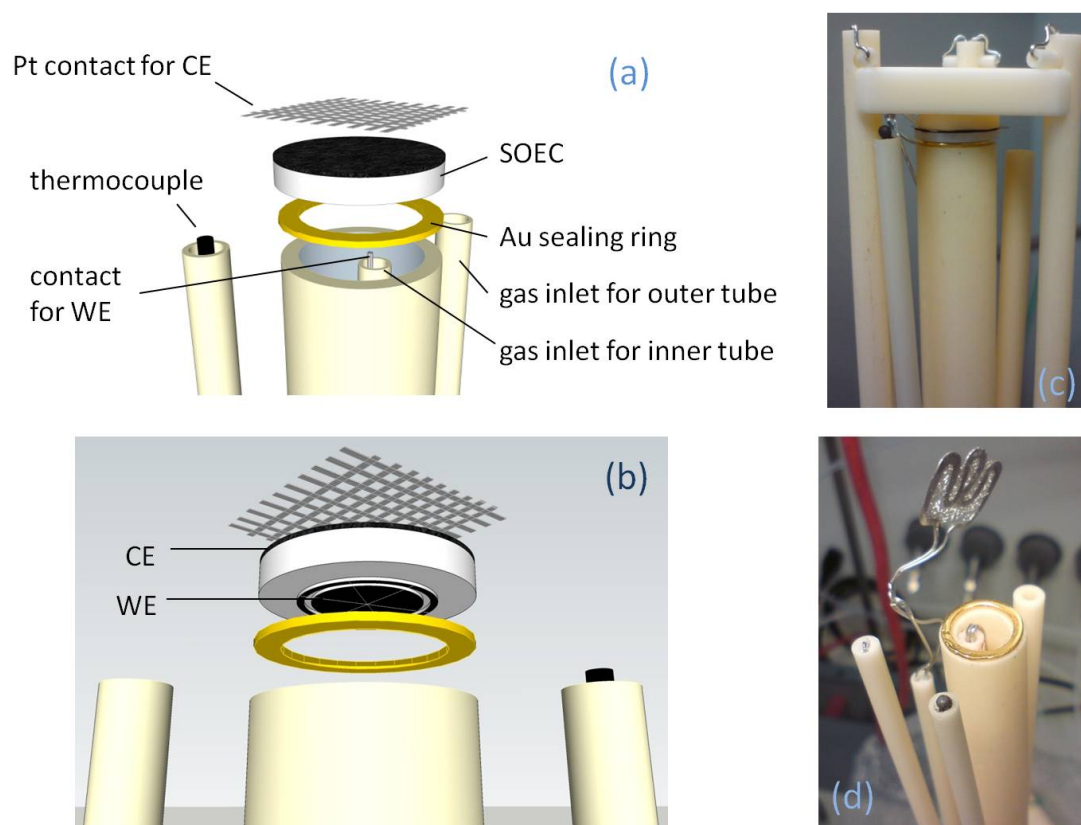| parameter	SOEC-004	SOEC-005
measurement mode	potentiostatic	
$\Delta E_{\text{cell, start}}$	+ 200 mV	
$\Delta E_{\text{cell, stop}}$	- 2 V	
number of data points	20	
acquisition time/s	600	
acquisition time resolution/s	0,5	
temperature/°C	639	648
high C-mode	yes	
4-wire mode	yes	
inner gas chamber	2,6% H_2O and 97,4% Ar	
gas flow inner chamber/scm^3/min	15,9	
outer gas chamber	1% O_2 in N_2	
gas flow outer chamber/scm^3/min	21,1	21

Figure 3.8: Sketch of the SOEC sample mounted in the sample holder (CE = counter electrode, WE = working electrode), (a) top and (b) bottom view. (c) The SOEC is held in place by the alumina plate and the outer rods that are tied down by metal springs, fixed at the bottom of the sample holder (not visible). (d) Sample holder without sample. The inner tube is used for gas supply and to hold the inner contacting wire in place. Parts in the heated zone are made from alumina, Pt or Au.

4 Results of sample characterisation

4.1 LSF64 PLD target

The diffraction patterns measured in this work were recorded on a Philips X'Pert diffractometer with X'Celerator detector and the Cu X-ray tube operated at 40 kV and 40 mA, using a Ni filter to obtain the Cu-Kα radiation.

The X-ray diffraction (XRD) pattern of the target for PLD, confirming the successful synthesis of LSF64, is shown in figure 4.1.
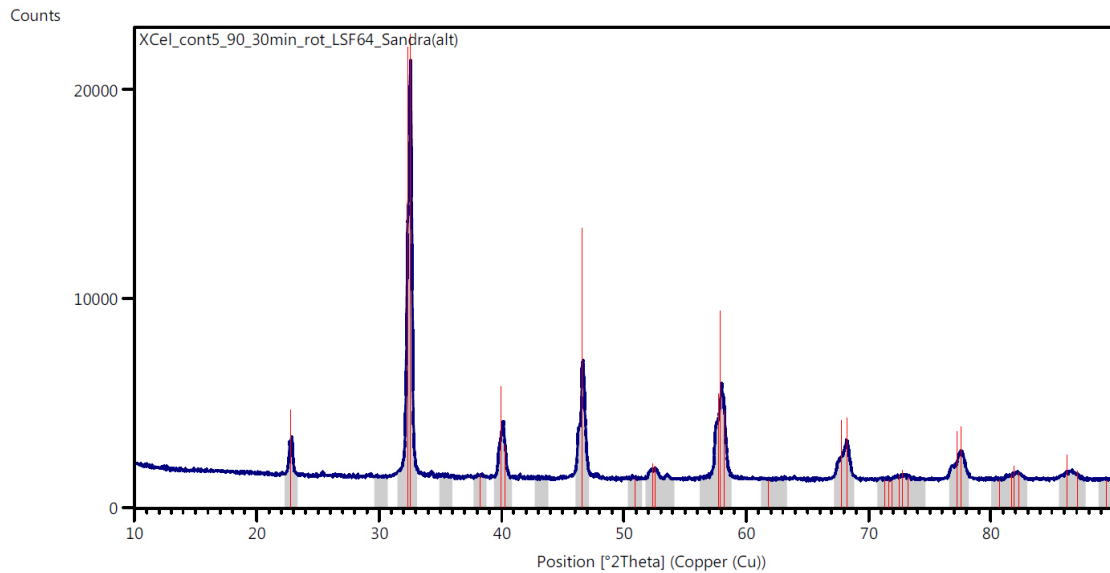

Figure 4.1: XRD pattern of the LSF64 target for PLD. The measured peaks (blue) correspond very well to the red lines that represent the LSF64 pattern from the ICDD database [85] (pdf 01-082-1961).

4.2 LSF64-YSZ-LSF64 cells

Figure 4.2 shows optical microscope images of different LSF64-YSZ-LSF64 samples. Due to the problems during Ti/Pt sputter deposition (see subsection 3.1.1), the metal grid on some electrodes was damaged during lift-off (see figure 4.2 (a) and (b), left pictures). Not the whole area of the 0,5 × 0,5 mm YSZ crystal can be covered by the grid due to the properties of the photoresist. After spincoating, the photoresist is much thicker along the edges of the sample and thus cannot be hardened by the UV light and so no metal is deposited in this area.

Additionally, the non-covered area varies from electrode to electrode, which could be due to the varying viscosity of the photoresist.
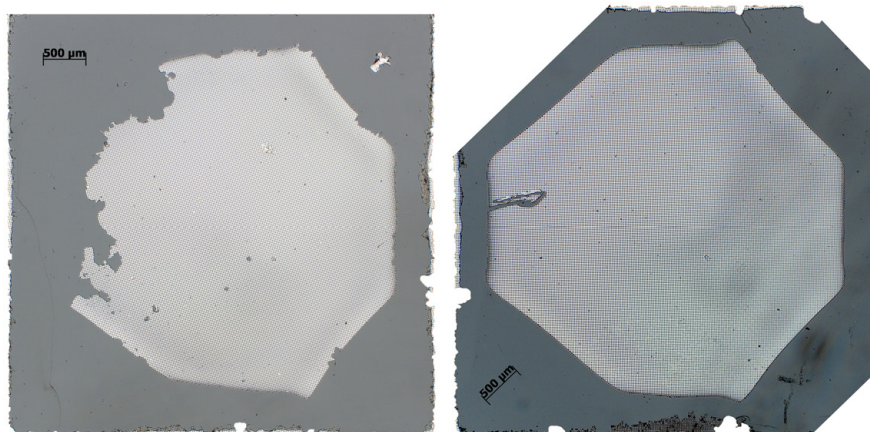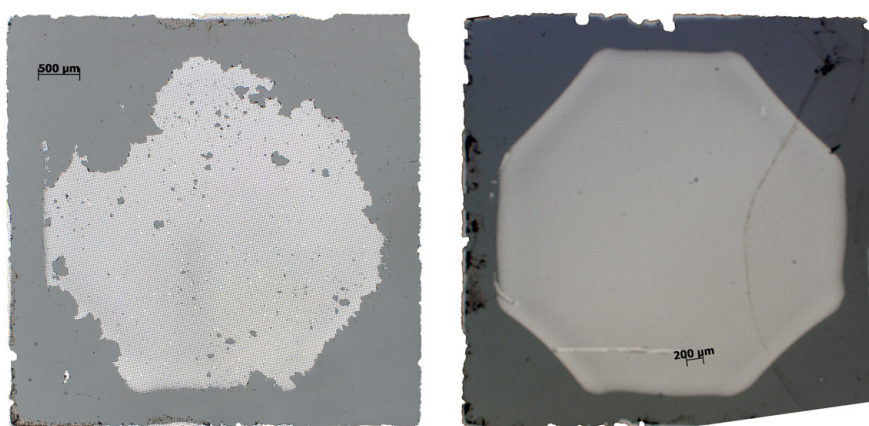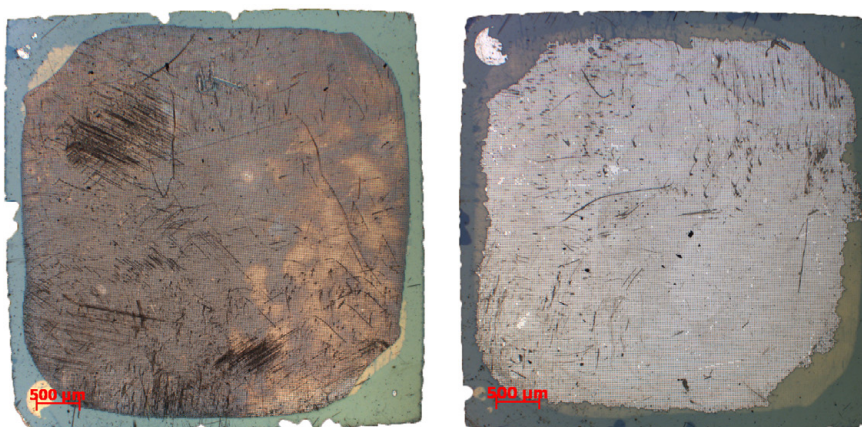
Figure 4.2: Optical microscope bright field images of LSF64 electrodes with metal grid. (a): Electrodes on sample LSF64_002_3 with damaged (left) and intact grid (right). (b) Damaged (left) and intact (right) grids on electrodes of sample LSF64_002_2. (c) Both grids on sample LSF64_001_1 are intact. The area which is not covered by an undamaged grid varies, probably due to changing viscosity of the photoresist.
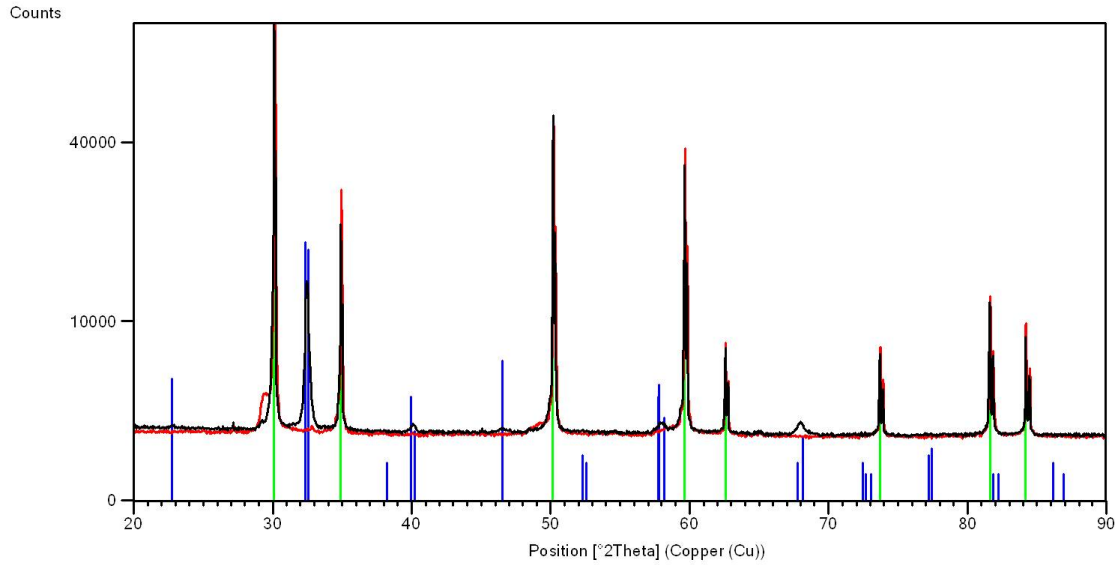
Figure 4.3: XRD patterns. LSF64-YSZ sample (black line), polycrystalline YSZ disk without coating (red line) and ICDD database [85] patterns for YSZ (pdf 01-070-4436, green lines) and LSF64 (pdf 00-049-0285 blue lines).

4.3 SOEC samples

4.3.1 XRD pattern of LSF64 on polycrystalline YSZ

Figure 4.3 shows four different XRD patterns: One for a polycrystalline YSZ disk coated with an LSF64 thin film (black line), one for a polycrystalline YSZ disk without any coating (red line) and two patterns from the ICDD database [85] (pdf 01-070-4436 for YSZ (green lines) and pdf 00-049-0285 for LSF64 (blue lines)). The PLD parameters for the deposition of the LSF64 thin film were similar to the ones for the SOEC samples.
By comparing the result of the measurement of the LSF64-YSZ sample with the pattern measured for a YSZ disk without any coating, the peaks originating from YSZ can be found. The YSZ pattern from the database confirms that the red peaks are caused by diffraction on YSZ. The remaining peaks in the LSF64-YSZ pattern are in good agreement with the ICDD pattern for LSF64, confirming the successful deposition of the LSF64 thin film on polycrystalline YSZ.

4.3.2 SEM images

Figure 4.4 shows scanning electron microscope (SEM; FEI Quanta 200, The Netherlands) images of the polycrystalline YSZ disk coated with an LSF64 thin film that was examined by XRD (see above). Pores in the polycrystalline YSZ are visible (fig. 4.4 (a), (b) and (c)). The pores are closed (fig. 4.4 (c)) and so the YSZ disk can be expected to be gas tight. The polishing step caused scratches in the YSZ surface which are discernible under the LSF64 thin film (fig. 4.4 (b), (c) and (d)). The grains of the dense LSF64 layer can be seen in fig. 4.4 (d).
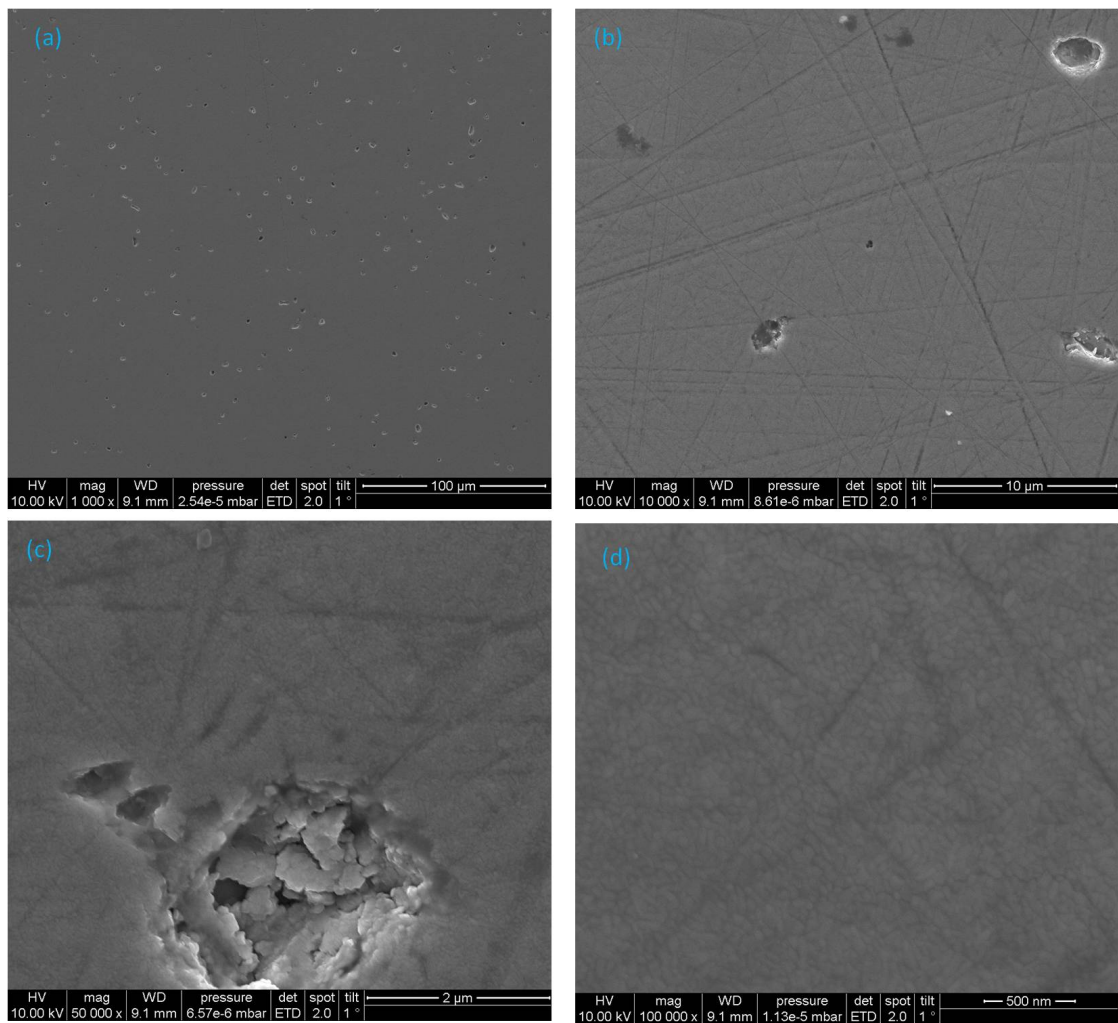
Figure 4.4: SEM images of a polycrystalline YSZ disk coated with an LSF64 thin film.

4.3.3 Optical microscope images

Figure 4.5 (a) shows a photograph (recorded without microscope) of the LSF64 electrode on a model SOEC. Sometimes, the photoresist cannot be removed completely after ion etching (brown lines at the edges of the cell). Figure 4.5 (b) is a bright field image of the LSF64 cathode. The metal grid is clearly visible on the lighter areas (LSF64), proving that the ion etching and photolithography steps worked. In dark field mode (figure 4.5 (c), (d)), the contrast between YSZ (white) and LSF64 (black) is much better.
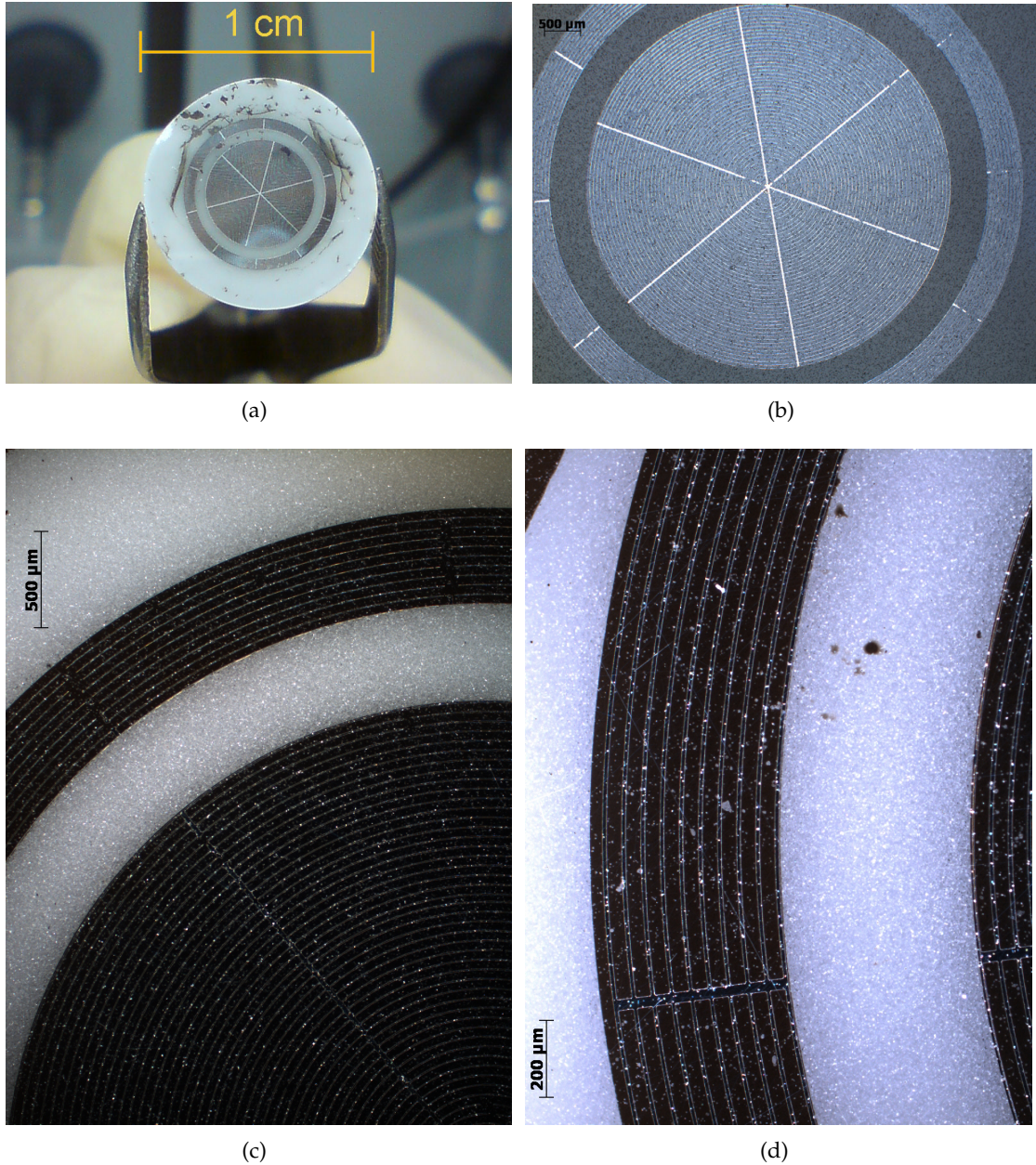

(a)   (b)

(c)   (d)

Figure 4.5: Images of model SOECs ((b) - (d) taken in an optical microscope).

5 Results and discussion of electrochemical measurements

This section starts with the results of the calibrations of mass flow controllers (MFCs) and mass spectrometer. Then the measurements performed on the three different kinds of samples are described. The results of the investigations are given and the influence of settings concerning the setup on the outcome of the measurements will be emphasized.

5.1 Calibration of mass flow controllers

For three mass flow controllers (Tylan FC280S, Aera FC-7700C, Aera FC-770AC) a calibration had to be done for two reasons: First, two of the MFCs were not used with gases they were once gauged for, so a calibration curve was needed to convert the displayed gas flows into gas flows of the actual gas used. Second, the three MFCs in question were obtained second-hand and therefore it cannot be assumed that they are still gauged correctly. An Aera Transformer FC-PAR780C mass flow controller, which can be programmed to control the flow of different kinds of gases via the software "Aera MFSet", was used as a reference.

Calibration curves were recorded by connecting the MFCs in series, setting a gas flow with the first one and recording the flow measured with the second one. Since the values measured with the second MFC varied, the highest and the lowest value were noted and the mean value was calculated.
The Tylan FC280S was calibrated for H_2 2,5% in Ar using the Aera Transformer FC-PAR780C set to H_2 2% in Ar being the closest option available and the error being neglected. Similarly, the Area FC-770AC was calibrated for O_2 1% in N_2 using the Aera Transformer FC-PAR780C set to O_2 3% in N_2. For the Ar calibrations of the Aera FC-770AC and the Aera FC-7700C the Aera Transformer FC-PAR780C was set to Ar. Calibration curves were recorded with the following flow schemes:

- Tylan FC280S (H_2 2,5% in Ar), Aera FC-7700C (Ar)
    - calibration 1: Aera Transformer FC-PAR780C $\rightarrow$ MFC to be calibrated
    - calibration 2: MFC to be calibrated $\rightarrow$ Aera Transformer FC-PAR780C
    - calibration 3: Aera Transformer FC-PAR780C $\rightarrow$ MFC to be calibrated

- Aera FC-770AC (O_2 1% in N_2 or Ar)
    - calibration 1: Aera FC-770AC $\rightarrow$ Aera Transformer FC-PAR780C
    - calibration 2: Aera Transformer FC-PAR780C $\rightarrow$ Aera FC-770AC
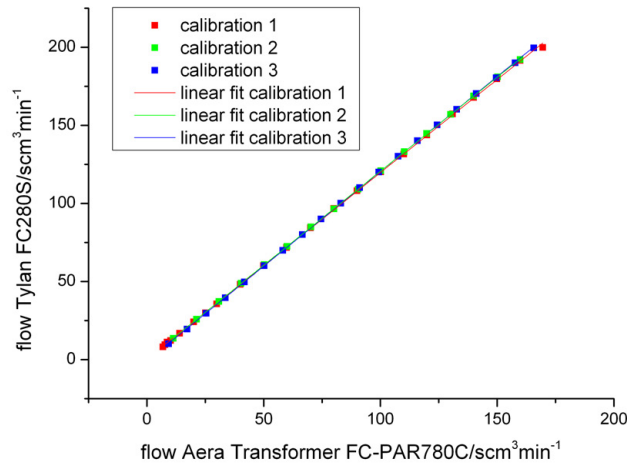   - calibration 3: Aera FC-770AC $\rightarrow$ Aera Transformer FC-PAR780C

Figure 5.1: Calibration curves for MFC Tylan FC280S (H_2 2,5% in Ar).
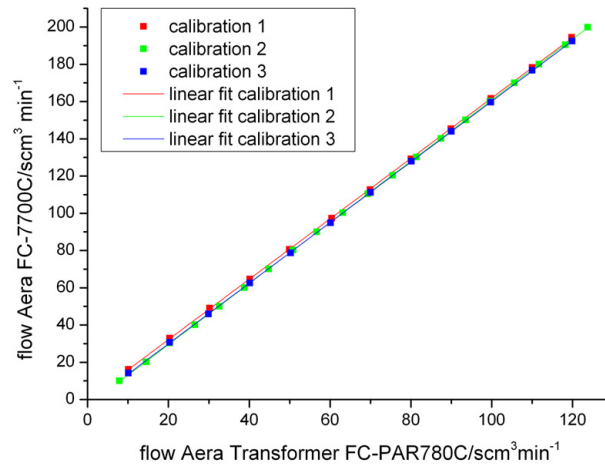

Figure 5.2: Calibration curves for MFC Aera FC-7700C (Ar).

Figures 5.1, 5.2, 5.3 and 5.4 show the calibration curves. Slope and intercept on the y-axis a given in table 5.1.

The calibration curves for all three MFCs are linear and reproducible. It is however remarkable that even though the Aera FC-7700C should be gauged to Ar there is a strong deviation from the gas flow values measured by the Aera Transformer FC-PAR780C.

The calibration curves that were finally used to correct the values read from the Tylan FC280S, Aera FC-7700C and Aera FC-770AC contain the mean values of each of the three calibrations.
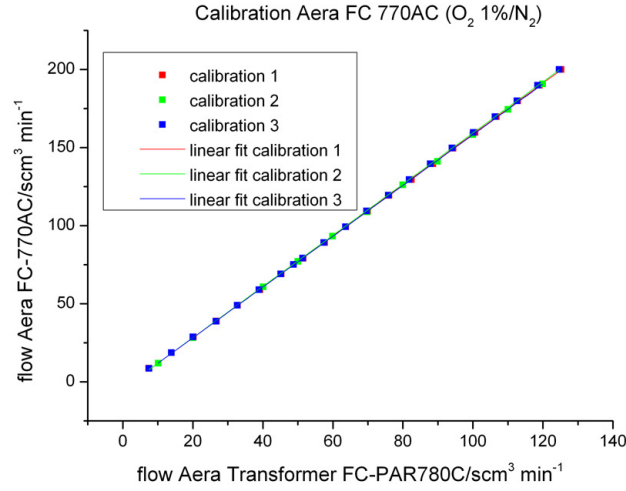
Figure 5.3: Calibration curves for MFC Aera FC-770AC (O_2 1% in N_2).
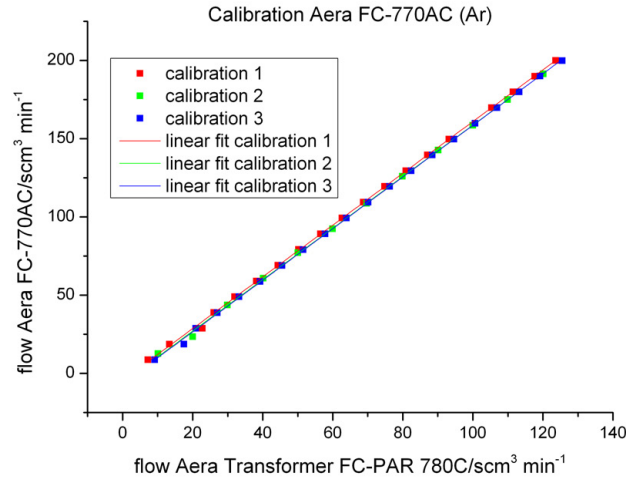

Figure 5.4: Calibration curves for MFC Aera FC-770AC (Ar).

5.2 Calibration of the mass spectrometer

In order to quantify the gases leaving the SOEC sample holder, the mass spectrometer (Pfeiffer OmniStar Gas Analysis System GSD320 with QMG220 PrismaPlus Compact Mass Spectrometer) needed to be calibrated for H_2 and O_2.

5.2.1 Gas flows and concentrations

Generally, when recording a calibration curve, the standard substances may be subject to dilution (e.g. due to the sample preparation or the measurement setup). During the measurements, the analyte may also be diluted. The dilution factors (dilution occurs if the dilution factor is < 1) for calibration and measurement, f_{cal} and f_{meas}, respectively,

Table 5.1: Slope and y-intercept of the MFC calibration curves.

	parameter	Tylan FC280S	FC-7700C	Aera FC-770AC (1% O_2/N_2)	Aera FC-770AC (Ar)
calibration 1	slope	1,1927	1,6215	1,6210	1,6540
	y-intercept	0,52684	-0,2360	-4,3395	-4,3958
calibration 2	slope	1,2139	1,6403	1,6252	1,6456
	y-intercept	-0,8062	-3,2620	-4,3219	-5,8604
calibration 3	slope	1,2043	1,627	1,6380	1,6410
	y-intercept	0,2822	-2,5933	-4,4571	-6,4467
mean value	slope	1,2036	1,6296	1,6309	1,6410
	y-intercept	0,0009	-2,0304	-4,3728	-5,5676

can be different. In order to determine the amount of substance present in the sample - which is one of the aims of this study - both dilution factors have to be known.

For the calibration of the mass spectrometer, gas flows with known compositions were produced by adjusting the flow values of a gas containing the analyte and an inert gas by means of MFCs and mixing the two gas streams. After mixing, a dilution of the analyte can occur (e.g. due to moistening of the gas stream in a humidifier). During a measurement, dilution of the analyte can occur as well (e.g. the concentration of produced H_2 depends on the incoming gas flow[1]; also, electrochemical processes can change the amount of gas in one of the gas chambers of the SOEC sample holder).

The linear calibration function relates the signal S to the concentration of analyte in the known gas flow before it enters any apparatus. If dilution occurs during calibration or measurement, it needs to be taken into account by multiplying the concentrations during calibration and measurement, c_{cal} and c_{meas} with the respective dilution factors, f_{cal} and f_{meas}. A measurement that leads to the same MS signal S as a certain calibration mixture is generated by concentrations $c_{cal} \cdot f_{cal}$ and also by $c_{meas} \cdot f_{meas}$ (with k and d denoting sensitivity and blank value):

$$S = k \cdot c_{cal} f_{cal} + d = k \cdot c_{meas} f_{meas} + d \quad \Rightarrow \quad \boxed{c_{meas} = c_{cal} \cdot \frac{f_{cal}}{f_{meas}} = c_{cal} \cdot f} \qquad (5.1)$$

In order to obtain the correct concentration in a measurement, the concentration computed from the calibration curve has to be multiplied by the overall dilution factor f, which is f_{cal}/f_{meas}. This concentration can then be attributed to the known gas flow before it enters the apparatus and therefore, the mole number of analyte can be calculated. In the following two subsections different cases of calibration and measurement will be discussed with the aim of finding f (if possible) or estimating the error if it is simply neglected.

---

[1]This is also important because by increasing the incoming gas flow, a certain amount of analyte can be pushed from just above the limit of detection (LOD) to below the LOD of the MS.
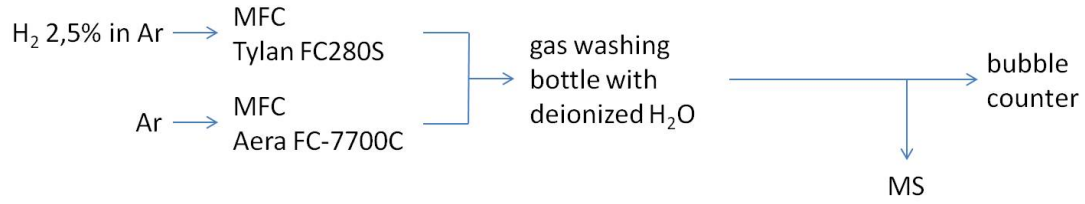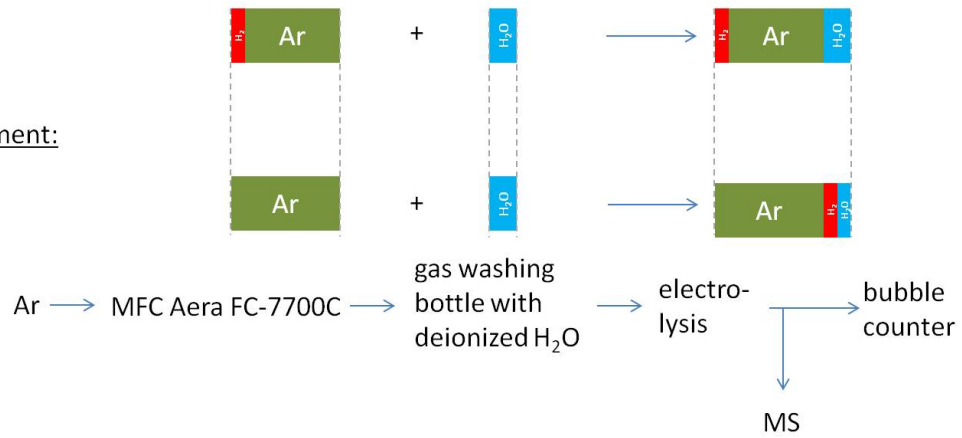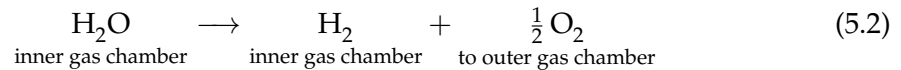
Figure 5.5: Flow scheme for H_2 calibration of the MS (top) compared with the flow scheme for the inner gas chamber of the SOEC sample holder during a measurement (bottom). The colored boxes represent gas flows. As can be seen from the grey lines, the total gas flow is increased by the same factor in both situations and it follows that $f = 1$.

Calibration for H_2 (inner gas chamber)

Figure 5.5 shows the gas flow schemes for calibration and measurement in this case and illustrates the changes in gas composition and flow throughout the two processes.

For the H_2 calibration known flows of 2,5% H_2 in Ar and pure Ar (99,999%) were mixed, bubbled through a gas washing bottle and then fed into the MS. By bubbling through the gas washing bottle the gas volume is increased by a factor f_{cal}.

During the measurement a known gas flow of Ar is bubbled through the gas washing bottle and introduced into the inner chamber of the sample holder, where a certain amount of water is converted to hydrogen. However, assuming perfect gases, the total gas flow in the inner chamber does not change, as can be seen from the reaction equation (and from the colored boxes in fig. 5.5):

$$\underset{\text{inner gas chamber}}{H_2O} \quad \longrightarrow \quad \underset{\text{inner gas chamber}}{H_2} \quad + \quad \underset{\text{to outer gas chamber}}{\tfrac{1}{2}O_2} \tag{5.2}$$

Oxygen is transported through the cell and released into the outer gas chamber. In both the calibration and the measurement situation the total gas flow that comes out of the sample holder's inner gas chamber is the same, provided the initial total gas flow is the same. The dilution factor is the same for calibration and measurement,

$$f_{cal} = f_{meas} \tag{5.3}$$

and the overall dilution factor $f = 1$. The measured concentrations can be calculated from the calibration curve without correction and can be attributed to the initial gas

stream. Even though in a measurement the inital gas stream consists of pure Ar, the MS signal can be interpreted as if the inital Ar stream already contained the produced hydrogen. Therefore, the mole number of produced H_2 can be calculated from the measured concentration and the initial Ar flow.

Calibration for O_2

Quantification of O_2 in the outer gas chamber   The amount of oxygen in the outer gas chamber was not quantified in this work. With the aim of developing a setup for SOEC measurements this case is discussed in theory because measuring the amount of O_2 produced during electrolysis is very helpful to show that the SOEC actually works. The dilution factor for calibration, which in this case would be done without moistening (see figure 5.6) is 1.
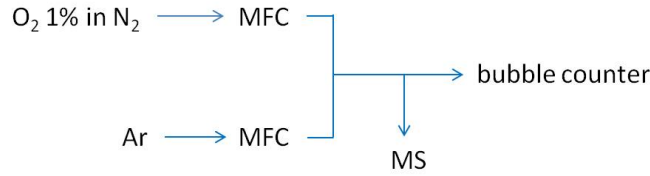

Figure 5.6: Flow scheme for the O_2 calibration in the outer gas chamber.

In a measurement, however, the gas flow in the outer gas chamber will increase ($\rightarrow$ dilution factor $f_{meas} < 1$) because the oxygen incorporated at the cathode will migrate through the cell, is released at the anode and thus contributes to the gas flow in the outer gas chamber of the SOEC sample holder (see figure 3.7, page 41), so

$$f_{cal} \neq f_{meas} \tag{5.4}$$

Moreover, f_{meas} depends on the current through the cell. It could be determined by measuring the gas flow at the outlet of the sample holder's outer gas chamber. However, this is not possible using an MFC because the concentration of O_2 changes with current (i.e. almost permanently) and the MFC would need constant recalibration, for which the gas composition must be known.
There are, however, several possible ways to determine f_{meas} approximately.

- The change in gas flow can simply be neglected ($f_{meas} \approx 1$). For the present setup the error can roughly be estimated as follows:

  Knowing that a charge Q of $4F$ electrons is needed for the production of one mole O_2 (n is the mole number), the O_2 volume produced per unit time (V/t) can be calculated:

  $$n(O_2) = \frac{Q}{4F} = \frac{It}{4F} \qquad \text{and} \qquad pV = nRT = \frac{It}{4F}RT$$

  $$\Rightarrow \boxed{\frac{V}{t} = \frac{IRT}{4F \cdot p}} \tag{5.5}$$

  Assuming that a realistic current I through the cell is about 10 mA (see subsection 5.2.2, paragraph "limit of detection") the additional gas flow in the outer gas

chamber can be estimated to be roughly 0,05 scm^3/min at 23°C and atmospheric pressure (perfect gas approximation). This change is even smaller than the (minimum) measurement accuracy of the MFC that was used to control the Ar flow (Aera FC-770AC) , which is $\pm$ 1 scm^3/min [86, p 6.2], so the gas flow in the outer gas chamber can safely assumed to be unchanged by the produced oxygen.

This was the approach chosen in this work. Since reflecting about other options was part of the goals of this study, the following two points are mentioned, even though they were not tested in practice.

- If a more accurate approximation is needed (e.g for higher currents, lower gas flows and if a more accurate MFC is used) the increase in volume in the outer gas chamber due to oxygen production can be calculated from the electric current.

- The gas flow coming from the outer gas chamber could be measured by means of an MFC being calibrated to a gas composition that is in the middle of the range of expected gas compositions. The assumption that the changing gas composition does not change the properties of the gas mixture significantly is supported by the fact that in the Aera gas database for the programmable Aera Transformer FC-PAR780C the parameters for pure N_2 and 3% O_2 in N_2 are identical.

Quantification of O_2 in the inner gas chamber (from leakage)   It turned out that due to a leak between inner and outer chamber of the SOEC sample holder O_2 was present in the inner gas chamber if a gas containing O_2 was used in the outer gas chamber. The leakage issue is discussed in more detail in subsection 5.5.1.

When electrolysing water, a quantification of O_2 in the inner chamber is important because the current needed for pumping O_2 to the other side of the cell can then be calculated from the amount of O_2 consumed electrochemically and subtracted from the total current, giving the current that was used for the production of H_2 (which should be in agreement with the amount of H_2 measured).

The flow scheme used for this calibration is shown in figure 5.7. It was chosen to bub-

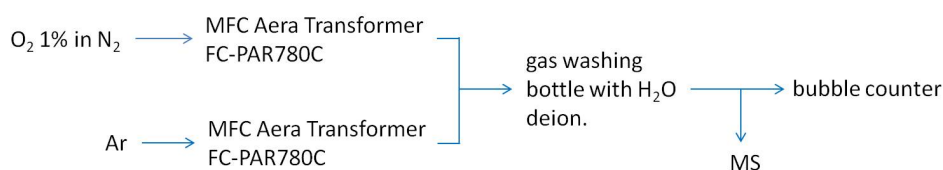*Figure 5.7:* Flow scheme for the O_2 calibration in the inner gas chamber.

ble O_2 through the gas washing bottle in order to make f_{cal} as similar as possible to f_{meas}. However, the quantification of O_2 in the inner chamber remains an approximation due to the exchange of gases between the two gas chambers and this error cannot be estimated.

5.2.2 Tasks for the quantification of gases by means of MS

The questions to be answered and the expected answers are discussed below.

Mass interference

Which mass signals can be used for the quantification of H_2 and O_2 in the presence of H_2O?
According to the mass spectrum of H_2 in figure 5.8 (a) a calibration via the $m/z = 2$ signal should be possible. Mass interference with water should not occur (see figure 5.8 (b)). For O_2 a calibration using the $m/z = 16$ signal as well as the $m/z = 32$ signal is expected to be possible (see fig. 5.9), with the $m/z = 32$ being expected to give a higher sensitivity.
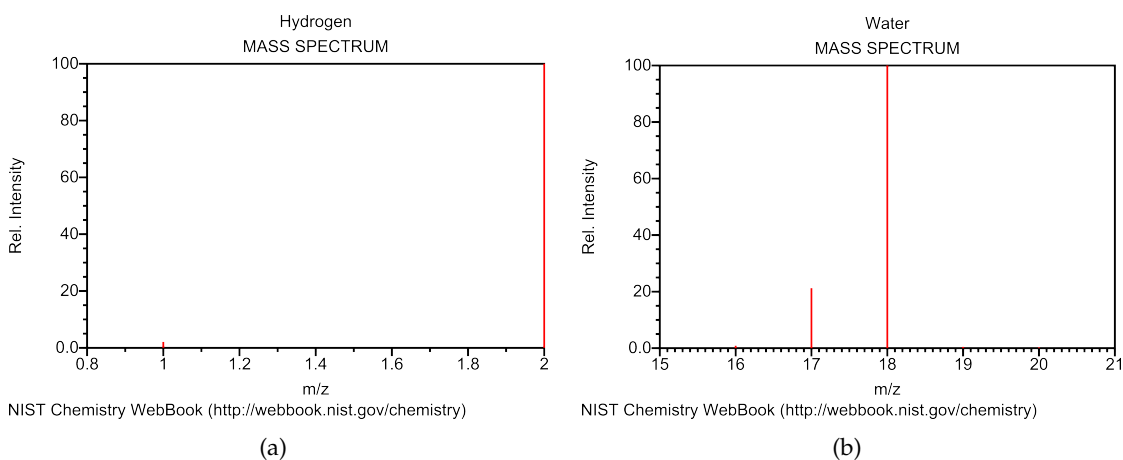

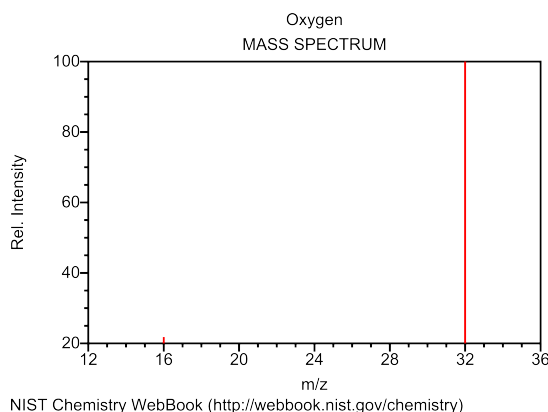*Figure 5.8:* EI mass spectra of H_2 and H_2O (from [87] and [88])

Figure 5.9: EI mass spectrium of O_2 (from [89])

Limit of detection, limit of quantification

The limit of detection (LOD) and the limit of quantification (LOQ) for H_2 and O_2 have to be determined.

The LOD is defined as "the smallest concentration that can be reported with a certain level of confidence" [90, p 214]. The minimum distinguishable analytical signal S_{LOD} is taken as the sum of the mean blank signal, $\bar{S}_{bl}$, plus three times the standard deviation of the blank, s_{bl} (signal-to-noise ratio is 3; 3σ-criterion) [64, p 20], [91, p 31], [92], [93, p 24], [90, p 214], [94]:

$$S_{LOD} = \bar{S}_{bl} + 3s_{bl} \tag{5.6}$$

By substituting S_{LOD} into the linear calibration function

$$S = kx + d, \tag{5.7}$$

where S, k, x and d denote signal, slope, concentration and y-intercept, respectively, the limit of detection, x_{LOD}, can be calculated:

$$x_{LOD} = \frac{S_{LOD} - d}{k} = \frac{\bar{S}_{bl} + 3s_{bl} - d}{k} \tag{5.8}$$

If the measured mean blank value is set identical to the y-intercept of the calibration curve ($d = \bar{S}_{bl}$; $\bar{S}_{bl}$ is "forced" to be a point of the calibration curve) the LOD is:

$$x_{LOD} = \frac{3s_{bl}}{k} \tag{5.9}$$

[90, p 214], [94], [95, 714A].

The LOQ is defined in analogy to the LOD, but with another multiple of s_{bl} in equation 5.6. While consensus seems to exist for the multiple of s_{bl} in the definition of the LOD, this is not the case for the LOQ (defined as six in [96, p 36], nine in [94] and ten in [91, p 31] and [93, p 24]).
In this work, the LOQ is taken to be

$$x_{LOQ} = \frac{10s_{bl}}{k}, \tag{5.10}$$

since this is the most strict criterion.

From the two detectors available in the Pfeiffer OmniStar GSD320 (SEM and Faraday cup) the SEM was chosen for its higher sensitivity. According to the data sheet for the OmniStar GSD320 [84] the LOD is below 1 ppm.

In order to find the concentration range for which the calibration had to be done and to check whether the mass spectrometer is capable of detecting the produced hydrogen, the expected H_2 concentration was estimated from DC measurements on an LSF64 microelectrode (circle with 200 µm diameter) on YSZ [47] (see fig. 5.10).
The amount of charge needed to produce one mol of hydrogen according to

$$H_2O + 2\,e^- \longrightarrow H_2 + O^{2-} \tag{5.11}$$
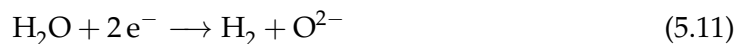
is $2F$. Therefore, the volume of (perfect) gas produced per unit time can be calculated in analogy to equation 5.5:
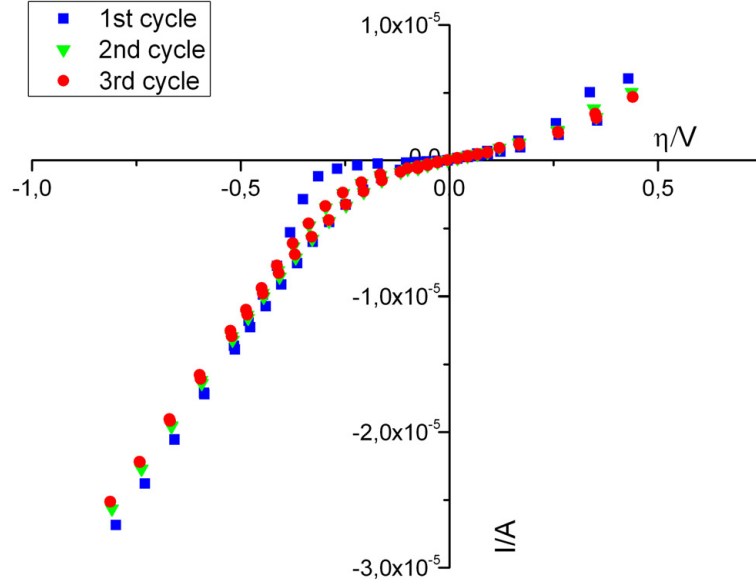
$$\frac{V}{t} = \frac{I \cdot RT}{2F \cdot p} \tag{5.12}$$

Figure 5.10: Current-overpotential (*I-η*) curve measured on an LSF64-microelectrode (microstructured Pt grid on top, diameter=200 μm) on a YSZ substrate in reducing atmosphere (approx. 2,4% H_2, 2,6% H_2O, 95% Ar) (from [47]).

The volume fraction in the gas stream that leaves the sample holder, x_{H_2}, is then

$$x_{H_2} = \frac{\frac{V}{t}}{\text{carrier gas flow}} \tag{5.13}$$

From figure 5.10 it can be estimated that at ≈ 0.5 V overpotential the current through the 200 μm microelectrode was about 1×10^{-5} A. As the microelectrode was covered with a 10×10 μm Pt thin film grid, only a quarter of the original surface area remains, giving a current density *i* of

$$i = \frac{1 \cdot 10^{-5} \text{A}}{1/4 \cdot \left(100 \cdot 10^{-6}\right)^2 \pi \text{ m}^2} = 1,27 \cdot 10^3 \text{ A/m}^2. \tag{5.14}$$

The surface area *A* of the LSF64 electrode with thin film grid (see figure 3.6) on the SOEC, of which only the inner circle was used (outer ring was not contacted), is approximately[2]

$$\underbrace{\left(2,5 \text{ mm}\right)^2 \pi \cdot \frac{4}{5}}_{\text{thin lines cover one fifth of the area}} - \underbrace{3 \cdot 5 \text{ mm} \cdot 30 \text{ μm}}_{\text{covered by thick lines}} = 15,26 \text{ mm}^2 = 1,526 \times 10^{-5} \text{m}^2. \tag{5.15}$$

Therefore the current *I* through the cell is

$$I = i \cdot A = 1,27 \times 10^3 \text{ A/m}^2 \cdot 1,526 \times 10^{-5} \text{m}^2 = 1,94 \times 10^{-2} A \approx 20 \text{ mA}, \tag{5.16}$$

which corresponds to a gas volume (perfect gas, $p = 1 \times 10^5$ Pa, $T = 23$ °C) produced per unit time of about 0,15 ml/min. With an incoming gas flow of 25 ml/min this gives a hydrogen concentration of roughly **0,6 %** (= 6000 ppm).

---

[2]The area where thick and thin lines cross is counted twice but this error can be neglected.

It follows that the amounts of hydrogen expected at $\eta \approx 0,5$ V should be well above the LOD given in the data sheet [84].

Drift of the MS background signal

In order to find out whether the MS signals drift with time, several calibration curves were recorded in different points in time. Possible causes for drifting signals could be:

- desorption/adsorption to/from MS sample inlet chamber
- temperature changes in the sample inlet chamber caused by heating by filament
- temperature changes of the detector

5.2.3 Results

Mass interference

Figure 5.11 shows the ion currents recorded by the MS as a function of time for a calibration. The concentration of the analyte was increased step by step.
The $m/z = 2$ signal reflected the increase in concentration while the $m/z = 1$ signal remained virtually constant (fig. 5.11 (a)). Therefore, the $m/z = 2$-signal was chosen to quantify H_2 (cf. also figure 5.8 (b)).
For the detection of O_2 both the $m/z = 16$ and $m/z = 32$ signals could be used as they both responded to the changes in concentration (fig. 5.11 (b)).

Limit of detection (LOD) and limit of quantification (LOQ)

While the H_2 calibration curves (figure 5.13) and the O_2 calibration curve using the $m/z = 16$- signal showed linear behaviour, the calibration curves for O_2 using the $m/z = 32$ signal can better be described by a polynomial of second degree (figure 5.14). Hence, the LOD and LOQ for O_2 ($m/z = 32$) was determined from a linear fit of the first few points of the calibration curves.
The LODs and LOQs for hydrogen are listed in table 5.2, those for oxygen in table 5.3.

Table 5.2: LODs and LOQs for H_2 calibration.

	calibration date	LOD/ppm	LOQ/ppm
	03/09/2012	1,20	3,90
	22/10/2012	0,95	3,16
mean value		**1,06**	**3,53**

Drift of the MS background signal

Signals vs. time in the range of hours   Generally, when a calibration curve was recorded, it took around 15-30 min until the MS signals became constant (flow schemes see subsection 5.2.1). When doing an electrolyis experiment, however, it took much longer for the signals to stop changing (several hours, see figure 5.12).
Hence, an influence of the SOEC measurement setup on the signals as a function of short time is likely.
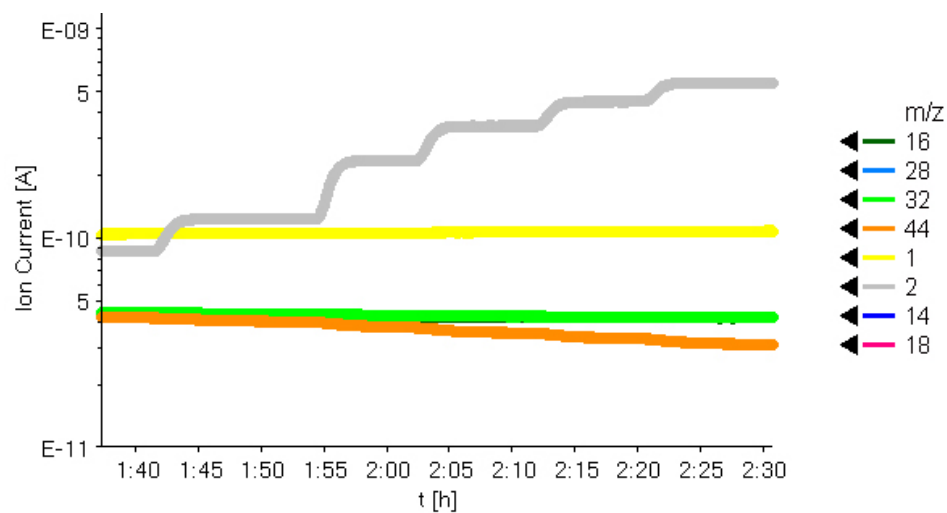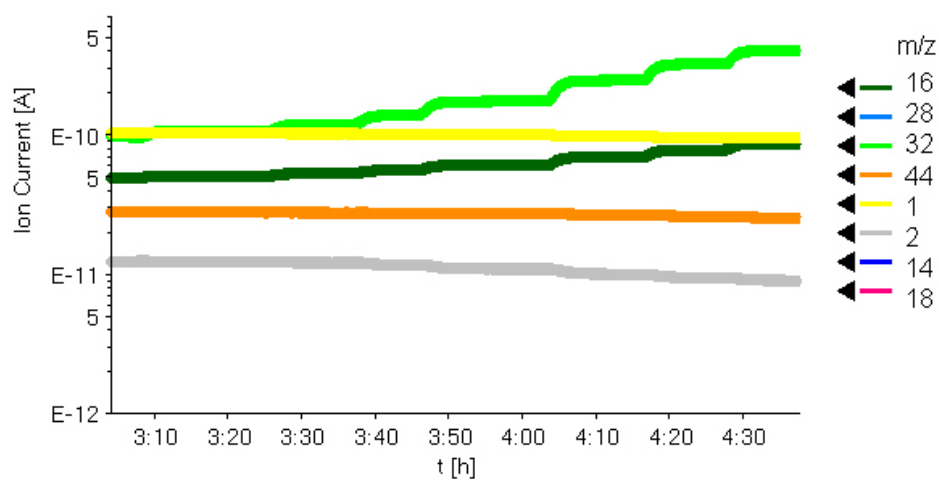
Figure 5.11: MS signals vs. time for (a) H_2 calibration and (b) O_2 calibration. (a): As the concentration of H_2 is increased stepwise, the $m/z = 2$ signal responds, whereas the $m/z = 1$ signal remains constant. (b): For the quantification of O_2 both the $m/z = 32$ and the $m/z = 16$ signal can be used.

Table 5.3: LODs and LOQs for O_2 calibration

(a) using the $m/z = 32$ signal

calibration date	LOD/ppm	LOQ/ppm
03/09/2012	1,38	4,60
23/10/2012	2,02	6,72
25/10/2012	2,14	7,14
mean value	**1,85**	**6,15**

(b) using the $m/z = 16$ signal

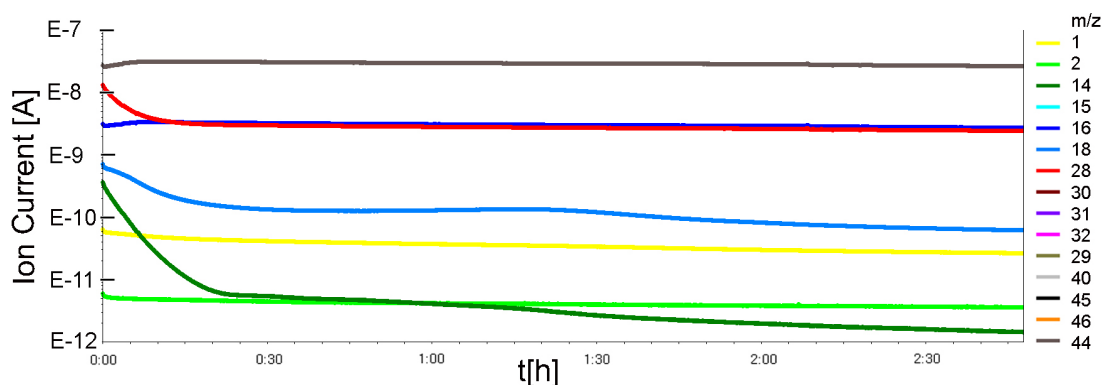| calibration date	LOD/ppm	LOQ/ppm
03/09/2012	12,69	42,29
23/10/2012	7,96	26,54
25/10/2012	9,55	31,83
mean value	**10,07**	**33,55**

Figure 5.12: MS signals vs. time. For the flow scheme see fig. 3.7 (CO_2/Ar supplied to inner gas chamber, MS at gas outlet of inner gas chamber; Ar supplied to outer gas chamber). The gas valves were opened at around 0:00 (far left in the figure) and 3 hours later, the signals were still drifting.

Signals vs. time in the range of days/months Figures 5.13 and 5.14 show several calibration curves (i.e. the SOEC setup was not part of the flow scheme) for H_2 and O_2, respectively, recorded at differents points in time, tables 5.4 and 5.5 contain the parameters of the fitted curves.

For the H_2 calibrations there is a large difference in the slopes of the calibrations done on a few consecutive days in March 2012 and the two calibrations done around 5,5 months and seven months later. One reason that can be excluded, due to arguments presented in the following paragraphs, are slightly different experimental conditions: The curves with the higher slopes were recorded without moistening (grey stars in fig. 5.13) or with bubbling through the gas washing bottle but without using a glass frit (denoted by "m"; yellow triangles, black squares, pink triangles and red circles in fig. 5.13; without the frit, the fraction of H_2O in the gas mixture can be expected to be a little lower). Hence, the slopes of curve "03/09/2012, frit" and curve "22/10/2012, frit"

being much lower could be due to the dilution of H_2 signals caused by more effective moistening while using the frit. This dilution effect, however, leaves the slope of the calibration curve almost unchanged. The data plotted as open green triangles in fig. 5.13 was obtained by multiplying the MS signals from measurement "03/09/2012, frit" (light blue diamonds) by $1/f_{H_2O}$, the reciprocal of the H_2O dilution factor[3] :

$$\text{signal "calculated from 03/09/2012, dry"} = \frac{1}{f_{H_2O}} \cdot \text{signal "03/09/2012"} \qquad (5.20)$$

The slopes of "03/09/2012, frit" (frit; most effective moistening) and "calculated from 03/09/2012, dry" (calculation supposes not moistening at all) are almost identical and represent the difference between the most effective moistening and the dry gas stream. Hence the dilution effect by moistening cannot cause the strongly different calibration curves.

Moreover, it is remarkable that in a period of around 5,5 months (measurements in March 2012 to measurement "03/09/2012, frit" at the beginning of September) drift is extremely strong, while it is negligible in a period of about 1,5 months (between measurements "03/09/2012, frit", Sept. 3rd, and "22/10/2012, frit", Oct. 22nd).

The O_2 calibrations show similar irregular drifting. The two calibrations "03/09/2012" (black squares and red circles) and "23/10/2012" (green triangles and blue triangles), recorded on Sept. 3rd and Oct. 23rd (distance in time $\approx$ 1,5 months), respectively, differ less than "23/10/2012" (green triangles and blue triangles) and "25/10/2012" (light blue diamonds amd pink triangles), recorded on Oct. 23rd and Oct. 25th, respectively (distance in time only two days!).

The reasons for the significantly different (sets of) calibrations at different points in time (figs. 5.13 and 5.14) are not understood so far. Their clarification, however, is far beyond the scope of this study. Consequently, only calibration data recorded immediately before the SOEC experiments can be regarded as reliable.

For the H_2 calibrations used in the SOEC measurements, a drift correction was attempted by replacing the blank value of the calibration curves by a blank value measured directly before each electrolysis experiment. This results in a calibration function

---

[3] f_{H_2O} can be calculated as follows:

The dry volume, V_{dry}, is increased by the volume of water, V_{H_2O}, to give the volume of the gas mixture after moistening, V_{wet}:

$$V_{dry} + V_{H_2O} = V_{wet} \qquad (5.17)$$

Assuming that all gases are perfect, the volume percentage of water in the moistened gas mixture, V_{H_2O}/V_{wet}, and the pressure of water in the moistened gas mixture are identical.

$$\frac{p(H_2O)}{p_{tot}} = \frac{V_{H_2O}}{V_{wet}} \quad \Rightarrow \quad V_{H_2O} = \frac{p(H_2O)}{p_{tot}} \cdot V_{wet} \qquad (5.18)$$

The vapor pressure of water in the moistened gas mixture, $p(H_2O)$, is the vapor pressure of water at temperature T ($p(H_2O) = 26,453$ mbar [79]). p_{tot} denotes the total pressure of the moistened gas mixture and is around 1 bar. Substituting equation 5.18 into equation 5.17 yields

$$\frac{V_{dry}}{V_{wet}} = 1 - \frac{p(H_2O)}{p_{tot}} = f_{H_2O} \qquad (5.19)$$
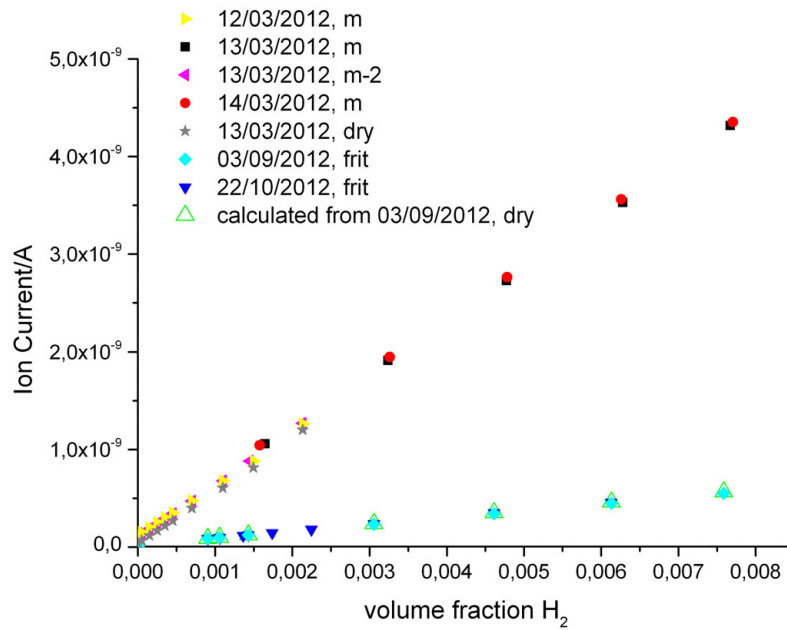
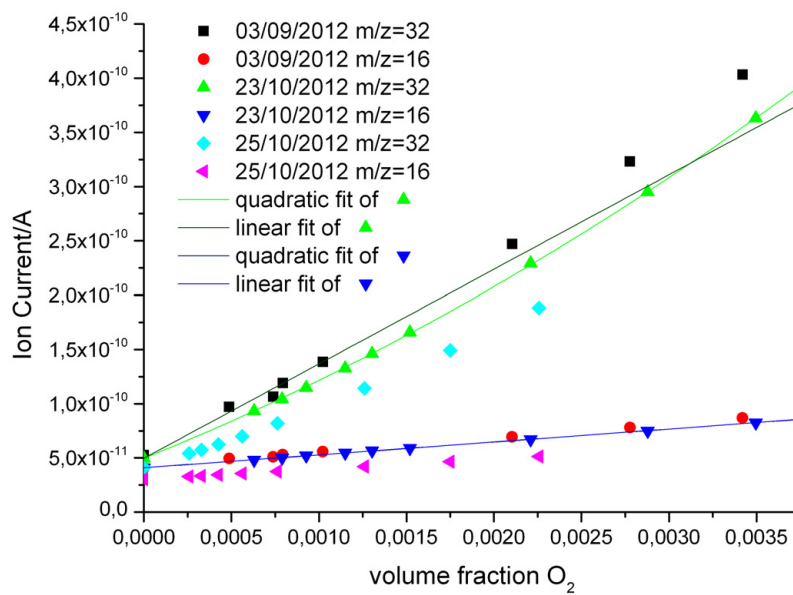*Figure 5.13:* Calibrations for H_2 at different points in time. All curves are linear.

Figure 5.14: Calibrations for O_2 at different points in time. The curves using $m/z = 16$ are linear, while the curves using $m/z = 32$ ought to be described by a polynomial of second degree (see fitted curves - the polynomial describes the data much better than the straight line).

Table 5.4: Calibration curves for H_2. k and d are the slope and the y-intercept (= measured blank value) of the calibration curves, respectively.

calibration date	k	d	moistening
13/03/2012	5.28×10^{-7}	4.52×10^{-11}	none
12/03/2012	5.22×10^{-7}	1.21×10^{-10}	yes, but no frit
13/03/2012	5.42×10^{-7}	1.03×10^{-10}	yes, but no frit
13/03/2012	5.41×10^{-7}	1.53×10^{-10}	yes, but no frit
14/03/2012	5.50×10^{-7}	1.30×10^{-10}	yes, but no frit
03/09/2012	7.07×10^{-8}	1.74×10^{-11}	frit
22/10/2012	7.25×10^{-8}	1.65×10^{-11}	frit

Table 5.5: Calibration curves for O_2. a, b and c are the coefficients of the polynomial $y = ax^2 + bx + c$, respectively. c is the measured blank value.

(a) using the $m/z = 32$-signal

calibration date	a	b	c
03/09/2012	7.79×10^{-6}	7.59×10^{-8}	5.26×10^{-11}
23/10/2012	7.1×10^{-6}	6.49×10^{-8}	4.97×10^{-11}
25/10/2012	7.65×10^{-6}	4.82×10^{-8}	4.09×10^{-11}

(b) using the $m/z = 16$-signal

calibration date	k	d
03/09/2012	1.35×10^{-8}	4.10×10^{-11}
23/10/2012	1.19×10^{-8}	4.09×10^{-11}
25/10/2012	9.31×10^{-8}	3.03×10^{-11}

that is shifted along the y-axis by the difference between the two blank values, and ensures that the LOD is above the hydrogen concentration corresponding to the $m/z = 2$ signal measured before starting the electrolysis. The measured hydrogen concentrations of produced hydrogen (i.e. the difference between before and during the electrolysis) are not affected because the slope of the calibration curve remains the same. These new calibration functions and the new LODs and LOQs for H_2 are given in subsection 5.5.4, table 5.7 (page 84).

5.3 Measurements on LSF64-YSZ-LSF64 cells

5.3.1 Tasks

Macroscopic LSF64-YSZ-LSF64 cells were compared with microelectrodes used in [47] by means of AC and DC measurements in order to figure out if macroscopic LSF64 electrodes exhibit the same favourable properties (e.g. stability, conductivity) needed to build an SOEC, as the microscopic ones.
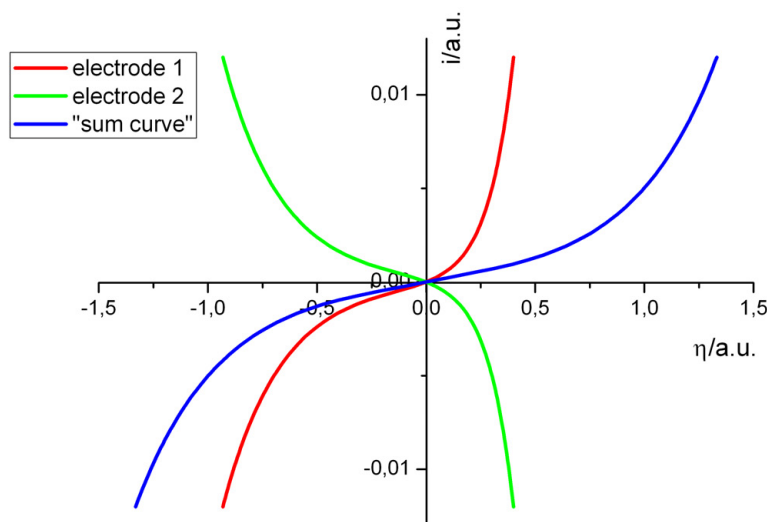
Figure 5.15: Current-voltage curves for an electrochemical cell with symmetrical electrodes calculated from a Butler-Volmer type single electrode current-voltage curve with $\alpha = 0,7$ (asymmetric). The blue and red curves represent the current-voltage behaviour of the single electrodes, the green curve is the "sum curve" (symmetric). The currents i and overpotentials η plotted are: $i_{total} = i_{electrode\ 1} = -i_{electrode\ 2}$ and $\eta_{total} = \eta_{electrode\ 1} - \eta_{electrode\ 2}$.

DC measurements

High C mode and acquisition time The Keithley 2611A source meter unit, which was used for DC measurements, features a special measuring mode for sample with capacities between 100 nF and 50 µF (referred to as "high C mode"). In order to assess whether this mode yields better results than the normal measuring mode, both modes were tested. Furthermore, different acquisition times for the current data in a potentiostatic measurement were compared. The experience acquired during these experiments was helpful for choosing the parameters for the DC measurements of the SOEC samples.

Comparing micro- with macro-measurements In microelectrode measurements, the voltage drop at the porous, macroscopic counter electrode can usually be neglected. Thus, after subtraction of the potential drop in the electrolyte, the current-overpotential curve for a single electrode is directly obtained. In contrast to this, for the macroscopic cells, the voltage between two (almost) identical electrodes is measured. The resulting current-voltage curve for the cell is symmetrical, even though the curve for one electrode can be asymmetrical (see figure 5.15). From the current-voltage curve measured on a microelectrode (data see figure 5.10) a current-voltage curve, expected for the a symmetric sample can be calculated. This "sum curve" can then be compared to the current-voltage curves measured on macroscopic LSF64-YSZ-LSF64 cells in this work.

EIS measurements

If the EIS measurements are performed without bias, the impedance values for one electrode can be calculated by dividing the measured impedance by two because the

impedance of the two electrodes is probed in the same point on the current-voltage curve (in the origin) and is therefore the same. For the DC resistance, for example, this means that the slopes of the two current-voltage curves are identical.

The considerations for comparing results from AC and DC measurements of LSF64-YSZ-LSF64 cells with those from measurements on microelectrodes are no longer valid if the two macroscopic electrodes show different current-voltage curves. As a consequence of the sample preparation process, one of the electrodes on an LSF64-YSZ-LSF64 cell was treated slightly differently: During PLD of the second electrode, the one that had already been deposited had to be heated as well, which might change its properties. Additionally, one electrode can be expected to behave differently due to the problems during the sputter deposition of Ti described in subsection 3.1.1.

Two kinds of experiments were carried out: Measurements in reducing atmosphere (approx. 2,4% H_2, 2,6% H_2O and 95% Ar) and measurements that were started in air, and then, during further measuring cycles, the reducing gas mixture was turned on.

5.3.2 Results

DC measurements

As described in section 2.2.2, the overpotential was calculated from

$$\Delta E_{cell} = \eta_{electrode\,1} + I \cdot \underbrace{R_{electrolyte}}_{\text{measured by EIS}} + \eta_{electrode\,2} + \underbrace{\Delta E_{Nernst}}_{=0} \tag{5.21}$$

$$\Rightarrow \quad \eta_{CE} + \eta_{WE} = \sum \eta = \Delta E_{cell} - IR_{electrolyte} \tag{5.22}$$

In the macroscopic sample holder with one gas chamber, ΔE_{Nernst} is zero if currents are low. After subtraction of the potential drop at the electrolyte, which can be determined by means of EIS (for the justification see page 71), the sum of the overpotentials of the two electrodes, denoted by $\sum \eta$, is obtained.

High C mode and acquisition time DC measurements with or without high C mode were reproducible (see figure 5.16).
The measurements in high C mode showed less noise. However, measurements with and without high C mode yielded slightly different curves, as can be seen in figure 5.17.

Acquisition times between 60 s and 5850 s were tested. While around the origin of the current-voltage curve the current became constant in shorter acquisition times (e.g. 600 s, see figure 5.18 (a)), near the maximum voltages that were applied, -0,5 V and +0,5 V, the current was not constant even after 5850 s (see figure 5.18 (b)).
At the beginning of most of the measurements, which started at the lowest voltage (-0,5 V), the absolute value of the current increased with time. A capacitive current can be excluded because during the charging process, the absolute value of current would decrease. Additionally, this phenomenon does not correspond to the characteristic frequency of the $R \parallel C$ element observed in the impedance spectra (see figure 5.21).
The observed behaviour could be related to an electrochemical activation effect, "i.e. the enhancement of the catalytic activity of the electrode with respect to oxygen surface exchange by dc bias treatments" which was observed on LSF64 by [97].
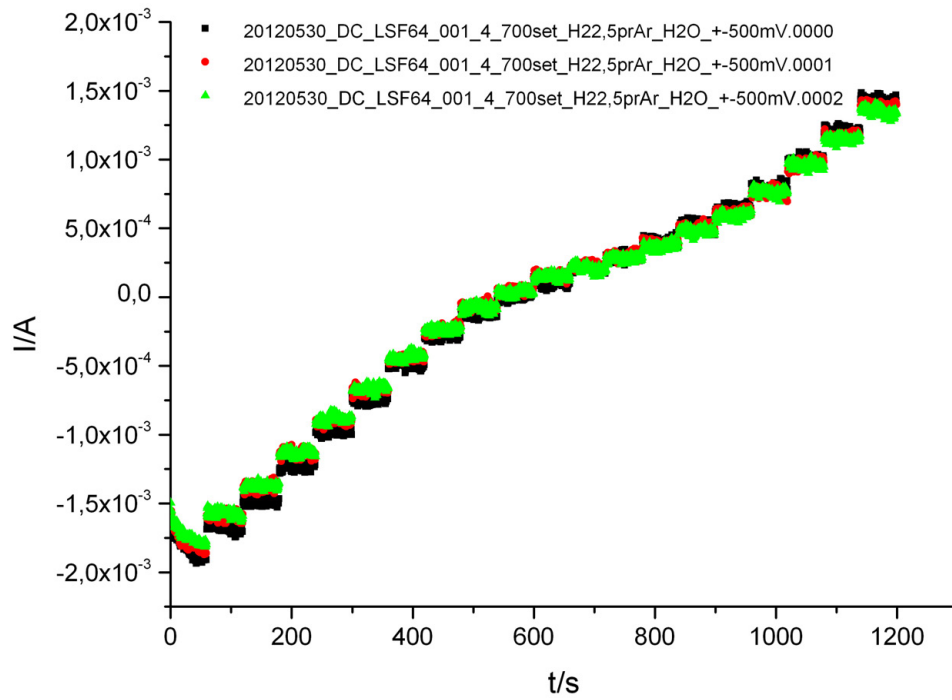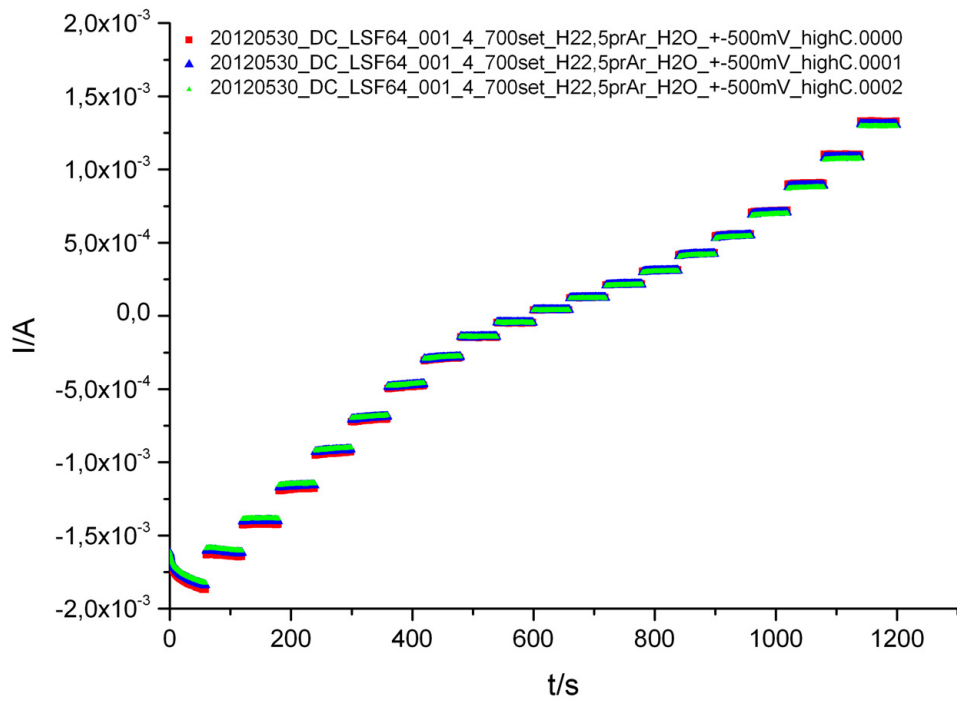
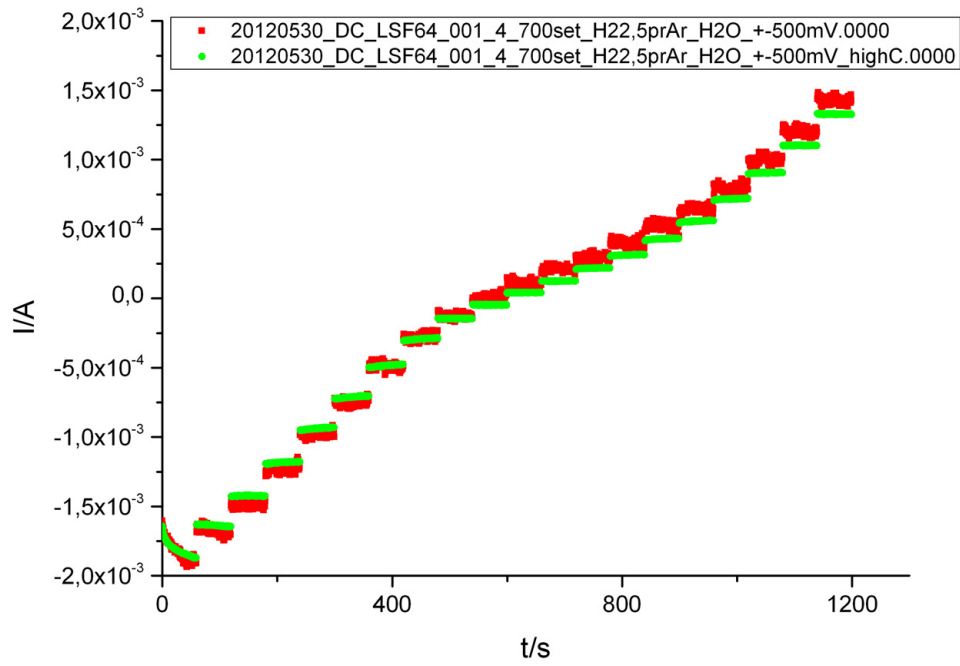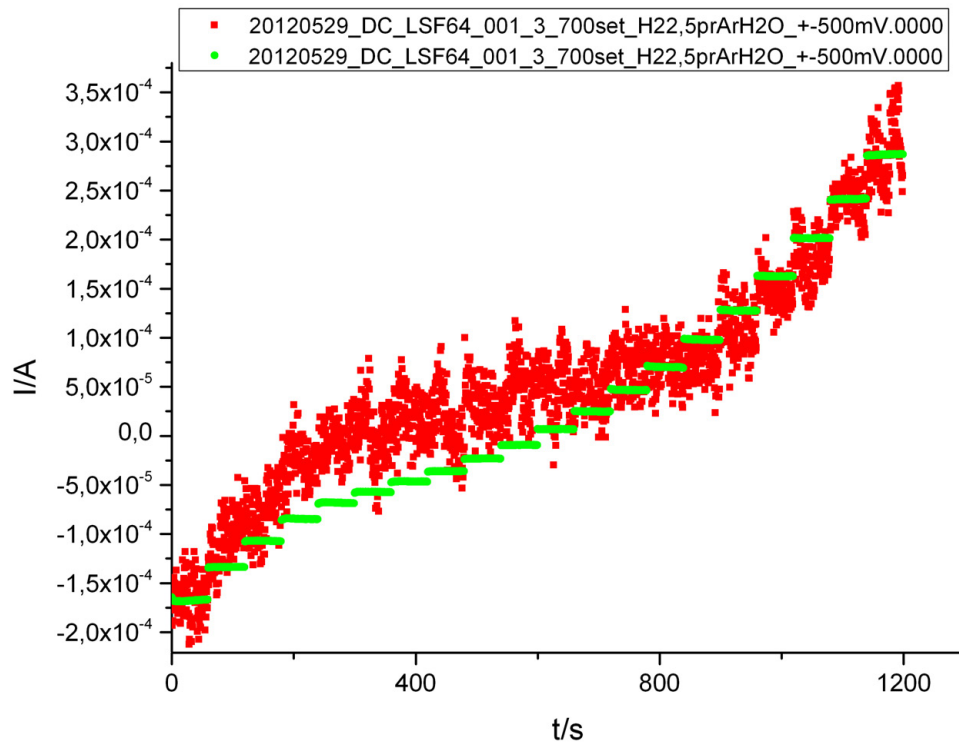*Figure 5.16:* Several measurements of the same sample without (a) and with high C mode (b). The measurements are reproducible, the high C mode reduces noise. Each current step reflects an increase of the applied voltage by 50 mV, starting from -0,5 V.

(a)

(b)

Figure 5.17: Comparison of DC curves measured with (red curves) and without high C mode (green curves) for samples LSF64_001_4 (a) and LSF64_001_3 (b). Each current step reflects an increase of the applied voltage by 50 mV, starting from -0,5 V.
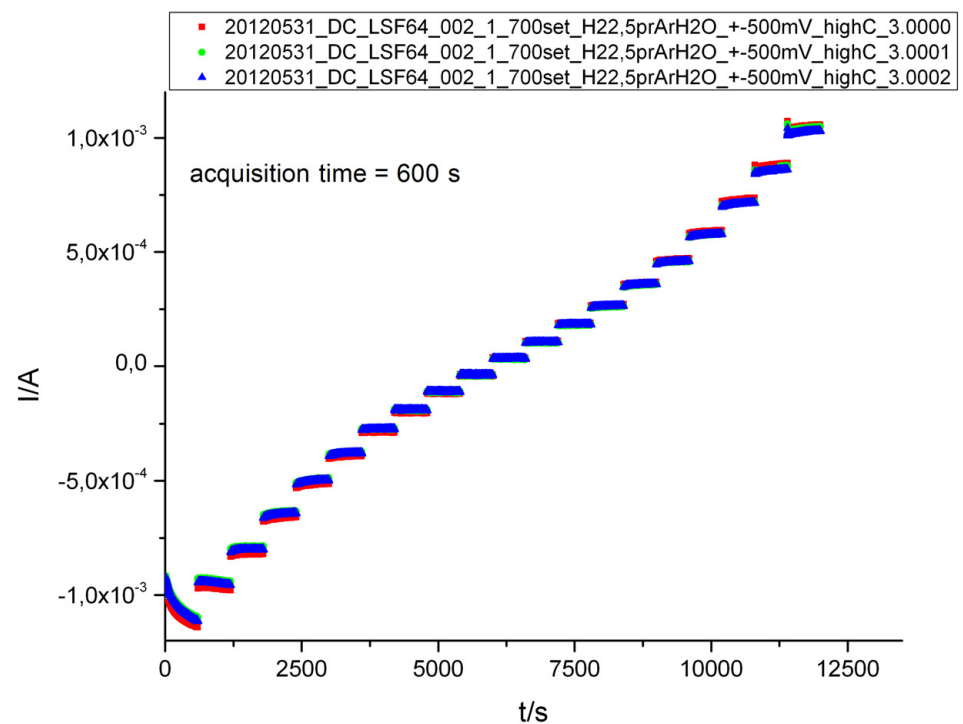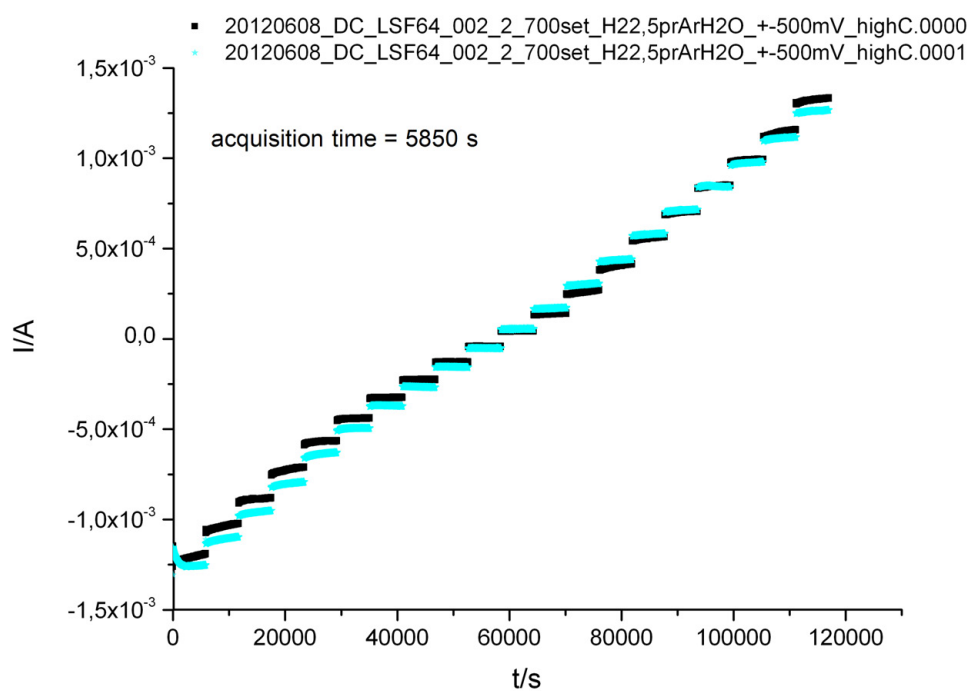
Figure 5.18: The current measured on sample LSF64_002_1 and LSF64_002_2 as a function of time with acquisition time = 600 s (a) and acquisition time = 5850 s (b), respectively. Each current step reflects an increase of the applied voltage by 50 mV, starting from -0,5 V.

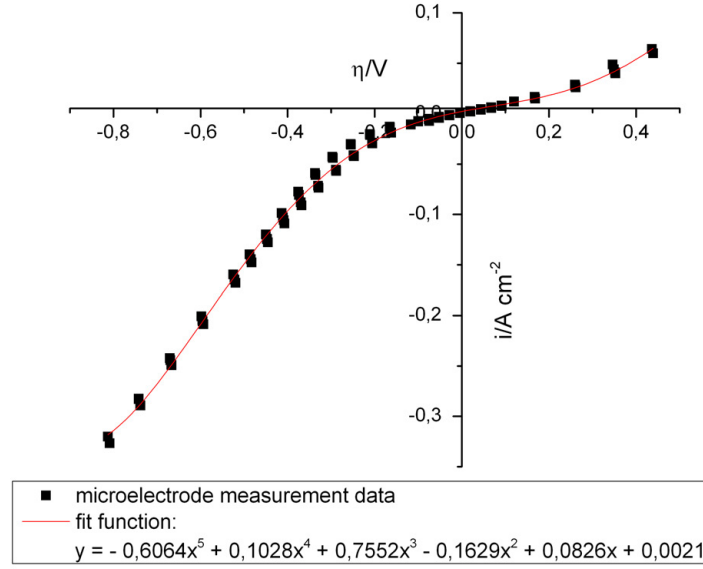*Figure 5.19:* Data points from [47] with fit function (polynomial of fifth degree).

Comparison of micro- with macro-measurements A current-voltage curve for an LSF64-YSZ-LSF64 cell was calculated from a current-voltage curve measured on a single LSF64 microelectrode in [47]. First, current densities were calculated from the microelectrode data from [47] (cycles 2 and 3, shown in figure 5.10). The electrode was 200 µm in diameter and had a 10×10 µm metal grid on top, that covers three quarters of the surface. The free surface area is therefore $100^2\pi \cdot 1/4$ µm$^2 \approx 7.854 \times 10^{-5}$ cm^2. The data was then fitted with an analytical function (polynomial of fifth degree, see figure 5.19), without giving any physical meaning to the fit parameters. Subsequently, the data points of a "sum curve" were calculated as described above (subsection 5.3.1, fig. 5.15). In order to plot current density i vs. $\sum \eta$ curves for the macroscopic LSF64-YSZ-LSF64 samples, the active electrode area, which is smaller than the whole surface area of the $0{,}5\times0{,}5$ cm samples (see section 4.2), was estimated based on the optical microscope images. An area of $\approx 0{,}126$ cm^2 was covered by a 10×10 µm metal grid, which leaves one quarter of the electrode area open $\Rightarrow$ area is $0{,}126/4 = 0{,}031$ cm^2. The resulting i vs. $\sum \eta$ curves are plotted in figure 5.20. The measured curves of one and the same LSF64-YSZ-LSF64 sample are mostly reproducible but the curves for different samples deviate to a certain degree. The differences between the samples could be due to the problems during sputtering which caused parts of the metal grid to fall off in the ultrasonic bath during lift-off (see subsection 3.1.1 and section 4.2). As the grid was needed to ensure good lateral electron distribution [47], a partly missing grid on one electrode of a cell results in a smaller active electrode surface area which leads to a higher resistance of this electrode. The cell is no longer symmetric and asymmetric curves, with the shape depending on the surface area being covered by the remaining grid, are obtained. Another reason for the asymmetric DC curves can be that the electrode deposited during the first PLD step is heated again in the second PLD step, which might change its conductivity or surface properties.

The "sum curve" calculated from measurements on a microelectrode (golden line in fig. 5.20) is in qualitative agreement with the ones measured on the macroscopic LSF64-
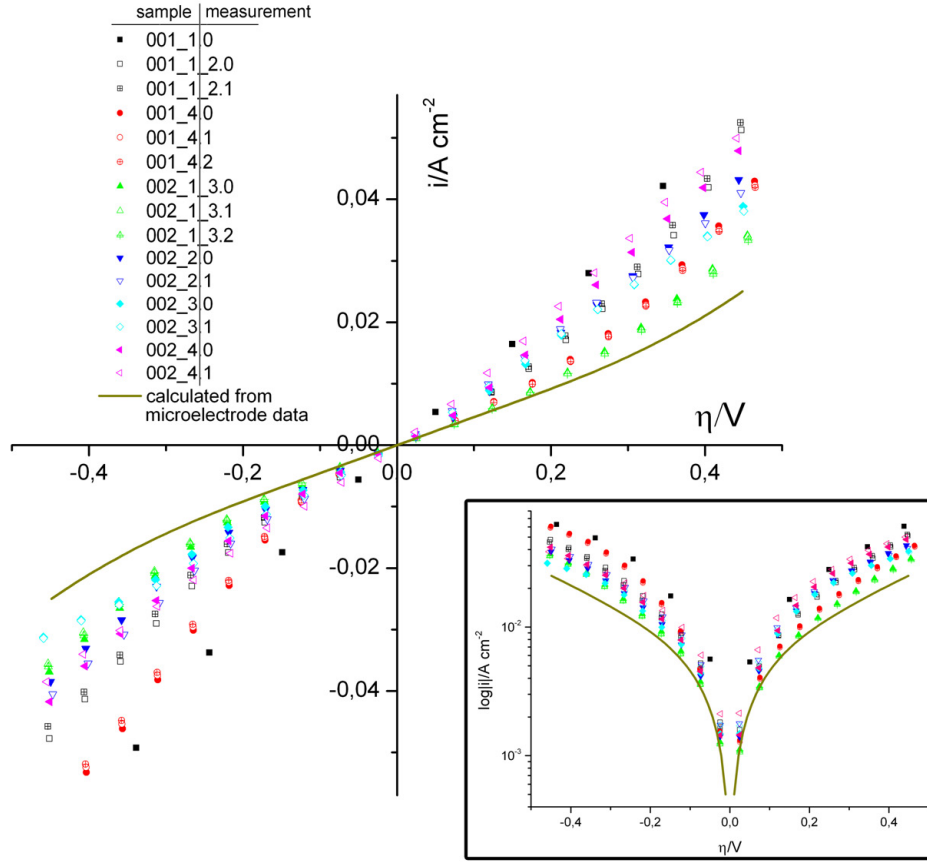
Figure 5.20: Current-voltage curves measured on macroscopic LSF64-YSZ-LSF64 cells compared with a curve that would have been obtained if two electrodes showing the behavior of the microelectrode measured in [47] would have been placed on a symmetric LSF64-YSZ-LSF64 cell (golden line labelled "calculated from microelectrode data"). In the log $|i|$ vs. η plot (insert) the similarity of the curves is most apparent. Several measurements on different samples are shown.

YSZ-LSF64 cells. The lower absolute current values of the "sum curve" can be explained by the temperature difference ("sum curve", [47]: 576°C; this study: 656-659°C). Under reducing conditions[4], the conductivity and therefore the current increase at higher temperature (see fig. 2.7, page 14). The same can be assumed for the electrochemical surface reaction.

---

[4]Gas mixture: 2,4% H_2, 2,6% H_2O, rest Ar, total pressure = 1 bar, see subsection 3.1.2. From the equilibrium

$$H_2 + \tfrac{1}{2} O_2 \rightleftharpoons H_2O \tag{5.23}$$

it follows that

$$p(O_2) = \left(\frac{p(H_2O)}{p(H_2) \cdot K} \right)^2 \approx 2 \times 10^{-25} \text{ bar}, \tag{5.24}$$

with K being the equilibrium constant, and $\log K \approx 12,392$ at 576°C $\approx$ 850 K (interpolation from [98]).
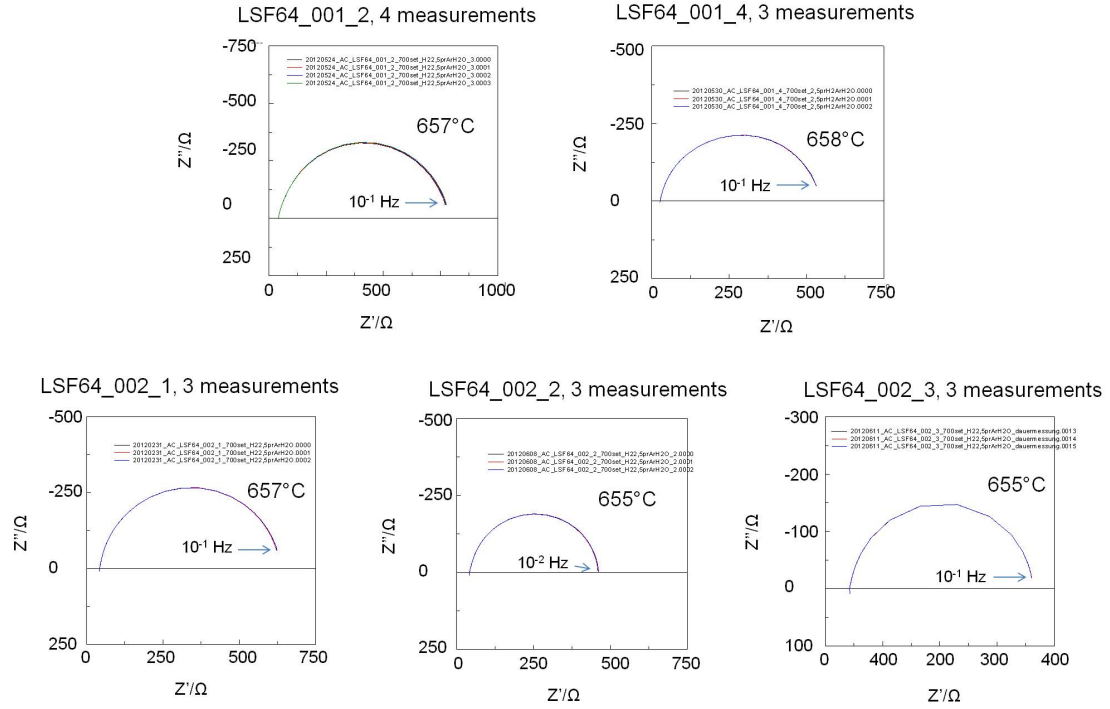
Figure 5.21: Impedance spectra measured on different LSF64-YSZ-LSF64 samples.

EIS measurements

Measurements in reducing atmosphere Figure 5.21 shows impedance spectra of six different samples. The spectra were reproducible and feature a semi-circle that has a positive x-intercept. The x-intercept is usually attributed to the ohmic resistance of the electrolyte [74], [99]. In order to check if R_{offset} can be interpreted as electrolyte resistance for the macroscopic samples used in this work, the conductivity σ_{offset} corresponding to R_{offset} was calculated ($\sigma_{\text{offset}} = \text{sample thickness}/(R_{\text{offset}} \cdot \text{sample area}) = 0,05\,\text{cm}/(R_{\text{offset}} \cdot 0,126\,\text{cm}^2)$) and compared to literature data ([100, pp 48,68,89], sample C1, barrier fit-model). Table 5.6 shows the conductivities calculated from the mean values of R_{offset} for several samples. The conductivities corresponding to R_{offset} are in agreement with the literature data for YSZ at the same temperature and therefore the high frequency offset was attributed to YSZ.

Table 5.6: Comparison of conductivities calculated from R_{offset} with literature data for YSZ conductivities at the same temperature [100, pp 48,68,89], showing that R_{offset} can be attributed to YSZ.

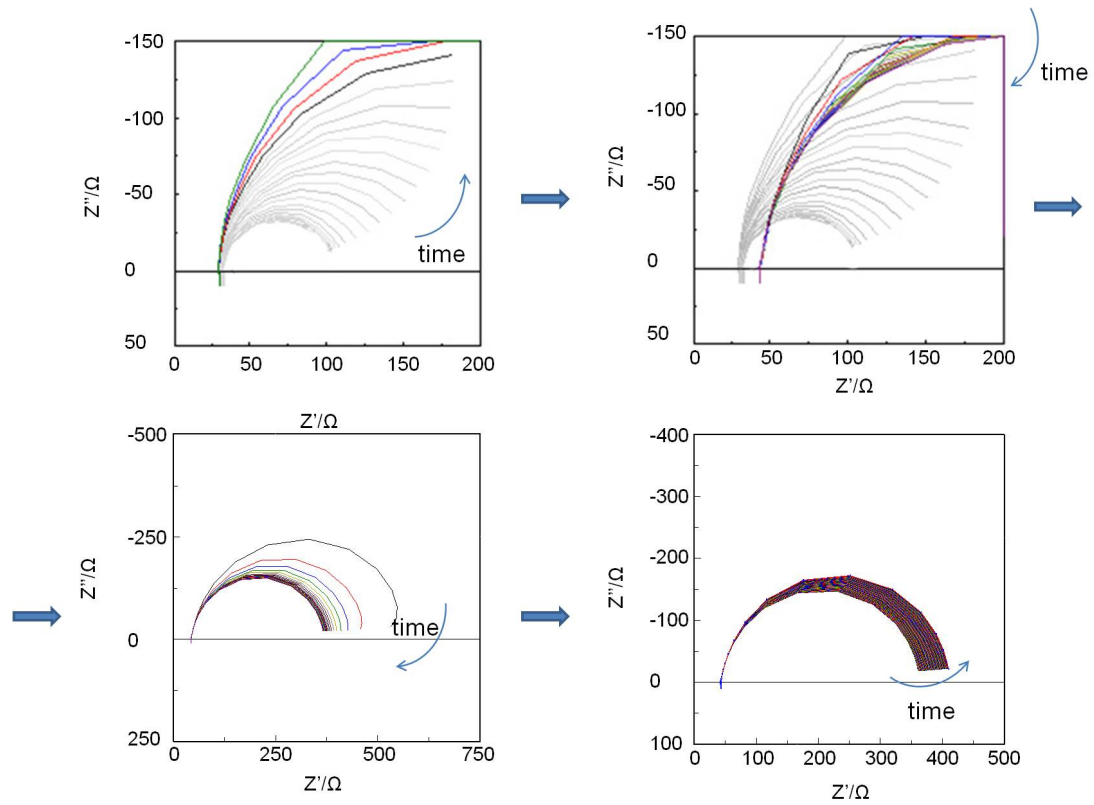| sample	$\sigma_{\text{offset}}/\text{S cm}$	$\sigma_{\text{offset, lit.}}/\text{S cm}$
LSF64_001_2	9.7×10^{-3}	8.5×10^{-3}
LSF64_001_4	1.5×10^{-2}	8.6×10^{-3}
LSF64_002_1	9.5×10^{-3}	8.5×10^{-3}
LSF64_002_2	9.6×10^{-3}	8.3×10^{-3}
LSF64_002_3	9.5×10^{-3}	8.3×10^{-3}

Figure 5.22: Impedance spectra of LSF64_002_3. The measurements were started in air (top left). The impedance increased with time. After a certain time the reducing gas mixture had filled the sample holder and the impedance started to decrease (top right). The offset on the x-axis jumped to a higher value. Subsequently, the impedance decreased to a certain value (bottom left) and then started to increase very slowly (bottom right). The measurements in the top left, top right and bottom left picture were done in about three hours, the ones in the bottom right picture took a little more than seven hours.

The polarization resistances of different samples differ approximately by a factor of 2.

Measurements with change of gas atmosphere   Degradation in air was more pronounced than under reducing conditions: In figure 5.22, top left picture, the impedance increase in air over about an hour is shown - the low frequency intercept increases by about a factor of five. In the bottom right picture of figure 5.22 the increase is shown under reducing atmosphere - the increase by a factor of about 1,3 took around seven hours.

When a sample was measured during a change from air to reducig gas, the impedance stopped to increase upon arrival of the reducing gas mixture and the offset on the $Re(Z)$ axis jumped to a higher value. The impedance then became smaller until a certain value was reached. Subsequently, it started to increase again, but very slowly compared to the changes upon change of gas (see figure 5.22).
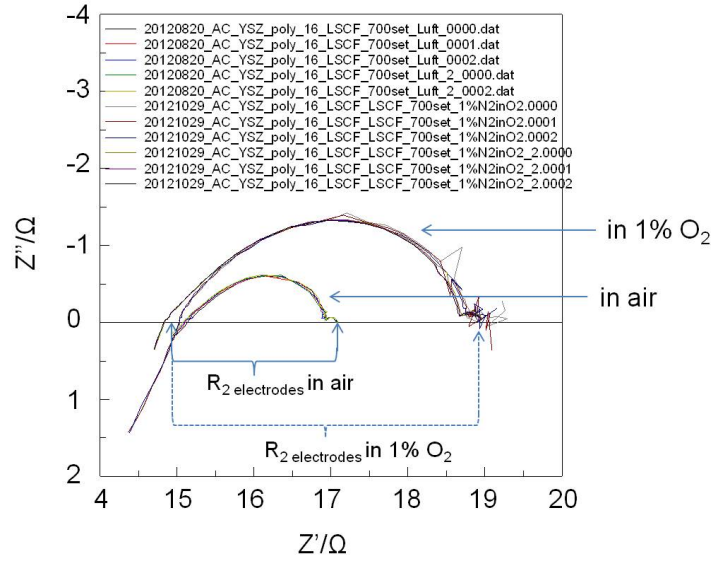
Figure 5.23: Impedance spectra of sample YSZ_poly_16_LSCF, measured in 1% O_2 in N_2 and in air. The impedance in air is smaller. The mean value of the DC resistance of both electrodes ($R_{2\,electrodes}$, width of both semi-circles) is $\approx 4{,}2\,\Omega$ in 1% O_2 and $\approx 2\,\Omega$ in air.

5.4 Measurements on LSCF6428-YSZ-LSCF6428 samples

5.4.1 "Anode quality test sample" for SOEC-003 – 005

Impedance spectra measured on YSZ_poly_16_LSCF, the symmetric cell with porous paste LSCF6428 electrodes, that served as a means to estimate the DC resistance of a porous LSCF6428 anode on the SOEC samples SOEC-003 to SOEC-005, are shown in figure 5.23.

Two semi-circles and a high frequency offset on the x-axis (R_{offset}) are visible. As for the LSF64-YSZ-LSF64 samples (see 5.3.2), the high frequency offset was interpreted as YSZ resistance, therefore the rest of the impedance was attributed to the electrode.

The DC resistance of both electrodes was taken from the spectrum (see fig. 5.23) and divided by two. The resulting DC resistance for 1 electrode, that was to be determined, was $\approx 2{,}1\,\Omega$ in 1% O_2 and $\approx 1\,\Omega$ in air.

Interestingly, the $\log p(O_2)$ dependence of the logarithm of the electrode conductivity is approximately $+1/4$:

$$\frac{\Delta \log(1/R)}{\Delta \log p(O_2)} = \frac{\log\left(\frac{R_{1\%\,O_2}}{R_{air}}\right)}{\log\left(\frac{p(O_2,air)}{p(O_2,1\%)}\right)} \approx 0{,}24 \tag{5.25}$$

This indicates that defect chemistry is involved in the rate limiting step of the electrochemical electrode process.

If DC bias is applied to the cell the DC resistance always decreases, as can be seen from a DC measurement in [81, p 27]. Therefore, the values measured without bias are the highest ones attainable and hence best suited to show that they are negligible
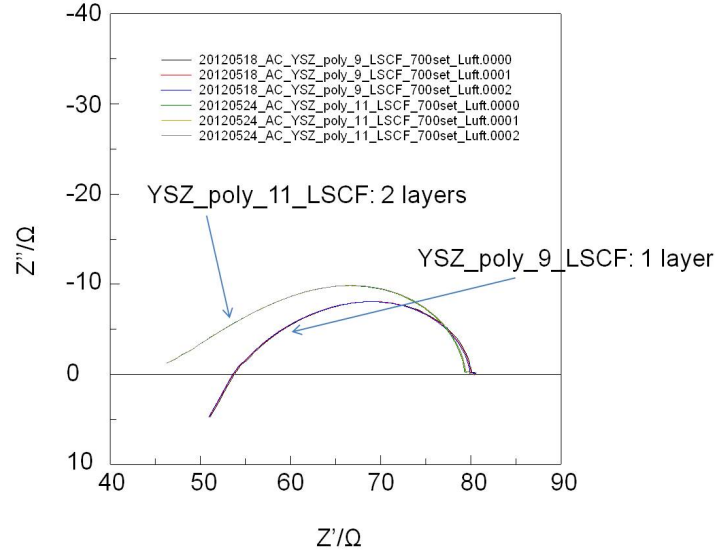
Figure 5.24: Impedance spectra of samples YSZ_poly_9_LSCF (at ≈ 651 °C) and YSZ_poly_11_LSCF (at ≈ 654 °C) measured in air. The sample with two layers of LSCF6428, YSZ_poly_11_LSCF, has a higher electrode resistance than the one with only one layer. The electrode resistances of both samples are larger than for sample YSZ_poly_16_LSCF (fig. 5.23), which is related to the fact that the LSCF6428 powder was ground dry, and terpineol was added afterwards, whereas powders for YSZ_poly_9_LSCF and YSZ_poly_11_LSCF were ground with terpineol (see subsection 3.2.1).

compared to the resistance values for the LSF64 thin film cathode on an SOEC sample: For SOEC-004 and 005 (measurements discussed in subsection 5.5.4) R_{CE} was compared to $R_{LSF} = R_{WE} + E_{OCV}/I$, with E_{OCV} being the open-circuit voltage. For the comparison the lowest possible R_{LSF} value (at the highest E_{LSF}) was chosen. The R_{CE}/R_{LSF} ratio was 0,0059 for SOEC-004 and 0,0010 for SOEC-005 showing that $\eta_{CE} \approx 0$ is valid.

5.4.2 One layer vs. two layers of LSCF6428

On sample YSZ_poly_9_LSCF, one layer of LSCF6428 was applied, while sample YSZ_poly_11_LSCF was coated with 2 layers of the electrode slurry. The cell with only one layer of electrode material showed a lower electrode impedance (5.24).
However, the electrolyte resistance is smaller for the double layer sample.
Additionally, it can be seen from comparing figure 5.24 with 5.23 that grinding the LSCF6428 powder without terpineol (i.e. dry) not only yields electrodes that show better mechanical stability (as described in subsection 3.2.1), but also exhibit lower polarization resistance.
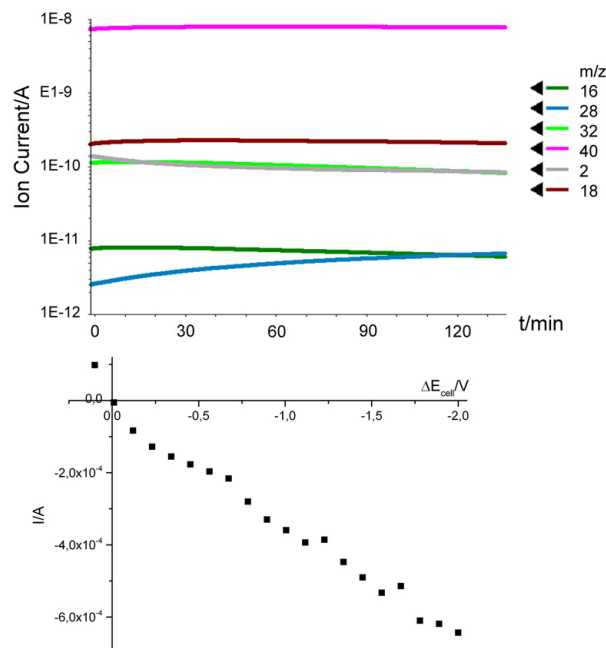
Figure 5.25: Measurement on SOEC-001 before microstructuring of the WE, with pure O_2 in the outer gas chamber: Current was flowing, but no hydrogen was produced. The current could be an "oxygen circling current". The plotted current values are mean values of the last 11 data points in the acquisition time of 360 s (acquisition time resolution = 0,5 s).

5.5 Measurements on SOEC samples

5.5.1 Effects of setup on results

"Oxygen circling current" hypothesis

As mentioned in subsection 3.3.1, paragraph "SOEC-001", the LSF64 electrode on sample SOEC-001 was not microstructured by photolithography and ion etching at first. During the water electrolysis experiments on this sample it was observed that although current was flowing, no hydrogen could be detected by the MS, if pure O_2 was present in the outer gas chamber of the SOEC sample holder (see figure 5.25). In contrast to this, hydrogen could be detected when pure N_2 was supplied to the outer gas chamber (see figure 5.26). This can be explained by the following considerations:

If O_2 is present, it can be incorporated on the part of the LSF64 electrode that reaches out into the outer gas chamber, provided that the lateral electronic conductivity is sufficiently high to bring electrons from the metal grid on LSF64 in the inner gas chamber to the part of the LSF64 thin film in the outer gas chamber (see figure 5.27). The hole conductivity of LSF64 is a few orders of magnitude higher at $p(O_2) = 1$ bar than at a $p(O_2) < 2$ ppm (in N_2), see subsection 2.1.1, on page 13. If this pathway is available, oxygen is only transported from one side of the cell to the other one, "circling" in the same gas chamber. Obviously, in such a situation the "oxygen circling" is the main contribution to the overall current, and the amount of produced hydrogen is below the LOD.

Figure 5.26: Measurement on SOEC-001 before microstructuring of the WE, with N_2 in the outer gas chamber: Current was flowing, hydrogen was produced. The plotted current values are mean values of the last 11 data points in the acquisition time of 360 s (acquisition time resolution = 0,5 s).
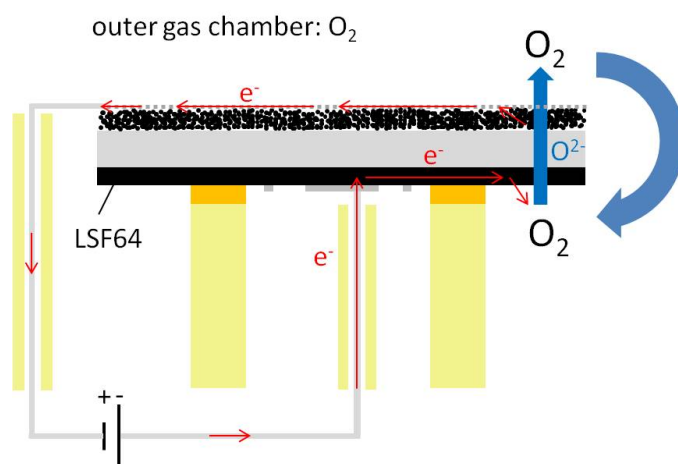
Figure 5.27: Sketch illustrating the "oxygen circling current" hypothesis. Electrons that are supplied from the power source to the WE can be transported in the LSF64 layer to the edge of the cell, that reaches out into the outer gas chamber (exaggerated in the sketch), driving oxygen pumping in the outer gas chamber, which leads to a current, but has no net effect on gas concentrations.

After removing the excess LSF64 thin film by ion etching, hydrogen could be detected with pure O_2 present in the outer gas chamber (see figure 5.28). Therefore, all following samples were subject to ion etching.

Choice of gas and flow rate in the outer gas chamber

The choice of gas and flow rate in the outer gas chamber has several effects.

- The potential drop at the counter electrode, η_{CE}, is influenced via the change of conductivity of LSCF6428 with $p(O_2)$.

- The thermodynamic cell voltage, ΔE_{Nernst}, is affected by $p(O_2)$. The oxygen flow rate in relation to the electrolysis current determines how much ΔE_{Nernst} changes during electrolysis.

- If $p(O_2)$ is higher, the amount of oxygen leaking into the inner gas chamber (see subsubsection 5.5.1) can be higher as well, leading to lower amounts of H_2 being produced.

- The $p(O_2)$ or gas flow rate of the gas in the outer gas chamber should have no effect on the quantifiability of O_2 in the outer gas chamber by means of MS. Since the MS signal is a linear or quadratic function of $p(O_2)$, the slope of the calibration curve, and therefore the LOQ, is nearly the same at all partial pressures.

  Another possibility for quantifying O_2 would be a lambda probe. However, if this sensor is used, the effect of $p(O_2)$ on the slope of the calibration curve and the LOQ must be taken into account. In case of the lambda probe the LOQ would be much lower at low $p(O_2)$ because the signal depends on the change of $\log p(O_2)$ (the order of magnitude of $p(O_2)$), which is greater if the same absolute amount of O_2 is added to a small quantity of O_2 than to a large one.

The measurement setup that is desired ensures that $\eta_{CE} \approx 0$, the contribution of $p(O_2)$ in the outer gas chamber to ΔE_{Nernst} is almost constant, and a low $p(O_2)$ is present in the inner gas chamber.
Generally, ΔE_{Nernst} is not constant due to the change of $p(H_2)$ in the inner and $p(O_2)$ in the outer gas chamber, respectively, during electrolysis. It can be calculated from the Nernst equation [61, p 221] for the overall cell reaction,

$$H_2O \rightleftharpoons H_2 + \tfrac{1}{2} O_2 \tag{5.26}$$
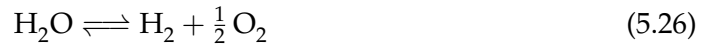
if the partial pressures of hydrogen, oxygen and water are known:

$$\Delta E_{Nernst} = \Delta E_{Nernst}^0 - \frac{RT}{4F} \ln \frac{p(H_2)p(O_2)^{1/2}}{p(H_2O)} \tag{5.27}$$

ΔE_{Nernst}^0 denotes the Nernst potential for the above reaction under standard conditions. The partial pressure of water, $p(H_2O)$, can either assumed to be constant (as a first approximation) or be calculated knowing the initial composition of the gas fed into the inner gas chamber (given in subsection 3.1.2). $p(H_2)$ and $p(O_2)$ need to be measured simultaneously, which would either require a second gas sensor (one for the outlet of

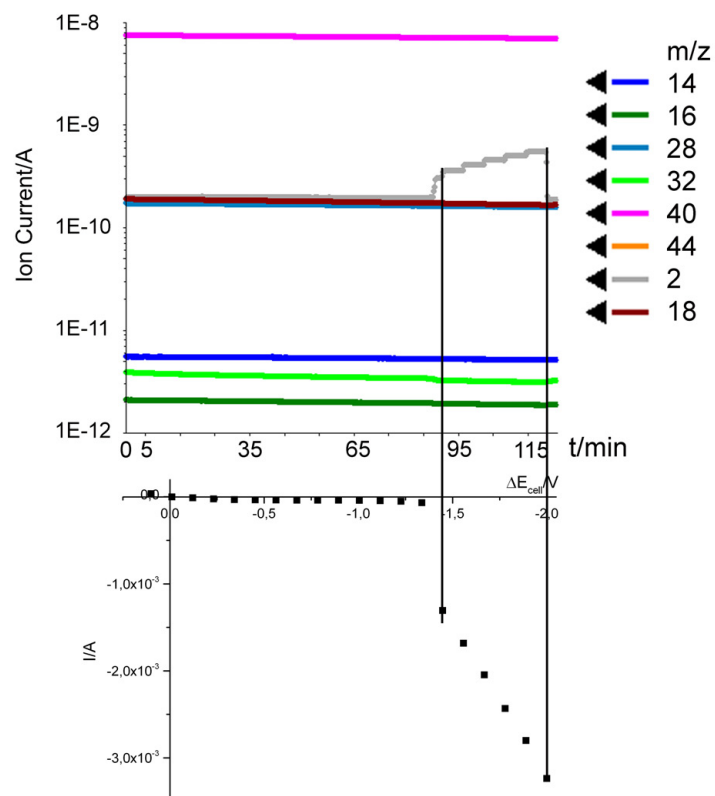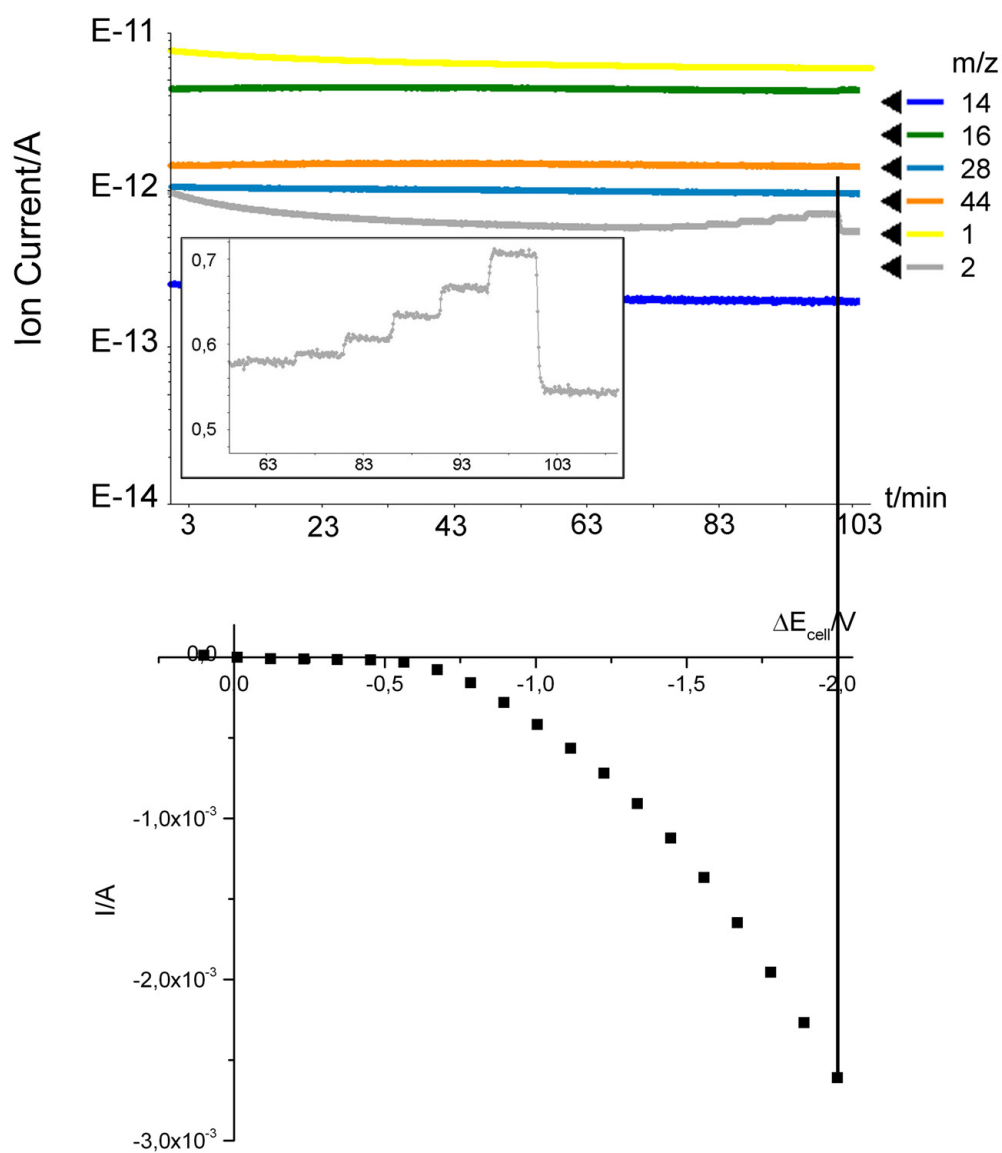*Figure 5.28:* SOEC-001 after microstructuring of the WE, with O_2 in the outer gas chamber: Current was flowing, hydrogen was produced (small steps at higher potentials; insert). The plotted current values are mean values of the last 10 current values in the acquisition time of 300 s (acquisition time resolution = 0,5 s).
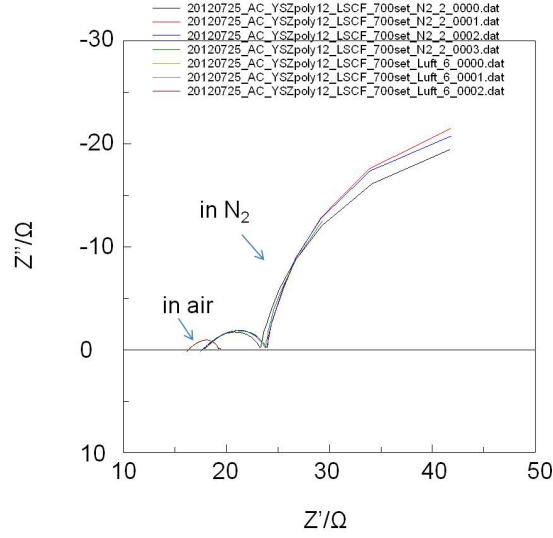
Figure 5.29: Impedance spectra of sample YSZ_poly_12_LSCF in air and N_2. The electrode impedance in N_2 roughly 20 times higher.

each gas chamber) or the need to mix the gas streams coming from the two gas chambers and feed them both into the MS. The second solution, however, would cause dilution of both gases, making amounts of gas undectable that would otherwise have been above the LOD. Therefore, it is convenient if the change of $p(O_2)$ in the outer gas chamber during electrolysis can be neglected and the contribution of $p(O_2)$ in the outer gas chamber to ΔE_{Nernst} can be assumed to be constant.

The following two paragraphs discuss the influence of different gases and flows on η_{CE}, ΔE_{Nernst}, leakage and the quantifyability of O_2 in the outer gas chamber.

Ar or N_2   The main advantage of low $p(O_2)$ in the outer gas chamber is the strongly reduced amount of O_2 possibly leaking into the inner gas chamber (only a few ppm present in Ar or N_2).
However, the resistance of LSCF6428 is much higher in low oxygen partial pressures (such as in N_2 or Ar) than in 1% oxygen or air (see figures 5.23 and 5.29). Hence, Ar or N_2 in the outer gas chamber cannot be used if η_{CE} should be negligible.

Also, ΔE_{Nernst} changes significantly in case of low $p(O_2)$ in the outer gas chamber since ΔE_{Nernst} is a function of $\log p(O_2)$ (although this effect can be mitigated by increasing the gas flow).
Another way out, that, as a "side effect" yields the amount of O_2 produced, is to measure it by means of MS or a lambda probe (low $\log p(O_2)$ - high sensitivity).

O_2   Pure oxygen is the best choice to reduce η_{CE}. In addition to this, the contribution of $p(O_2)$ in the outer gas chamber to ΔE_{Nernst} is constant. The amount of oxygen produced could not be quantified because the partial pressure is unity and does not change

by adding oxygen.

The major drawback is the strong leakage of O_2 into the inner gas chamber.

1% O_2 in N_2 A mixture of 1% O_2 in N_2 ensures that $\eta_{CE} \approx 0$ (shown in subsection 5.4.1). Also, the change in $p(O_2)$ during electrolysis alters ΔE_{Nernst} negligibly (shown in the following).

The volume percentage of oxygen in the outer gas chamber during electrolysis, $V\%(O_2, \text{elec})$, can be calculated using equation 5.5 to obtain the volume of oxygen produced per unit time, $V_{O_2, \text{prod}}/t$, and substituting it into the following equation:

$$V\%(O_2, \text{elec}) = \frac{V_{O_2, \text{prod}}/t}{V_{O_2, \text{init}}/t + V_{O_2, \text{prod}}/t} \cdot 100 + V\%(O_2, \text{init}) \tag{5.28}$$

In this equation $V_{O_2, \text{init}}/t$ denotes the gas flow rate of the oxygen-containing gas fed into the outer gas chamber and $V\%(O_2, \text{init})$ is the volume percent of oxygen in this incoming gas. The volume percentage of O_2 is identical to $p(O_2)$ for a perfect gas and a total pressure $p_{tot} = 1$ bar ($vol\% = p\%$; $p\% = p(O_2)/p_{tot}$). The corresponding change in ΔE_{Nernst} is

$$\Delta E_{Nernst, \text{elec.}} - \Delta E_{Nernst, \text{init}} = \frac{RT}{4F} \ln \frac{p(O_2)_{\text{init}}^{1/2}}{p(O_2)_{\text{elec}}^{1/2}} \tag{5.29}$$

where $\Delta E_{Nernst, \text{elec.}}$ denotes the thermodynamic cell voltage during electrolysis (at a certain current) and $\Delta E_{Nernst, \text{init}}$ is the thermodynamic cell voltage before the electrolysis starts. For a typical electrolysis experiment with a current of 11 mA, an incoming gas flow $V_{O_2, \text{init}}/t = 20$ ml min^{-1}, with a mixture of 1% O_2 supplied to the outer gas chamber, the volume percent of oxygen changes from 1 to approximately 1,21%. This leads to a change in ΔE_{Nernst} of around -2 mV. The current of 11 mA can be expected to be reached at $\eta_{WE} + \Delta E_{Nernst}$ being somewhere around 1,5 V. Therefore, it can be assumed that the contribution of $p(O_2)$ in the outer gas chamber to ΔE_{Nernst} will be almost constant, with the error being in the order of magnitude of 1 ‰ of $\eta_{WE} + \Delta E_{Nernst}$[5].
If higher accuracy is necessary or higher currents are flowing, the incoming gas flow ($V_{O_2, \text{init}}/t$) in the outer gas chamber can be increased in order to lower the error.

Using a gas mixture containing only 1% O_2 reduces $p(O_2)$ leaking into the inner gas chamber.

A quantification of produced O_2 should be possible by means of MS. In the hypothetical case of using a lambda probe, small amounts (e.g. in the beginning of the electrolysis) can probably not be detected because the change in voltage might not be distinguishable from noise.

The use of 1% O_2 in N_2 ensures that $\eta_{CE} \approx 0$ and the change of $p(O_2)$ in the outer gas chamber does not change ΔE_{Nernst} significantly. It also minimizes the amount of O_2 leaking into the inner gas chamber and consequently was the best choice for the

---

[5]As will be explained in subsection 5.5.4, η_{WE} could not be obtained due to the thermodynamic cell voltage being a mixed potential. Therefore, $\eta_{WE} + \Delta E_{Nernst}$ was the value that was related to the current and it is the error in this value that needs to be considered here.
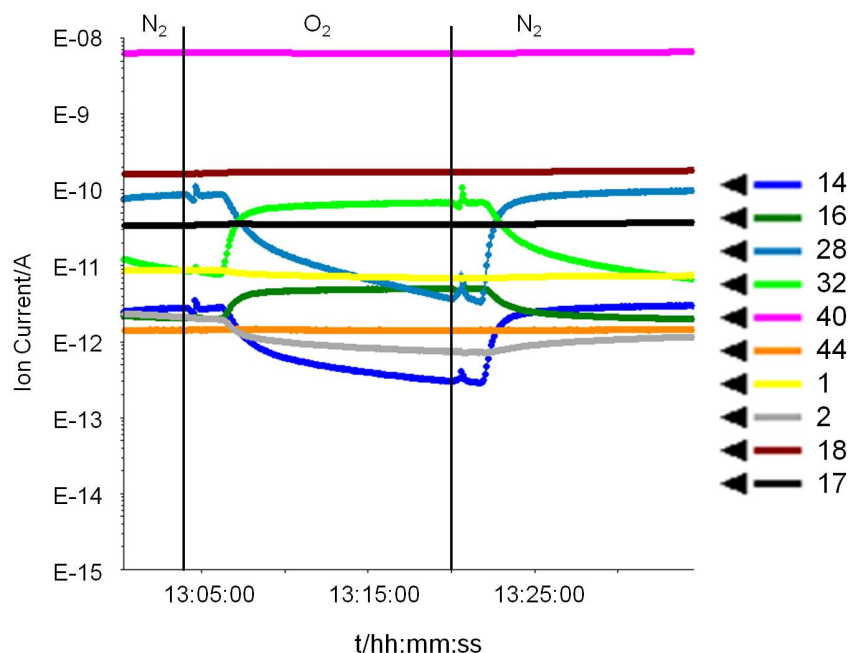
Figure 5.30: MS signals of the gas mixture in the inner gas chamber of the SOEC sample holder vs. absolute time. When the gas was changed in the outer gas chamber ($N_2 \rightarrow O_2 \rightarrow N_2$), the corresponding m/z ratios increased in the inner gas chamber, indicating a leakage of gas between inner and outer gas chamber. The black lines indicate time when the gas valve was operated. The slow response of the MS signals is because it takes some time for the gases to pass through the tubes to reach the MS.

electrolyte experiments. A quantification of O_2 is possible by MS as well, but was not carried out in this work.

SOEC sample holder leakage issues

Leakage between inner and outer gas chambers   It turned out that there was a leak between the inner and the outer gas chamber. This could be shown by recording the MS signals for hydrogen and nitrogen in the gas stream leaving the inner gas chamber and switching gases in the outer gas chamber. If the gas in the outer gas chamber was changed from N_2 to O_2, the O_2 signals ($m/z = 16$, 32) increased and the N_2 signals ($m/z = 14$, 28) decreased and vice versa (see figure figure 5.30).

Even if the sealing between inner and outer gas chambers was perfectly gas-tight, still an exchange of oxygen is conceivable. The gold sealing ring together with the electrolyte of the SOEC represent an oxygen permeation "membrane" (see figure 5.31). If $p(O_2)$ is higher in the outer gas chamber, oxygen is incorporated into YSZ at the triple phase boundary Au-YSZ-gas. It takes up electrons coming from the metal and the resulting O^{2-} ions diffuse to the TPB in the inner gas chamber, where they are oxidised. Gaseous O_2 is released into the inner gas chamber. If the system is left to itself, the oxygen permeation only ceases when the oxygen partial pressures in both gas chambers are equal.

Owing to the small TPB length, the internal resistance of the "oxygen exchange mem-
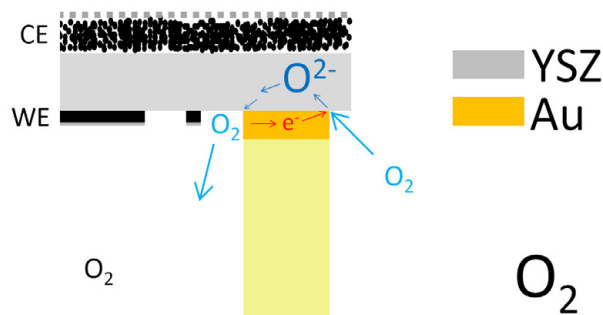
Figure 5.31: Sketch illustrating the oxygen permeation between inner and outer gas chambers in the SOEC sample holder. It is supposed that $p(O_2)$ is larger in the outer gas chamber (indicated by the huge O_2 symbol). Only half of the SOEC resting on the alumina tube is shown.

brane" is very large and the flow of oxygen leaking into the inner gas chamber can be considered to be very small. Taking into account that these small quantities of O_2 are diluted immediately by the gas flow in the inner gas chamber, the mixed potential can be expected to be close to the potential of the SOEC's LSF64 electrode.

Leakage from outer gas chamber to outside The outer alumina tube of the SOEC sample holder that covers the ensemble shown in figure 3.8 is fixed by a metal tube-shaped nut that is screwed on the sample holder, pushing a rubber sealing ring in the gap between the end of the alumina tube and the body of the sample holder. This nut needs to be screwed up unexpectedly tight in order to improve gas-thightness between the outer gas chamber and the surrounding air (see figure 5.32).

5.5.2 Measurement of open circuit voltage

It was tried to measure the open circuit voltage across an SOEC on different samples with moistened Ar in the inner gas chamber and Ar or 1% O_2 in N_2 in the outer gas chamber at around 650°C, using a Keithley 2000 digital voltmeter and Hewlett Packard 34401A voltmeter. In every of the four measurements on three different samples (SOEC-003, SOEC-004 and SOEC-005), the voltage values fluctuated and no constant open circuit voltage could be measured.

5.5.3 AC measurements

The EIS measurements on the SOEC samples were performed to obtain the electrolyte resistance $R_{electrolyte}$. Even though an SOEC acts as a voltage source if two different $p(O_2)$ are present in the two gas chambers, the determination of the YSZ resistance is possible and meaningful because it is ohmic (i.e. independent of cell voltage) [101, p 93].
In analogy to the argument in 5.4.1, the offset on the x-axis in the impedance spectrum was interpreted as $R_{electrolyte}$.
For SOEC-004, $R_{electrolyte}$ was found to be 96,6 Ω at 638,19°C (mean value of three measurements), for SOEC-005 it was 47,1 Ω at 647,8°C (mean value of six measurements).

Figure 5.32: The MS signals for N_2 an O_2 in the outer gas chamber decreased dramatically (up to one order of magnitude) after screwing up the nut really tight.

(a)

(b)

Figure 5.33: Impedance spectra of SOECs-004 (a) and 005 (b). The x-axis offset represents the electrolyte resistance.

5.5.4 DC measurements with detection of hydrogen

Calibration   Table 5.7 contains the calibration data for hydrogen and oxygen used to evaluate the electrolysis experiments (calibration curves for H_2 with new blank value, see subsubsection 5.2.3).

Table 5.7: MS calibration data for samples SOEC-004 and SOEC-005. For the oxygen calibration data see table 5.5, page 63 (calibrations 22/10/2012 and 25/10/2012), and table 5.3, page 60 (LODs and LOQs). S denotes the ion current/A and x is the volume fraction of H_2.

	SOEC-004	SOEC-005
date of calibration H_2	03/09/2012 (cf. fig. 5.13, page 62)	22/10/2012 (cf. fig. 5.14, page 62)
date of calibration O_2	03/09/2012	25/10/2012 (cf. fig. 5.14, page 62)
date of blank value	28/08/2012	24/10/2012
calibration function H_2	$S = 7.07 \times 10^{-8}x + 4.37 \times 10^{-11}$	$S = 7.25 \times 10^{-8}x + 1.34 \times 10^{-11}$
LOD H_2/ppm	11,30	0,73
LOQ H_2/ppm	37,65	2,45

The measured potential   Figure 5.34 shows current-voltage curves for samples SOEC-004 and SOEC-005. Since the surface area of the LSF64 thin film electrode was known, current densities are plotted. The potential E_{LSF} is the sum of η_{WE} and ΔE_{Nernst}. Due to an O_2 leakage, ΔE_{Nernst} is not defined in this case. Rather, a mixed potential exists, which is determined by the kinetics of the oxygen incorporation reactions from water and oxygen gas,

$$H_2O + 2\,e^- \rightleftharpoons O^{2-}_{LSF} + H_2 \tag{5.30}$$

and

$$O_2 + 4\,e^- \rightleftharpoons 2\,O^{2-}_{LSF} \tag{5.31}$$
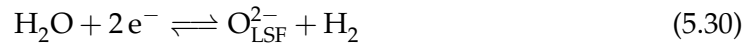
Therefore, ΔE_{Nernst} cannot be calculated from the concentrations of the gases taking part in the above reactions and will only be called ΔE_{OCV} in the following. The overpotential at the working electrode, η_{WE} is also a "mixed overpotential".

Evaluation using Faraday's law   Figure 5.35 shows the MS signals recorded during an electrolyis experiment. It can be cleary seen that the hydrogen concentration increases stepwise, corresponding to the cathodic potential applied to the LSF64 electrode. Likewise, the oxygen concentration decreases in response to the applied potential. Even without a quantitative evaluation, this shows that the model-type SOEC built in this work is capable of splitting water - more hydrogen is produced if a lower cathodic potential is applied to the WE.

For the quantitative evaluation, the following two effects have to be considered apart from the leakage. Before starting the electrolysis experiment, the MS signals were constant. After the electrolysis had finished, the gas mixture had the same composition as before the experiment. The MS signals, however, did not go back their initial values in about 20 minutes. This indicates that also during the experiment, the signals do not exactly reflect the actual gas composition.
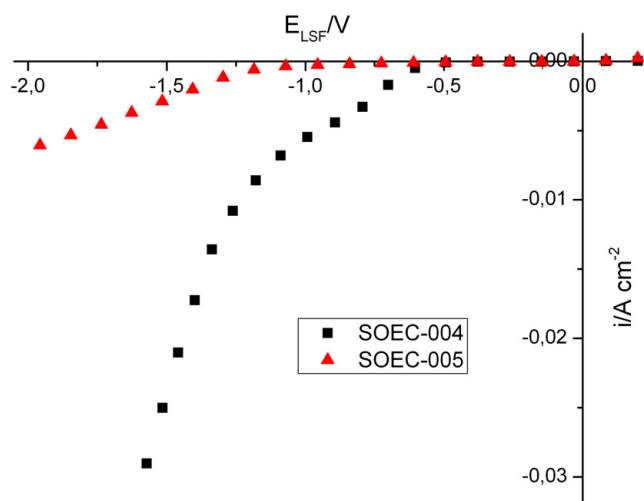
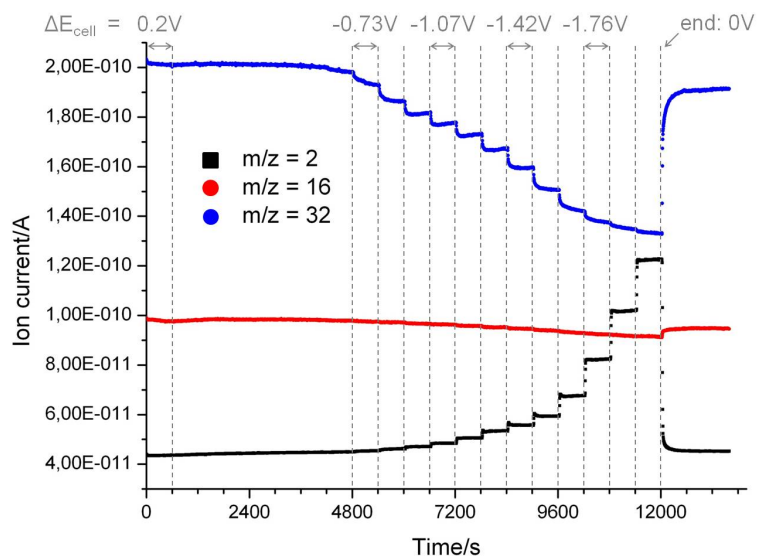*Figure 5.34:* Current-voltage curves of samples SOECs-004 and 005.

Figure 5.35: MS signals as a function of electrolysing time on sample SOEC-004. The signals corresponding to O_2 ($m/z = 16, 32$) decrease, the $m/z = 2$ signal associated with H_2 increases if a cathodic potential is applied to the LSF64 electrode. The voltage was changed by ≈ 11 mV every 10 min.
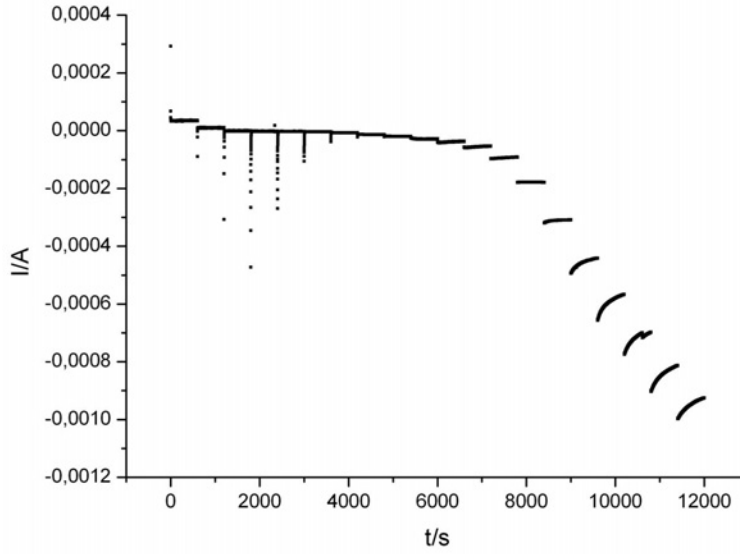
Figure 5.36: Current vs. time curve for SOEC-005.

When choosing the acquisition time, a compromise needed to be made between a steady-state current and electrode degradation. The DC measurements performed on the LSF64-YSZ-LSF64 samples (subsection 5.3.2) showed that even after very long acquisition times (e.g. 5850 s) no constant current was reached. This effect was more pronounced for shorter acquisition times, but the acquisition time cannot be chosen arbitrarily long in order to make the current as constant as possible, because the cathode material degrades (see subsubsection 5.3.2). This would compromise the intention of recording a stationary current-voltage curve as a measurement that is characteristic for the material. Therefore, an acquisition time of 600 s was chosen. However, a current changing with time can also have an impact on the quantitative evaluation using Faraday's law. Since the gas mixture needs some time to flow from the sample holder to the MS, a change in gas composition is not immediately detected by the MS. As a consequence, the electrically measured current at time t might not exactly correspond to the current calculated from the gas composition via Faraday's law at the same time t.
An example for an I vs. t curve (SOEC-005) is shown in figure 5.36.

Figure 5.37 shows current-voltage curves for sample SOEC-004 (top) and the volume fraction of hydrogen and oxygen in the inner gas chamber as a function of E_{LSF} (bottom). The oxygen curve was evaluated using the O_2 calibration via the $m/z = 16$ signal (indicated by an asterisk). Figure 5.38 is similar to fig. 5.37 but the oxygen fraction was calculated using the $m/z = 32$ signal (denoted by two asterisks). Figures 5.39 and 5.40 are analogous plots for SOEC-005.
From the bottom plots in figures 5.37, 5.38, 5.39 and 5.40 it can be seen that H_2 is produced and O_2 is consumed during electrolysis. The top plots in these figures show the electrically measured current-voltage curve as well as the curves calculated from the fluxes of hydrogen and oxygen. The latter two currents were calculated from the

Figure 5.37: Current-voltage curves and gas concentrations-voltage curves for SOEC-004 (Vol-% O$_2$ obtained from $m/z = 16$).

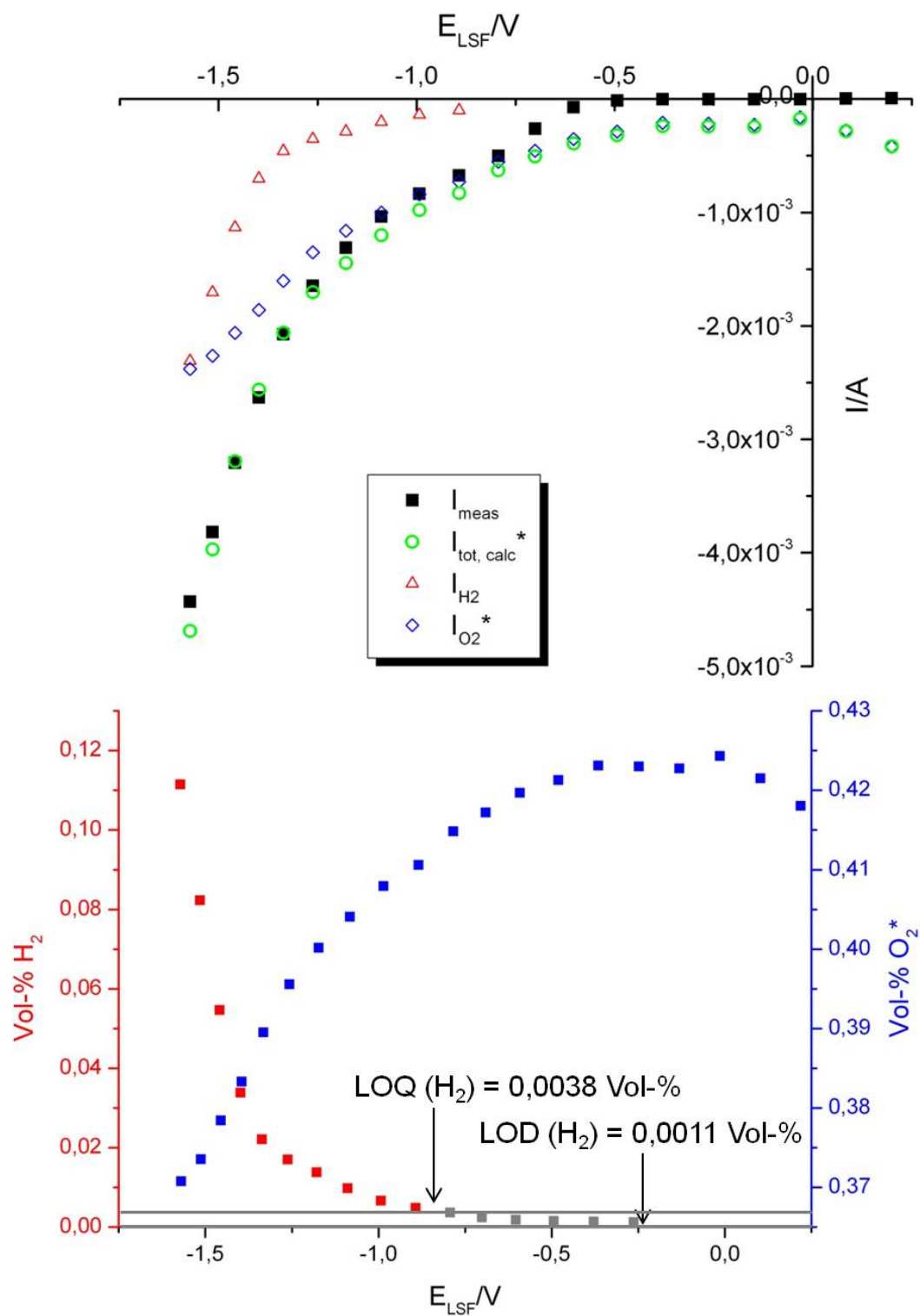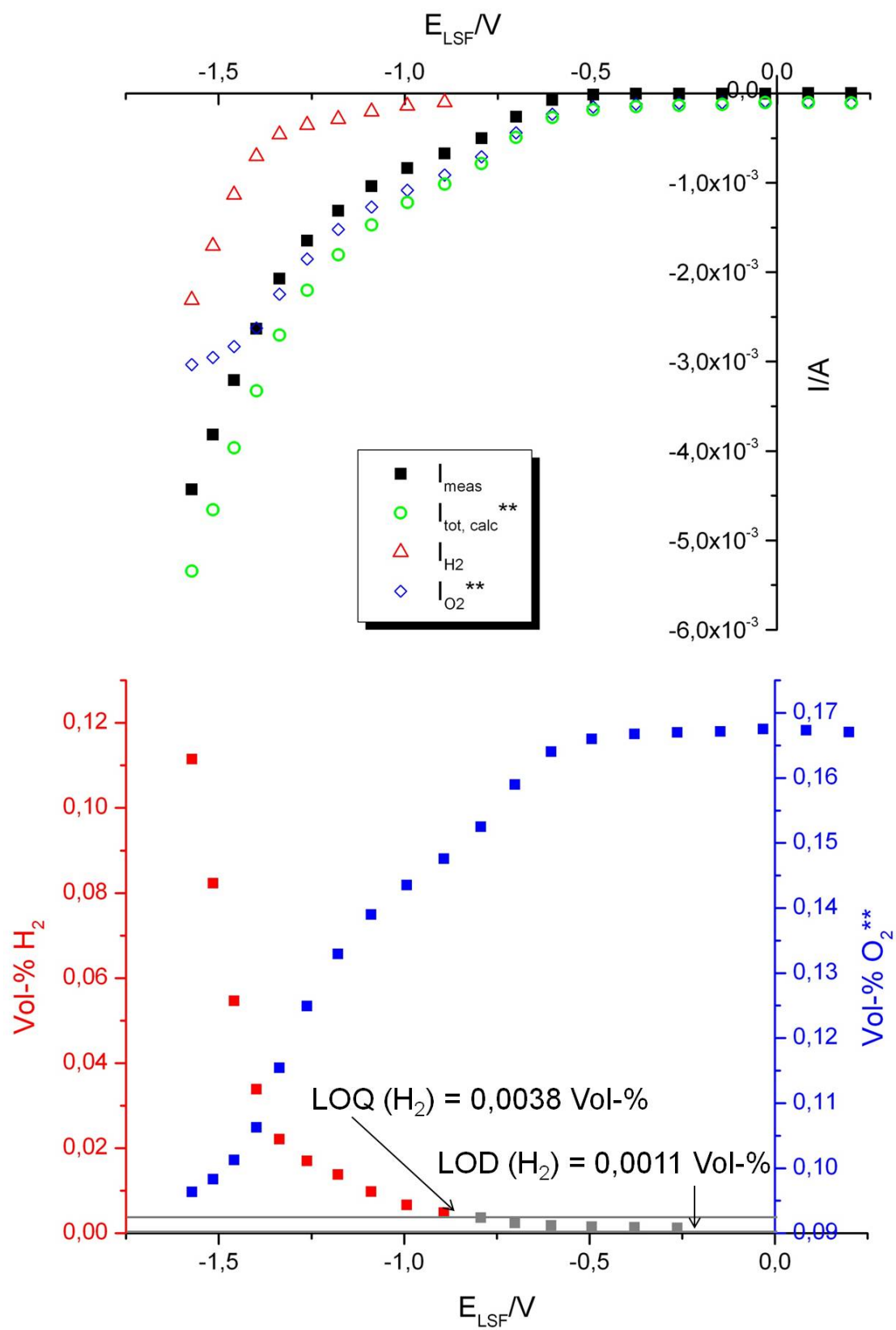*Figure 5.38:* Current-voltage curves and gas concentrations-voltage curves for SOEC-004 (Vol-% O_2 obtained from $m/z = 32$).
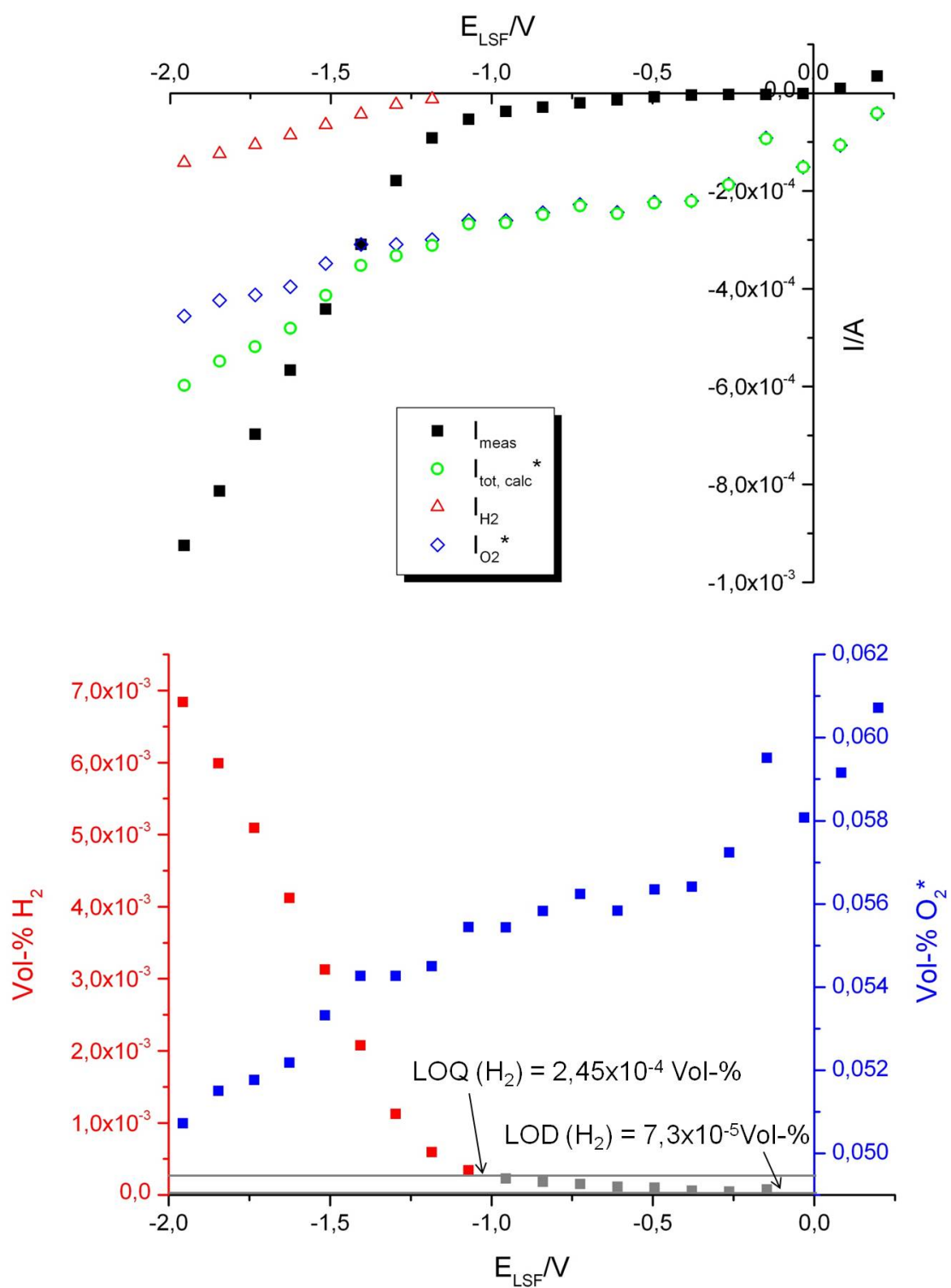
Figure 5.39: Current-voltage curves and gas concentrations-voltage curves for SOEC-005 (Vol-% O_2 obtained from $m/z = 16$).
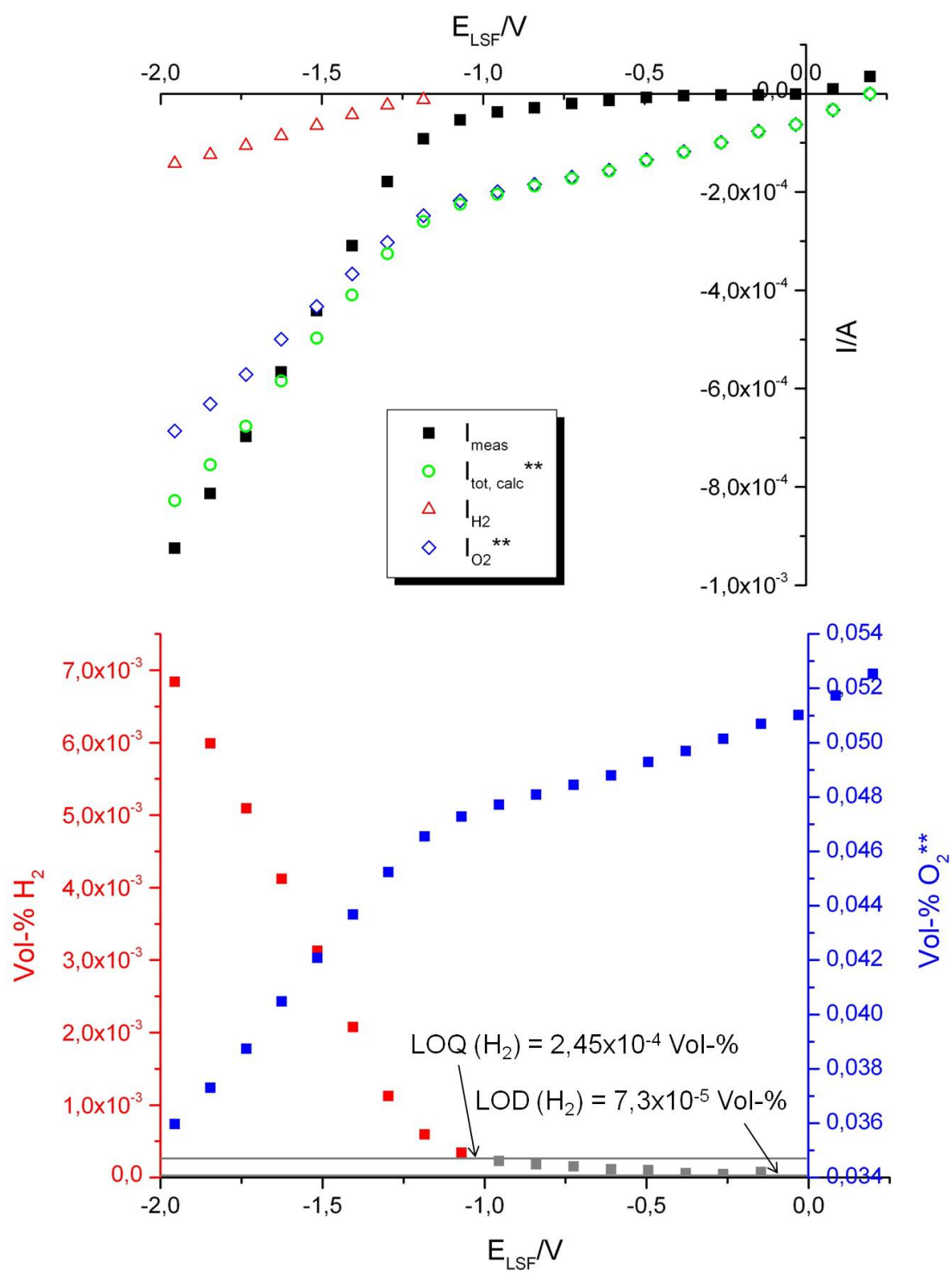
Figure 5.40: Current-voltage curves and gas concentrations-voltage curves for SOEC-005 (Vol-% O_2 obtained from $m/z = 32$).

following equations (Faraday's law):

$$I_{H_2} = \frac{x(H_2) \cdot \text{carrier gas flow} \cdot 2F \cdot p}{RT} \qquad (5.32)$$

and

$$I_{O_2} = -\frac{(x(O_2) - x(O_2, \text{init.})) \cdot \text{carrier gas flow} \cdot 2F \cdot p}{RT} \qquad (5.33)$$

In equation 5.33, $x(O_2, \text{init.})$ is the volume fraction of O_2 present before the electrolysis started. It can be observed that I_{O_2} does not vanish at $E_{LSF} = 0$. This is because the MS signals for $m/z = 16, 32$ at $E_{LSF} = 0$ (i.e. the third potential step) differed from those before the electrolysis was started and from which $x(O_2, \text{init.})$ was calculated. The gas composition is the same but as mentioned above and in subsubsection 5.2.3, the MS signals seem to change slightly nonetheless.

Despite the sample holder leakage issues, drifting MS signals and constraints in acquisition time, the sum of the two calculated currents ($I_{\text{tot, calc}} = I_{H_2} + I_{O_2}$, shown as green circles in figs. 5.37, 5.38, 5.39 and 5.40) is in good agreement with the measured current-voltage curve. Not only a qualitative demonstration of the SOEC's function could be provided, but a semi-quantitative evaluation using Faraday's law is possible. This represents a next step in the characterisation of LSF64 as a potential electrode material for elecrolysis with solid oxide cell.

Potential threshold Furthermore, as assumed in subsubsection 2.2.2, no potential threshold for the generation of H_2 can be observed.

When electrolysing liquid water, hydrogen and oxygen usually evolve as pure substances at a pressure of 1 bar. The corresponding "threshold potential" is, according to reaction 5.26 and the Nernst equation (ΔE^0 is the standard potential for the electrolysis of water):

$$\Delta E_{\text{cell}} = \Delta E^0 - \frac{RT}{2F} \ln \frac{p(H_2)p(O_2)^{1/2}}{a(H_2O)} = \Delta E^0 = -1,23 \text{ V} \qquad (5.34)$$

The activity of water can be set to 1 since it is constant and is incorporated into ΔE^0. The potential threshold results from the fact that the partial pressures, at which the gases are "allowed" to evolve, are fixed by the experimental conditions (liquid water - hydrostatic pressure)[6]. The corresponding voltage at the operating temperature of sample SOEC-004 is the standard potential at 639°C, $\Delta E^0_{639°C}$:

$$\Delta E_{\text{cell, 639°C}} = \Delta E^0_{639°C} - \frac{RT}{zF} \ln 1 = \Delta E^0_{639°C} = -\frac{-\Delta_f G^0_{639°C}(H_2O)}{2F} \approx -1,02 \text{ V} \quad (5.35)$$

The free enthalpy of formation of water was interpolated from values taken from reference [98]. In the case of the SOEC, partial pressures of hydrogen and oxygen below 1 bar can be realized by a steady state electrolysis current (see figures 5.37, 5.38. In terms of potential, this means that the corresponding Nernst potential is more positive than -1,02 V. For instance, just above the LOQ of H_2, the partial pressures were $p(H_2 = 4.8 \times 10^{-5}$ bar, $p(H_2O) \approx 2.6 \times 10^{-2}$ bar (assuming $p(H_2O)$ to be constant) and $p(O_2) = 1 \times 10^{-2}$ bar, which gives a Nernst potential of about -0,59 V.

---

[6]Of course, lower hydrogen and oxygen partial pressures can be achieved in liquid electrochemistry, e.g. by purging the solution with inert gas, but let's take a typical liquid phase electrolysis experiment, i.e. two electrodes in water + potential applied, as an example here.

To sum up, the presence of hydrogen at partial pressures significantly below 1 bar together with the corresponding Nernst potential indicate that there is no potential threshold in high temperature electrolysis.

6 Conclusions and outlook

A model-type SOEC with a $La_{0.6}Sr_{0.4}FeO_{3-\delta}$ (LSF64) cathode was built and a setup that allows electrochemical measurements and simultaneous detection of produced gases was tested (SOEC sample holder + mass spectrometer (MS)).

The potential difference ΔE_{cell} of the SOEC is the sum of potential drops $\eta_i = IR_i$ at different components of the cell plus the thermodynamic cell voltage ΔE_{Nernst}:

$$\Delta E_{cell} = IR_{CE} + IR_{electrolyte} + IR_{WE} + \Delta E_{Nernst}$$

The electrolyte contribution $IR_{electrolyte}$ was measured by electrochemical impedance spectroscopy and subsequently subtracted from ΔE_{cell}. The potential drop at the porous counter electrode, IR_{CE}, was shown to be negligible and thus the quantities of interest, η_{WE} and ΔE_{Nernst}, become determinable. The overpotential η_{WE} describes the kinetics of water splitting on LSF64. Generally, ΔE_{Nernst} varies as a function of the gas concentrations and as a consequence depends on the solid state setup. The gas concentrations can actually change with different ΔE_{cell} applied. This was found to be in contrast to a classic liquid electrochemistry setup where $p(H_2)$ and $p(O_2)$ are usually around atmospheric pressure, which leads to a "threshold potential" at 1,23 V. Indeed, no "threshold potential" was observed in the experiments. However, as a consequence of leakage, a separation of η_{WE} and ΔE_{Nernst} was not possible in this study.

Model-type LSF64-YSZ-LSCF6428 SOECs could be successfully prepared by pulsed laser deposition of LSF64 and subsequent microstructuring by means of photolithography and ion etching. In contrast to a porous material, the well-defined cathode geometry allows the calculation of current densities and hence facilitates comparison with other materials. The counter electrode consisted of porous $La_{0.6}Sr_{0.4}Co_{0.2}Fe_{0.8}O_{3-\delta}$ (LSCF6428).

Coupling the commercial SOFC sample holder "ProboStat" to an electron ionization quadrupole MS suited for gas analysis was proven to be a viable solution for the characterization of thin film model electrodes. Quantifying hydrogen and oxygen via the MS signals was found to be possible but the signals seem to show a drift that is not understood yet. Owing to the presence of a second redox couple, ΔE_{Nernst} turned into a mixed potential. Different gas mixtures in the outer gas chamber were tested in order to realize $\eta_{CE} \approx 0$, to keep the contribution of the produced oxygen to the open-circuit voltage negligible and to minimize the loss of produced H_2 by reaction with oxygen streaming into the inner gas chamber, all at the same time. It was found that 1% O_2 in N_2 best suited these requirements.

The H_2 and O_2 concentrations were quantified for different cell voltages and the electrolyis currents corresponding to the gas fluxes were calculated by Faraday's law. Despite the difficulties of the experimental setup, these Faraday currents are in good agreement with the measured electrical current.

For further experiments, the calibrations of the mass flow controllers need to be checked with respect to a more reliable reference, since they are the basis of the MS calibration. Using MFCs with low flow rates ($\approx$ 1 ml/min), the MS could be calibrated while letting the gases flow through the SOEC sample holder. This makes the measurement and calibration situation more alike. Alternatively, a calibration by standard addition (for a few points in the current-voltage curve) can be considered.

By polishing the inner tube of the SOEC sample holder, better gas-tightness might be achieved. The leakage of O_2 from the outer into the inner gas chamber could also be reduced by using e.g. pure Ar in the outer gas chamber. Because of η_{CE} being no longer negligible, η_{WE} could then be measured vs. a reference electrode next to the WE (e.g. the ring around the microstructured LSF64 electrode).

Measurements on LSF64 electrodes with a metal grid *beneath* LSF64 could be compared to the measurements done in this work.

Finally, other electrode materials (e.g. other perovskites) and other reactant gases (e.g. CO_2, CO_2+H_2O) should be investigated.

7 Acknowledgements

I would like to thank Jürgen Fleig for the opportunity to do this master's thesis, his support, and the chance to participate in the "Electrochemistry 2012" conference.

Furthermore, I would like to thank Alexander Opitz for his support in ... basically everything (the list would require another appendix).

I would also like to express my thanks towards Sandra Kogler for introducing me to the operation of many machines and her advice on everything concerning "her" material, LSF64.

Likewise, I want to acknowledge the work of Alexander Hutterer and Vincent Moraes who found the right preparation procedure for low-resistance LSCF6428 electrodes during their bachelor's theses.

Special thanks go to my fellow detectives Christoph Ahamer and Sebastian Köck who not only contributed to, but basically are at the origin of an extremely pleasant working atmosphere in our office.

For the relaxing working atmosphere outside our office I want to thank all the pirates (☠), viz. Alex, Andreas, Andreas, Bernhard, Christoph, Christoph, Dominik, Edvinas, Gerald, Hinnerk, Lukas, Markus, Mr. Snoot, Tobias, Sandra, Sebastian, Steffi and Tschisi, as well as Udo and Kurt for their support in gas and administrative issues, respectively.

Also, I would like to thank Elisabeth Maurer for a sample of a screen for screen-printing, that I tried out but didn't use in the end.

Finally I would like to thank my parents for their support throughout my studies.

\end{document}

Bibliography

[1]   Verne, J., *The Mysterious Island*; Heritage Press: 1959.

[2]   `http://www.jules-verne.net/jules-verne-bibliographie.html` (accessed 24/01/2013).

[3]   *Report of the World Commission on Environment and Development*; tech. rep.; United Nations, 1987.

[4]   Kyoto Protocol to the United Nations Framework Convention on Climate Change., 1998.

[5]   *Key World Energy Statistics 2011*; tech. rep.; International Energy Agency, 2011.

[6]   IPCC *Summary for Policymakers*; tech. rep.; 2007.

[7]   Hauch, A.; Ebbesen, S. D.; Jensen, S. H.; Mogensen, M. Highly efficient high temperature electrolysis. *Journal of Materials Chemistry* **2008**, *18*, 2331–2340.

[8]   Dönitz, W.; Erdle, E.; Streicher, R. In *Electrochemical Hydrogen Technologies*, Wendt, H., Ed.; Elsevier: Amsterdam - Oxford - New York - Tokyo, 1990; Chapter 3.

[9]   Vielstich, W. In *Handbook of Fuel Cells*, Vielstich, W., Gasteiger, H. A., Lamm, A., Yokokawa, H., Eds.; John Wiley + Sons: 2010.

[10]   Stoots, C. M.; O'Brien, J. E.; Condie, K. G.; Hartvigsen, J. J. High-temperature electrolysis for large-scale hydrogen production from nuclear energy – Experimental investigations. *International Journal of Hydrogen Energy* **2010**, *35*, 4861–4870.

[11]   *Nuclear Hydrogen R+D Plan*; tech. rep.; U.S. Department of Energy, Office of Nuclear Energy, Science and Techology, 2004.

[12]   Laguna-Bercero, M. A. Recent advances in high temperature electrolysis using solid oxide fuel cells: A review. *Journal of Power Sources* **2012**, *203*, 4–16.

[13]   Oldham, K. B.; Myland, J. C.; Bond, A. M. Electrochemical science and technology: fundamentals and applications., 2012.

[14]   Trasatti, S. Water electrolysis: who first? *Journal of Electroanalytical Chemistry* **1999**, *476*, 90–91.

[15]   Russell, C. Enterprise and electrolysis... *Chemistry in Britain* **2003**.

[16]   Smolinka, T. Wasserstoff aus Elektrolyse – ein technologischer Vergleich der alkalischen und PEM-Wasserelektrolyse., `http://www.fvee.de/fileadmin/publikationen/Workshopbaende/ws2007/ws2007_07.pdf` (accessed 29/09/2012).

[17]   Faraday, M. Experimental Researches in Electricity. Seventh Series. *Philosophical Transactions of the Royal Society of London* **1834**, *124*, 77–122.

[18]   Holladay, J. D.; Hu, J.; King, D. L.; Wang, Y. An overview of hydrogen production technologies. *Catalysis Today* **2009**, *139*, 244–260.

[19] Fuel Cell Store - Hydrogen Electrolyzer Products, High Purity Hydrogen Generator, Production Units., `http://www.fuelcellstore.com/en/pc/viewCategories.asp?idCategory=60` (accessed 29/09/2012).

[20] RelHy., `www.relhy.eu` (accessed 03/10/2012).

[21] Fuel Cell and Hydrogen Joint Undertaking., `http://www.fch-ju.eu/` (accessed 03/10/2012).

[22] Spacil, H. S.; Tedmon, C. S. Electrochemical Dissociation of Water Vapor in Solid Oxide Electrolyte Cells. *Journal of The Electrochemical Society* **1969**, *116*, 1627–1633.

[23] Isenberg, A. O. Energy conversion via solid oxide electrolyte electrochemical cells at high temperatures. *Solid State Ionics* **1981**, *3–4*, 431–437.

[24] Dönitz, W.; Erdle, E. High-temperature electrolysis of water vapor—status of development and perspectives for application. *International Journal of Hydrogen Energy* **1985**, *10*, 291–295.

[25] Iwahara, H.; Esaka, T.; Uchida, H.; Yamauchi, T.; Ogaki, K. High temperature type protonic conductor based on $SrCeO_3$ and its application to the extraction of hydrogen gas. *Solid State Ionics* **1986**, *18–19, Part 2*, 1003–1007.

[26] Maskalick, N. J. High temperature electrolysis cell performance characterization. *International Journal of Hydrogen Energy* **1986**, *11*, 563–570.

[27] Eguchi, K.; Hatagishi, T.; Arai, H. Power generation and steam electrolysis characteristics of an electrochemical cell with a zirconia- or ceria-based electrolyte. *Solid State Ionics* **1996**, *86–88, Part 2*, 1245–1249.

[28] Momma, A.; Kato, T.; Kaga, Y.; Nagata, S. Polarization behavior of high temperature solid oxide electrolysis cells (SOEC). *Nippon Seramikkusu Kyokai Gakujutsu Ronbunshi/Journal of the Ceramic Society of Japan* **1997**, *105*, 369–373.

[29] Kobayashi, T.; Abe, K.; Ukyo, Y.; Matsumoto, H. Study on current efficiency of steam electrolysis using a partial protonic conductor $SrZr_{0.9}Yb_{0.1}O_{3-\alpha}$. *Solid State Ionics* **2001**, *138*, 243–251.

[30] Uchida, H.; Osada, N.; Watanabe, M. High-performance electrode for steam electrolysis: Mixed conducting ceria-based cathode with highly-dispersed Ni electrocatalysts. *Electrochemical and Solid-State Letters* **2004**, *7*, A500–A502.

[31] O'Brien, J. E.; Stoots, C. M.; Herring, J. S.; Lessing, P. A.; Hartvigsen, J. J.; Elangovan, S. Performance Measurements of Solid-Oxide Electrolysis Cells for Hydrogen Production. *Journal of Fuel Cell Science and Technology* **2005**, *2*, 156–163.

[32] Hauch, A.; Jensen, S. H.; Ramousse, S.; Mogensen, M. Performance and durability of solid oxide electrolysis cells. *Journal of The Electrochemical Society* **2006**, *153*, A1741–A1747.

[33] Herring, J. S.; O'Brien, J. E.; Stoots, C. M.; Hawkes, G. L.; Hartvigsen, J. J.; Shahnam, M. Progress in high-temperature electrolysis for hydrogen production using planar SOFC technology. *International Journal of Hydrogen Energy* **2007**, *32*, 440–450.

[34] Marina, O. A.; Pederson, L. R.; Williams, M. C.; Coffey, G. W.; Meinhardt, K. D.; Nguyen, C. D.; Thomsen, E. C. Electrode Performance in Reversible Solid Oxide Fuel Cells. *Journal of The Electrochemical Society* **2007**, *154*, B452–B459.

[35] Brisse, A.; Schefold, J.; Zahid, M. High temperature water electrolysis in solid oxide cells. *International Journal of Hydrogen Energy* **2008**, *33*, 5375–5382.

[36] Yang, X.; Irvine, J. T. S. $(La_{0.75}Sr_{0.25})_{0.95}Mn_{0.5}Cr_{0.5}O_3$ as the cathode of solid oxide electrolysis cells for high temperature hydrogen production from steam. *Journal of Materials Chemistry* **2008**, *18*, 2349–2354.

[37] Chauveau, F.; Mougin, J.; Bassat, J. M.; Mauvy, F.; Grenier, J. C. A new anode material for solid oxide electrolyser: The neodymium nickelate $Nd_2NiO_{4+\delta}$. *Journal of Power Sources* **2010**, *195*, 744–749.

[38] Schiller, G.; Ansar, A.; Lang, M.; Patz, O. High temperature water electrolysis using metal supported solid oxide electrolyser cells (SOEC). *Journal of Applied Electrochemistry* **2009**, *39*, 293–301.

[39] Stoots, C. M.; Condie, K. G.; O'Brien, J. E.; Herring, J. S.; Hartvigsen, J. J. Test Results From the Idaho National Laboratory 15kW High Temperature Electrolysis Test Facility. *ASME Conference Proceedings* **2009**, *2009*, 831–841.

[40] Ouweltjes, J. P.; Berkeveld, L.; Rietveld, B. In *18th World Hydrogen Energy Conference 2010 - WHEC 2010*, Detlef Stolten Thomas Grube.

[41] Kim, S.; Yu, J.; Seo, D.; Han, I.; Woo, S. Hydrogen Production by High Temperature Electrolysis Using Solid Oxide Electrolyzer Cells. *ECS Transactions* **2011**, *35*, 2957–2960.

[42] Minh, N. Q. Development of Reversible Solid Oxide Fuel Cells (RSOFCs)and Stacks. *ECS Transactions* **2011**, *35*, 2897–2904.

[43] Li, S.; Li, Y.; Gan, Y.; Xie, K.; Meng, G. Electrolysis of H_2O and CO_2 in an oxygenion conducting solid oxide electrolyzer with a $La_{0.2}Sr_{0.8}TiO_{3+\delta}$ composite cathode. *Journal of Power Sources* **2012**, *218*, 244–249.

[44] Matsui, T.; Kishida, R.; Kim, J.-Y.; Muroyama, H.; Eguchi, K. Performance Deterioration of Ni–YSZ Anode Induced by Electrochemically Generated Steam in Solid Oxide Fuel Cells. *Journal of The Electrochemical Society* **2010**, *157*, B776–B781.

[45] Hauch, A.; Ebbesen, S. D.; Jensen, S. H.; Mogensen, M. Solid Oxide Electrolysis Cells: Microstructure and Degradation of the Ni/Yttria-Stabilized Zirconia Electrode. *Journal of The Electrochemical Society* **2008**, *155*, B1184–B1193.

[46] Kuhn, M.; Hashimoto, S.; Sato, K.; Yashiro, K.; Mizusaki, J. Oxygen nonstoichiometry, thermo-chemical stability and lattice expansion of $La_{0.6}Sr_{0.4}FeO_{3-\delta}$. *Solid State Ionics* **2011**, *195*, 7–15.

[47] Kogler, S. Electrode kinetics of (La,Sr)FeO_3 in H_2/H_2O and O_2 containing atmospheres. *Lecture no. O 016 at the "Electrochemistry 2012" conference* **2012**.

[48] Riedel, E., *Anorganische Chemie*, 6th ed.; Walter De Gruyter: 2004.

[49] West, A. R., *Basic Solid State Chemistry*; John Wiley + Sons: Chichester, New York, Brisbane, Toronto, Singapore, 1988.

[50] Mogensen, M.; Sammes, N. M.; Tompsett, G. A. Physical, chemical and electrochemical properties of pure and doped ceria. *Solid State Ionics* **2000**, *129*, 63–94.

[51] Holleman, A.; Wiberg, N., *Lehrbuch der Anorganischen Chemie*, 102nd ed.; Walter de Gruyter: 2007.

[52] Müller, U., *Anorganische Strukturchemie*, 6th ed.; Vieweg+Teubner: Wiesbaden, 2008.

[53] `http://www.chemexplore.net/ReO3-NiO.htm` (accessed 04/11/2012).

[54] `http://www.seas.upenn.edu/~chem101/sschem/ionicsolids.html` (accessed 29/10/2012).

[55] `http://en.wikipedia.org/wiki/File:CaF2_polyhedra.png` (accessed 29/10/2012).

[56] Mizusaki, J.; Yoshihiro, M.; Yamauchi, S.; Fueki, K. Nonstoichiometry and defect structure of the perovskite-type oxides $La_{1-x}Sr_xFeO_{3-\delta}$. *Journal of Solid State Chemistry* **1985**, *58*, 257–266.

[57] Søgaard, M.; Vang Hendriksen, P.; Mogensen, M. Oxygen nonstoichiometry and transport properties of strontium substituted lanthanum ferrite. *Journal of Solid State Chemistry* **2007**, *180*, 1489–1503.

[58] Patrakeev, M. V.; Bahteeva, J. A.; Mitberg, E. B.; Leonidov, I. A.; Kozhevnikov, V. L.; Poeppelmeier, K. R. Electron/hole and ion transport in $La_{1-x}Sr_xFeO_{3-\delta}$. *Journal of Solid State Chemistry* **2003**, *172*, 219–231.

[59] Fossdal, A.; Menon, M.; Waernhus, I.; Wiik, K.; Einarsrud, M.-A.; Grande, T. Crystal Structure and Thermal Expansion of $La_{1-x}Sr_xFeO_{3-\delta}$ Materials. *Journal of the American Ceramic Society* **2004**, *87*, 1952–1958.

[60] Dann, S. E.; Currie, D. B.; Weller, M. T.; Thomas, M. F.; Al-Rawwas, A. D. The Effect of Oxygen Stoichiometry on Phase Relations and Structure in the System $La_{1-x}Sr_xFeO_{3-\delta}$ ($0 \leq x \leq 1, 0 \leq \delta \leq 0.5$). *Journal of Solid State Chemistry* **1994**, *109*, 134–144.

[61] Atkins, P.; Paula, J. d., *Physical Chemistry*; Oxford University Press: Great Britain, 2006; Vol. 8.

[62] Orlovskaya, N.; Browning, N.; Nicholls, A. Ferroelasticity in mixed conducting $LaCoO_3$ based perovskites: a ferroelastic phase transition. *Acta Materialia* **2003**, *51*, 5063–5071.

[63] Leonidov, I. A.; Kozhevnikov, V. L.; Patrakeev, M. V.; Mitberg, E. B.; Poeppelmeier, K. R. High-temperature electrical conductivity of $Sr_{0.7}La_{0.3}FeO_{3-\delta}$. *Solid State Ionics* **2001**, *144*, 361–369.

[64] Skoog, D. A.; Holler, J. F.; Crouch, S. R., *Principles of Instrumental Analysis*, 6th ed.; David Harris: 2007.

[65] Camman, K., *Instrumentelle Analytische Chemie*; Spektrum: 2001.

[66] Rizzi, A. Vorlesungsskriptum VO Analytische Chemie III - Massenspektrometrie I (Universität Wien, VO-Nr. 270110, WS 2006)., 2006.

[67] Dass, C., *Fundamentals of Contemporary Mass Spectrometry*; John Wiley + Sons: 2007.

[68] Hoffmann, E. d.; Stroobant, V., *Mass Spectrometry - Principles and Applications*, 3rd ed.; John Wiley + Sons: 2007.

[69] Budzikiewicz, H., *Massenspektrometrie - Eine Einführung*, 4th ed.; Wiley-VCH: 1998.

[70] Barker, J., *Mass Spectrometry*; Wiley: 1999.

[71] Worley, J.; Kvech, S. More Information on the ICP-MS., `http://www.seaes.manchester.ac.uk/research/facilities/agu/equipment/ICP_MS/moreinfo/` (accessed 10/10/2012).

[72] Bard, A. J.; Faulkner, L. R., *Electrochemical Methods - Fundamentals and Applications*, 2nd ed.; John Wiley + Sons: 2001.

[73] Song, C.; Zhang, J. In *PEM Fuel Cell Electrocatalysts and Catalyst Layers*, Zhang, J., Ed.; Springer London: 2008; Chapter 2, pp 89–134.

[74] Baumann, F. S.; Fleig, J.; Habermeier, H.-U.; Maier, J. Impedance spectroscopic study on well-defined $(La,Sr)(Co,Fe)O_{3-\delta}$ model electrodes. *Solid State Ionics* **2006**, *177*, 1071–1081.

[75] Hamann, C. H.; Vielstich, W., *Elektrochemie*, 4th; Wiley-VCH: Weinheim, 2005.

[76] Huber, T. Konstruktion einer Vakuum-Mikrokontaktapparatur und Impedanzmessungen an mikrostrukturierten Platin- und Nickelelektroden auf Yttrium stabilisiertem Zirconiumoxid in Wasserstoff Atmosphäre., Diploma Thesis, Technische Universität Wien, 2010.

[77] Lvovich, V. F., *Impedance Spectroscopy - Applications to Electrochemical and Dielectric Phenomena*; John Wiley and Sons: Hoboken, New Jersey, 2012.

[78] Pechini, M. P. Method of preparing lead and alkaline earth titanates and niobates and coating method using the same to form a capacitor. pat., 3330697 (U.S.A.), 1967.

[79] Lemmon, E. W. In *CRC Handbook of Chemistry and Physics*, 92nd ed., 2011-2012.

[80] Moraes, V. Herstellung und Charakterisierung von $La_xSr_{1-x}CoO_{3-\delta}$-Kathoden für Festoxidbrennstoffzellen., Bachelor's Thesis, Technische Universität Wien, 2012.

[81] Hutterer, A. Herstellung und Charakterisierung von $(La,Sr)(Co,Fe)O_{3-\delta}$-Kathoden für Festoxidbrennstoffzellen., Bachelor's Thesis, Technische Universität Wien, 2012.

[82] `http://www.malereibetrieb-poppe.de/navi/set/kontakt.htm` (accessed 24/01/2013).

[83] `http://www.digitpedia.com/backward-future-of-computer-design/9204/#.UQD3n_LNNK8` (accessed 24/01/2013).

[84] Pfeiffer Vacuum - Datenblatt OmniStar GSD 320 O2, 1-200 amu, Wolframkathode, beheizte Kapillare 200°C, 1m., `http://www.pfeiffer-vacuum.de/produkte/massenspektrometer/gasanalyse/gasanalyse-im-druckbereich-bis-1-bar/omnistar-gsd-320-o/onlinecatalog.action?detailPdoId=5575#product-downloads` (accessed 23/02/2012).

[85] ICDD PDF-4+ 2010 (Database)., edited by Dr. Soorya Kabekkodu, International Centre for Diffraction Data, Newtown Square, PA, USA, 2010.

[86] Mass Flow Controllers Series FC-77X/77XX, Series FC-78X/78XX, and Series FC-79X User Manual., `http://img19.ybzhan.cn/5/20110825/634498820774538750.pdf` (accessed 05/12/2012).

[87] http://webbook.nist.gov/cgi/cbook.cgi?Spec=C1333740&Index=0&Type=Mass&Large=on&SVG=on (accessed 16/11/2012).

[88] http://webbook.nist.gov/cgi/cbook.cgi?Spec=C7732185&Index=0&Type=Mass&Large=on&SVG=on (accessed 16/11/2012).

[89] http://webbook.nist.gov/cgi/cbook.cgi?Spec=C7782447&Index=0&Type=Mass&Large=on&SVG=on (accessed 16/11/2012).

[90] Skoog, D. A.; West, D. M.; Holler, F. J.; Crouch, S. R., *Fundamentals of Analytical Chemistry*, 8th ed.; Thomson Brooks/Cole: 2004.

[91] Cichna-Markl, M. Vorlesungsunterlagen VO Lebensmittelanalytik I (Universität Wien, VO-Nr. 270077, WS 2009), Teil 1., 2009.

[92] Morrison, G.; Cheng, K. L.; Grasserbauer, M. General aspects of trace analytical methods - IV. Recommendations for nomenclature, standard procedures and reporting of experimental data for surface analysis techniques. *Pure and Applied Chemistry* **1979**, *51*, 2243–2250.

[93] Otto, M., *Analytische Chemie*, 4th ed.; Wiley-VCH: 2011.

[94] Universität Wien, Institut für Analytische Chemie und Lebensmittelchemie - Analytisch-chemisches Praktikum: Beispiel Atomabsorptionsspektroskopie., http://anchem.univie.ac.at/fileadmin/user_upload/anchem/instPraktikum/AAS_Kanz.pdf (accessed 07/12/2012).

[95] Long, G. L.; Winefordner, J. D. Limit of Detection - A Closer Look at the IUPAC Definition. *Analytical Chemistry* **1983**, *55*, 712A–724A.

[96] Schwedt, G., *Analytische Chemie - Grundlagen, Methoden und Praxis*, 2nd ed.; Wiley-VCH: 2008.

[97] Baumann, F. S.; Fleig, J.; Cristiani, G.; Stuhlhofer, B.; Habermeier, H.-U.; Maier, J. Quantitative Comparison of Mixed Conducting SOFC Cathode Materials by Means of Thin Film Model Electrodes. *Journal of The Electrochemical Society* **2007**, *154*, B931–B941.

[98] Gurvich, L. V.; Iorish, V. S.; Yungman, V. S.; Dorofeeva, O. V. In *CRC Handbook of Chemistry and Physics*, 93rd ed., 2012-2013.

[99] Brichzin, V.; Fleig, J.; Habermeier, H. U.; Cristiani, G.; Maier, J. The geometry dependence of the polarization resistance of Sr-doped LaMnO$_3$ microelectrodes on yttria-stabilized zirconia. *Solid State Ionics* **2002**, *152-153*, 499–507.

[100] Ahamer, C. Auswirkung der Mikrostruktur von Yttrium-stabilisiertem Zirconiumoxid auf dessen Leitfähigkeit., Diploma Thesis, Technische Universität Wien, 2012.

[101] Opitz, A. Oxygen Exchange Pathways of Pt Model Electrodes on YSZ., Ph.D. Thesis, Technische Universität Wien, 2011.

Curriculum vitae

Personal information

Gregor Walch

gregor.walch@gmx.at

Education and training

September 2012	Poster contribution "High temperature electrolysis with $La_{0.6}Sr_{0.4}FeO_{3-\delta}$ thin film electrodes" at "Electrochemistry 2012" conference in Munich
Since February 2012	Master thesis "High temperature electrolysis on model-type $La_{0.6}Sr_{0.4}FeO_{3-\delta}$ thin film electrodes" under supervision of Prof. Jürgen Fleig at Vienna University of Technology
September 2011 – February 2012	Erasmus stay at Aix-Marseille Université, Marseille
Since October 2005	Chemistry studies at University of Vienna
1996 – 2004	Secondary school GRG 21 Ödenburger Straße, focus on languages (English: 8 years, French: 6 years, Italian: 4 years)
1992 – 1996	Primary school

Languages

English	Certificate in Advanced English (June 2003), level C1
French	Level B2/C1